X-ray Study of Accretion-Powered Pulsar Hercules X-1 with Suzaku
すざく衛星を用いた降着駆動型パルサー ヘラクレス座X-1の研究

東京理科大学・理学研究科・物理学専攻

阿佐美　ふみ

Abstract

Accretion-powered pulsars consists of a dense and magnetized neutron star and a normal stellar companion. They are astrophysical laboratories for testing theories of dense matter physics and propagation of radiation in strong magnetic fields. The accretion-powered pulsars convert the gravitational binding energy of the accreted matter into X-ray. Thus, the X-ray gives information about neutron stars and its surrounding environment.

Hercules X-1 discovered in 1972 is a prototype of the accretion-powered pulsars. It therefore has been well investigated, but its radiation mechanisms have not been revealed completely due to the complex X-ray spectrum. In particular the spectral features (a number of components and its structures) around 4–10 keV still remain unclear. The spectral features can play role as probes that provided information about Hercules X-1. In this thesis the existence of a radiation component which has been not established in the 4–9 keV range is presented, using the Suzaku satellite data.

Hercules X-1 was observed in the main-on state from 2005 to 2010. The 0.4–100 keV wide-band spectra obtained in four observations showed a broad hump around 4–9 keV in addition to narrow Fe lines at 6.4 and 6.7 keV. The hump was seen in all the four observations regardless of the selection of the continuum models. Thus it is considered a stable and intrinsic spectral feature in Hercules X-1. The broad hump lacked a sharp structure like an absorption edge. Thus it was represented by two different spectral models: an ionized partial covering or an additional broad line at 6.5 keV. The former required a persistently existing ionized absorber, whose origin was unclear. In the latter case, the Gaussian fitting of the $\sim$6.5 keV line needs a large width of σ = 1.0–1.5 keV and a large equivalent width of 400–900 eV. If the broad line originates from Fe fluorescence of accreting matters, its large width may be explained by the Doppler broadening in the accretion flow. However, the large equivalent width may be inconsistent with a simple accretion geometry assuming the dipole magnetic field.

Contents

Chapter 1

INTRODUCTION

Accretion-powered pulsars, which consists of a magnetized neutron star in orbit with a normal stellar companion, would allow us to examine the high-density matters and the radiation transfer in a strong magnetic field. The neutron star has its radius of $R_{\rm NS}$ $\sim$10 km and mass of $M_{\rm NS}$ $\sim$1.4$M_{\odot}$ ($M_{\odot}$ is the solar mass; 1.99×10^{33} g) and then the core has higher density than nuclear matter ($\sim$2.3 $\times 10^{14}$ g cm^{-3}). Some neutron stars also have a strong magnetic field of 10^{12} G, where the X-ray polarization would be generated due to the differential opacity among the electric vectors of photons. (However, the X-ray polarization from the cosmic X-ray sources has not been detected except Crab nebula.) In the accretion-powered pulsar the matter from the companion star is accreted onto the neutron star. The accreting matter is channeled by the strong magnetic field into a columnar geometry, and the resulting emission is powered by the conversion of gravitational potential energy into kinetic energy, which escapes from the column in the form of X-rays as the matter decelerates through a radiative shock and settles onto the stellar surface. Therefore, the X-ray study is the only way to investigate the high-density matters and the radiation transfer in the accretion-powered pulsars.

Hercules X-1 (Her X-1) is one of the accretion-powered pulsars. In some observations the 4–9 keV spectrum exhibited a broad and hump-like feature besides of the X-ray main emission from the accretion column, The 4–9 keV hump was presented by the partially highly-absorbed emission from the accretion column plus two Fe narrow lines at 6.4 keV and 6.7 keV, or a broad (σ $\sim$0.5 keV) Fe line around 6.5 keV. However it has been not revealed whether the 4–9 keV hump is artificial or is independent from to Fe narrow lines because of a potential for a failure modeling of the emission from the accretion column and a poor energy resolution of past detectors. The 4–9 keV hump would become a probe that reveals the description of absorber or scatter surrounding Her X-1, or dynamics of accretion matter close to the neutron star. Our purpose is to reveal the existence of the broad 4–9 keV hump using the X-ray spectral analysis and discuss the possible origins of the hump.

In this thesis, we report the results of the X-ray observations of Her X-1 with Suzaku, which is the Japanese X-ray satellite. Chapter 2 gives an introduction to the close X-ray binary systems. In Chaper 3 we give a description of the Her X-1 X-ray binary and review past

X-ray observations. In Chapter 4 we show instrumentation of Suzaku. Chapter 5 shows the Suzaku observations of Her X-1. In Chapter 6 we present analysis of X-ray spectra from the Suzaku data. In Chapter 7 we discuss the results of our analysis and provide interpretations of them. A summary is given in Chapter 8.

Chapter 2

ACCRETION-POWERED PULSARS

2.1 General picture

The accretion-powered pulsars, which consists of a highly magnetized neutron star and a normal stellar companion. The first discovered accretion-powered pulser is Centaurus X-3 in 1971 (Giacconi et al., 1971) with the Uhuru satellite which is the first NASA's astronomy one. Centaurus X-3 exhibits a pulse period of 4.84 s only in the X-ray flux. The X-ray pulsation is a common feature among the accretion-powered pulsars. Therefore, the accretion-powered pulsars are also called "X-ray pulsars". A second X-ray pulsar is Hercules X-1, which was discovered in 1972 by the Uhulu satellite (Tananbaum et al., 1972) and one of the most widely studied accretion-powered pulsars. About 110 accretion-powered pulsars are known now. Their pulse periods range from a few ms to several hours.

Figure 2.1 shows a sketch of an X-ray binary system. Matter from the stellar companion often forms a disk around the neutron star, hereafter accretion disk. The accretion matter falls in the neutron star and results X-ray emission is powered by the conversion of gravitational potential energy into kinetic energy with a shock wave heating. The neutron star in the accretion-powered pulsars has the strong magnetic field, typically 10^{12} G (10^{8} T). The accretion matter is channeled by the strong magnetic field and fall in the magnetic poles of the neutron star. If the magnetic axis is inclined to the rotational axis of the neutron star, the X-ray is modulated with the spin. Some sources with the stable accretion are persistently so bright in X-ray that they have been well investigated since from the early age of the cosmic X-ray observations which started in 1962 (Giacconi et al., 1962).

Some of the accretion-powered pulsars (> 10), Her X-1, Cen X-3, and Vela X-1 etc..., were directly measured the magnetic-field strengths of the neutron stars using a spectral feature (like an absorption line) caused by quantized electron cyclotron resonances (the detailed will be shown in section 2.4). The correlations among the line energy of the feature, X-ray flux, and other spectral parameters has been explored (Coburn et al., 2002; Staubert et al., 2009; Staubert, 2013). This variation of the line is considered to be influenced by the accretion rate.

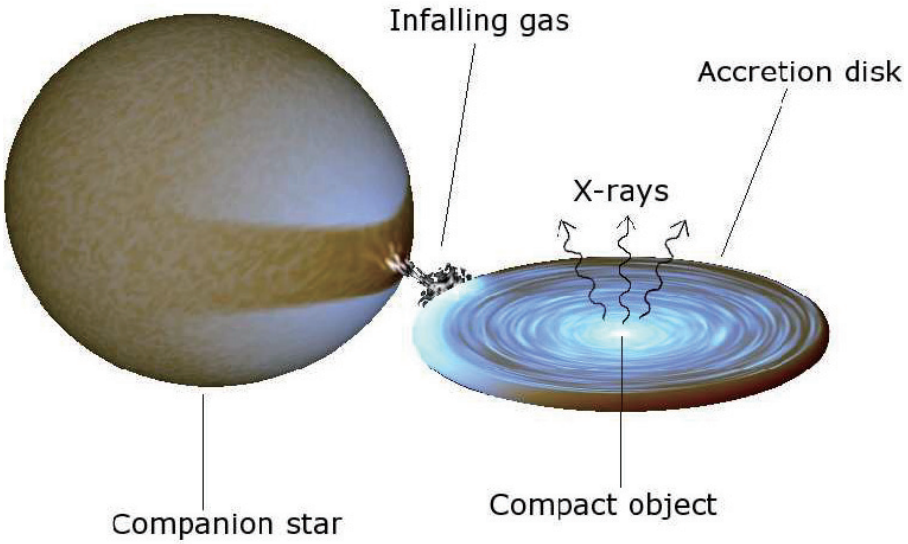

Figure 2.1: A schematic view of an X-ray binary (Klochkov, 2007). Gas is pulled off the normal star by the gravity of the compact object.

Accretion-powered pulsars are astrophysical laboratories for testing accretion dynamics and the physical mechanisms in extreme conditions. A X-ray study is the only way to investigate the physical information and process about the neutron star, accreting matter and its surrounding environment.

2.2 Neutron star

The idea of a neutron star was conceived about 80 years ago. Neutrons were discovered by Chadwick in 1932. During this discussion, Landau proposed the idea of the neutron star. Baade and Zwicky (1934) suggested that the high-dense star is produced through the supernova of the massive stars and proposed the name "neutron star". Oppenheimer and Volkoff (1939) performed the first calculation of the neutron star masses and radii using the equation of state for a cold Fermi gas. On November 28, 1967, Bell and Hewish observed a pulsation of the radio wave with a 1.337 s period from PSR 1919+21. This event played the most impotent role of the reality of the neutron stars. Hewish shared the 1974 Nobel Prize in physics.

As mentioned above, the neutron star is a stellar remnant which is produced by the gravitational collapse of a massive ($\geq 10 M_\odot$) star. The mass of the neutron star balances the degenerate pressure of neutrons. Therefore, the neutron stars are estimated to have its radius of $\sim$10 km and its mass of $\sim 1.4 M_\odot$. The density of the neutron star is at least by a factor of 3 greater than the averaged that of the nuclear matter ($\sim 2.8 \times 10^{14}$ g cm^{-3}). The neutron star is to provide a unique laboratory for exploring the properties of cold matter at supranuclear density. As shown in Figure 2.2, the $\sim$1 km thick crust consists of neutron rich nuclei in a lattice and a uniform background of electrons and, in the inner crust, also a neutron gas. The interior of the neutron star contains a nuclear liquid of mainly neutrons, $\sim$10% protons at densities above nuclear matter density increasing towards the center. When (and if) the density exceeds the nuclear density by a factor of 2 or 3, very exotic stuff might be able to form, like pion condensates, lambda hyperons, delta isobars, and quark-gluon plasmas. Some equation of states (EOS), i.e. the relation between the density and mass, is theoretically calculated with various matters (Lattimer and Prakash, 2001). The EOS gives the mass-radius relation of cold stellar object. Thus, if we obtain the mass or radius of the neutron star, we can strongly constrain the neutron-star matter EOS, and the interior composition of the neutron star. In fact, the neutron star in the X-ray binary of PSR J1614-2230 was found to have $2 M_\odot$, and then some EOSs which indicate the presence of hyperons, bosons, or free quarks was ruled out (Demorest et al., 2010). However, almost neutron stars are not measured their masses due to the difficulty of it and no way to do, and the radius of the neutron star has not been measured. Therefore measuring the masses and radii of the neutron stars and its way is required.

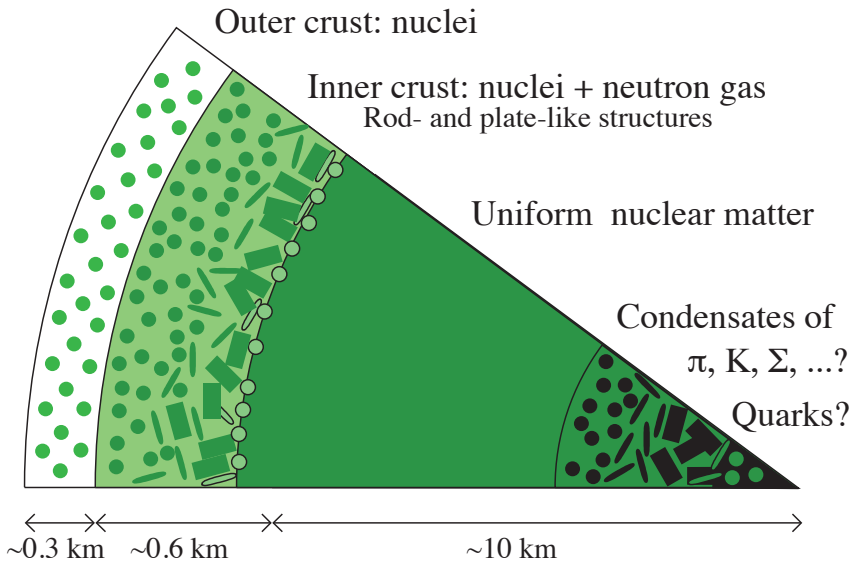

Figure 2.2: Cross-section of a $\sim 1.4 M_{\odot}$ neutron star Heiselberg (2002).

Table 2.1: The properties of HMXB and LMXB (Tauris and van den Heuvel, 2006).

	HMXB	LMXB
X-ray spectra	$kT \geq 15$ keV (hard)	$kT \leq 10$ keV (soft)
Type of time variability	regular X-ray pulsations no X-ray bursts	only a very few pulsars often X-ray bursts
Accretion process	wind	Roche-lobe overflow
Timescale of accretion	10^5 yr	10^{7-9} yr
Accreting compact star	high B-field NS	low B-field NS
Spatial distribution	Galactic plane	Galactic center and spread around the plane
Stellar population	young, age $\leq 10^7$ yr	old, age $\geq 10^9$ yr
Companion stars	luminous, $L_{\rm optical}/L_{\rm X} \geq 1$ $\geq 10 M_\odot$	faint, $L_{\rm optical}/L_{\rm X} \ll 0.1$ $\leq 1 M_\odot$

2.3 Binary system and accretion mechanism

The accretion-powered pulsars are one of the binary system in the universe. The system are classified according to the mass of the companion star, high mass X-ray binaries (HMXB) where the mass is greater than several solar masses, and low mass X-ray binaries (LMXB). In the former, the matter form the companion star accretes through stellar wind. On the other hand, in the latter mass accretion occurs through the inner Lagrangian point–the point where the gravitational pull of two large masses precisely equals the centripetal force required for a small object to move with them. The properties of HMXB and LMXB are summarized in Table 2.1. For the two classes, we show the binary system and the accretion mechanism in the following.

The potential of the close binary system, defined as the Roche potential, is briefly described as

$$\Phi = -\frac{GM_1}{r_1} - \frac{GM_2}{r_2} - \frac{\omega^2 r_3^2}{2} \tag{2.1}$$

where M_1 and M_2 are the masses of the stars, r_1 and r_2 are the distances to the center of the stars, G is the gravitation constant, ω is the orbital angular velocity, and r_3 is the distance to the axis of rotation of the binary. The first and second terms are the gravitational potential, and the third one is the centrifugal potential. Figure 2.3 shows the geometry and the equipotential surface. Close to each star, the potential is dominated by the gravity of that star, and the equipotential surface has an almost spherical shape. The droplet-shaped figures in the equipotential plot are called the Roche lobes of each star. The some potential extremum are called the Lagrangian points, where the net force on particle cancel out. The number of the Lagrangian points is five. The first Lagrangian point is placed at the center of the droplet. The distribution of the matter in the system is restricted to the Roche potential with a simple picture. If the Roche lobe is filled with the matter from one star the mass transfer occurs via the Lagrange point.

The evolution of the system is estimated with the assumption of the conservation of the

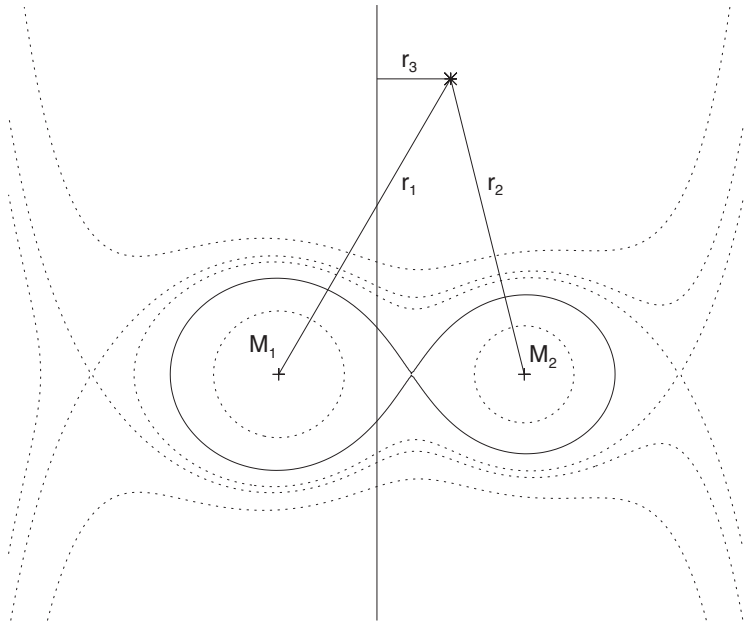

Figure 2.3: Roche lobe geometry for a mass ratio $M_1/M_2 = 3/2$ (Klochkov, 2007). The plot shows cuts through equipotential surfaces of the co-rotating frame, parallel to the rotational axis, which is shown by the vertical solid line.

mass and angular momentum J of the binary system. For a circular orbit these conditions are

$$M_1 + M_2 = \text{const.} \tag{2.2}$$

$$J = \omega r_1^2 M_1 + \omega r_2^2 M_2 = \text{const.} \tag{2.3}$$

With the Kepler's third law and the Equations 2.2 and 2.3 we obtain

$$\dot{M_1} \frac{M_1 - M_2}{M_1 M_2} = \frac{\dot{a}}{2a} \tag{2.4}$$

where $a = r_1 + r_2$ is the binary separation. This equation indicates that the binary separation of a decrease during the condition of $\dot{M_1} < 0$. Thus, the orbital period become shorter. Considering the above, we show the accretion mechanisms for LMXB and HMXB in the following sections.

2.3.1 Roche lobe overflow and disk accretion

In LMXB, when the outer layer of the companion star expand and reach the Roche lobe with the evolution, the mass transfers from the companion to the neutron star via the inner Lagrangian point. This phenomenon is called the Roche lobe overflow. Figure 2.4 shows this picture. Assuming that the all points in the accretion disk, the local circular velocity remains

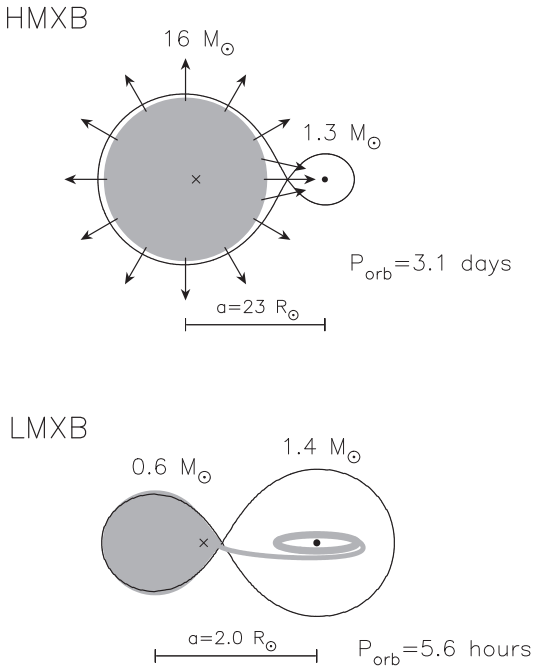

Figure 2.4: Schematic view of the accretion in HMXB (top) and LMXB (bottom) (Tauris and van den Heuvel, 2006).

Keplerian, the specific angular momentum J at the radius r is given by

$$J = \Omega_{\rm K} r^2 = \sqrt{G M_{\rm NS} r}, \tag{2.5}$$

where $\Omega_{\rm K} = \sqrt{G M_{\rm NS}/r^3}$ is the angular velocity at r. This formula can be rewrote for a radius,

$$R_{\rm circ} = \frac{J^2}{G M_{\rm NS}}. \tag{2.6}$$

Here $R_{\rm circ}$ is called the circularization radius. If the accretion matter satisfies this condition, which means that the matter has an adequate angular momentum, the Keplarian accretion disk can be formed.

2.3.2 Accretion from the stellar wind

In HMXB, luminous OB stars produce powerful winds (over Roche lobe). If the neutron star can capture a part of the matter it is required that the matter is within the accretion radius

$$r_{\rm acc} = \frac{2GM_1}{v_{\rm rel}^2}. \tag{2.7}$$

Here $v_{\rm rel}^2 = v_{\rm w}^2 + v_{\rm orb}^2$, $v_{\rm w}$ is a velocity of the accreting matter (wind), $v_{\rm orb}$ is a orbital velocity (Bondi and Hoyle, 1944; Blondin et al., 1990). If the wind is emitted over a solid angle Ω and

has total mass loss rate $\dot{M}_{\rm w}$ this implies an accretion rate

$$\dot{M} \sim \frac{\pi r_{\rm acc}^2}{\Omega a}\dot{M}_{\rm w}, \tag{2.8}$$

where a is the binary separation. It is difficult to decide whether the disk formation condition (Equation 2.6) is satisfied. The periodic variations of X-ray flux indicate that some HMXBs, Cen X-3, LMC X-4, and SMC X-1, has the accretion disk.

2.3.3 Accretion onto a magnetized neutron star

The magnetic field strength at the surface of neutron stars is typically about 10^{12} G (10^8 Tesla). Because of the strong magnetic field, the accretion matter cannot form the accretion disk in vicinity of the neutron star, where the magnetic pressure equals the ram pressure. This point is defined as Alfvén radius $r_{\rm A}$. The ram pressure is written by

$$p_{\rm ram} = \rho v^2, \tag{2.9}$$

where, ρ and v are the density and velocity of the accretion matter, respectively. On the other hand, the magnetic pressure is given by

$$p_{\rm mag} = \frac{B^2}{8\pi}. \tag{2.10}$$

Assuming the spherically symmetrical accretion flow, the accretion rate at r is expressed as $\dot{M} = 4\pi r^2 \rho v$. From Eq. (2.9) and (2.10) we obtain

$$r_{\rm A} = \left(\frac{\mu^4}{\dot{M}^2 2GM_{\rm NS}}\right)^{1/7}, \tag{2.11}$$

where $M_{\rm NS}$ is the mass of the neutron star, $\mu = B^2R^3/8\pi$ is its dipole magnetic moment. The typical value of the $r_{\rm A}$ is $\sim 10^8$ cm (1000 km). Within the $r_{\rm A}$, the accreting matter falls along the field lines toward the magnetic poles of the neutron star.

2.4 X-ray spectrum

As mentioned above, in binary systems of the accretion-powered pulsar mass transfer from companion star occurs. As shown in Figure 2.5 the accretion flow is channeled by the strong magnetic field into a columnar geometry, and the resulting emission is powered by the conversion of gravitational potential energy into kinetic energy, which escapes from the column in the form of X-rays as the gas decelerates through a radiative shock and settles onto the stellar surface. The typical energy (X-ray luminosity), which is released near the magnetic poles of neutron star, is written by

$$L_{\rm X} = \eta \frac{G M_{\rm NS} \dot{M}}{R_{\rm NS}}, \tag{2.12}$$

where η is an X-ray conversion efficiency. Assuming the gravitational potential energy is released through blackbody emission, the effective temperature T in the magnetic poles with the emission area of A is given by the Stefan-Boltzmann law;

$$L = \sigma A T^4. \tag{2.13}$$

Here, σ is the Stefan-Boltzmann constant. The accretion area is considered to be A of $\sim$1 km^2, which is a typical value at neutron-star surface with the dipole magnetic field, and thus the temperature corresponds to $\sim$keV ($\sim 10^7$ K) range. The observed X-ray spectrum of the accretion-powered pulsar is actually a PL up to $\sim$20 keV. Because the cut-off energy is higher than that required by the blackbody temperature, the radiation from the neutron star is not just blackbody emission. Figure 2.6 shows a schematic view of a gas accretion geometry and radiation system near the neutron star magnetic poles. In the accretion column, seed photons are created via thermal emission, bremsstrahlung or blackbody, from heated gas by the shock wave. These thermal emissions are modified by inverse Comptonization of the high-energy electrons gyrating around the magnetic field. Recently, some physical models for the radiation from the magnetic poles are developed (Becker and Wolff, 2007), but the emergent spectra are not fully represented. Because of this, most accretion-powered pulsar spectral data have traditionally been fitted using PL model. The observed X-ray spectra of accreting pulsars are characterized by a flat power law with a photon index, Γ, of 1.0–2.0 up to a high-energy cut-off at 10–25 keV, above which the spectrum decays more steeply. The spectrum above the high-energy cut-off, $E_{\rm cut}$, is often approximated by the function $\exp[(E_{\rm cut} - E)/E_{\rm fold}]$, where $E_{\rm fold}$ is the e-folding energy describing the cut-off steepness (White et al., 1983).

One of the characteristic feature for the accretion-powered pulsars is the cyclotron resonance scattering feature. The classical equation of motion of the electron gyrating in a magnetic field B is given by

$$\frac{m_{\rm e} v^2}{r_{\rm L}} = \frac{ev}{c} B, \tag{2.14}$$

where $m_{\rm e}$ is the electron mass, v is the velocity perpendicular to B, $r_{\rm L}$ is the Larmor radius

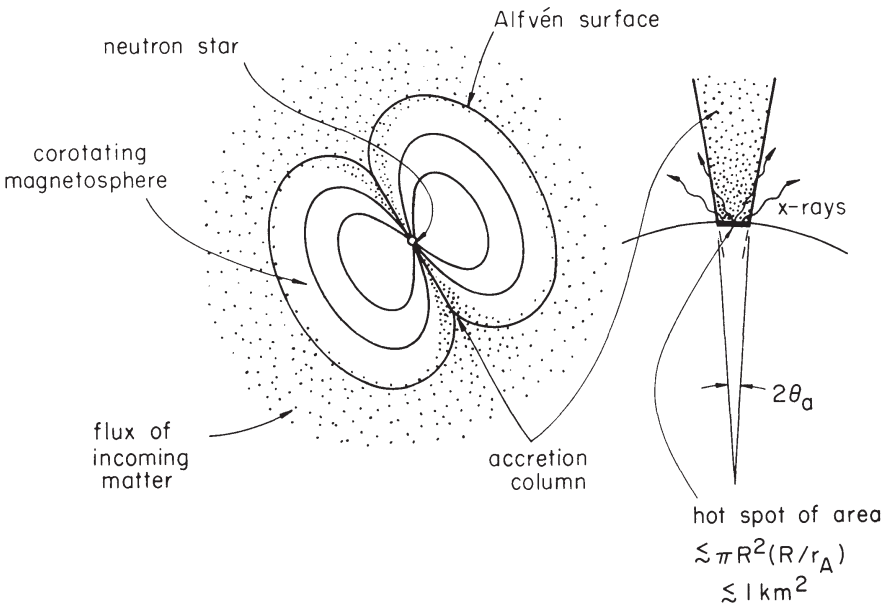

Figure 2.5: Sketch depicting some of the basic features of accretion onto a magnetic neutron star (Lamb et al., 1973). (Left) An overall view of the magnetosphere showing the location of the r_A surface. (Right) A close-up view of an accretion column.

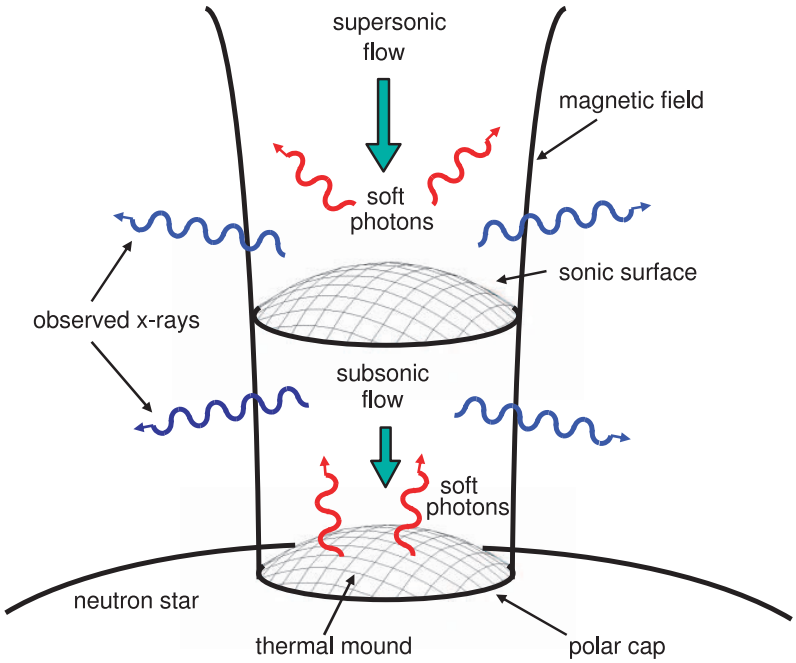

Figure 2.6: Schematic depiction of gas accreting onto the magnetic polar cap of a neutron star (Becker and Wolff, 2007).

of the electron, c is the light speed. When $r_{\rm L}$ becomes comparable to or smaller than the de Broglie wavelength of the electron $\hbar/p = \hbar/(\gamma mv)$, quantum effects become important. This condition sets in for

$$\frac{\hbar}{\gamma mv} \geq \frac{\gamma mcv}{eB} \tag{2.15}$$

or for magnetic fields

$$B \geq \frac{m^2c^3\gamma^2}{e\hbar}\left(\frac{v}{c}\right)^2. \tag{2.16}$$

This indicates that above $B \simeq 10^{12}$ G quantum effects are important. The kinetic energies of the plasma electrons in such a strong B-field are quantized perpendicular to the field lines in discrete Landau levels (Meszaros, 1992; Daugherty and Harding, 1986). From solving the Schrödinger equation, Landau levels is given by

$$\begin{aligned} E &= \frac{1}{2}\hbar\omega_{\rm c}(2n+1+s), \\ n &= 0,1,2,...,s = \pm 1 \end{aligned} \tag{2.17}$$

where $\omega_{\rm c} = eB/m_{\rm e}c$ is the usual cyclotron energy, n is the Landau quantum number, and s is the spin eigenvalue. Thus, the relation between the cyclotron energy and the magnetic field is expressed as,

$$E_{\rm cycl} \simeq \hbar\omega_{\rm c} \simeq \frac{\hbar eB}{m_{\rm e}c} \simeq 11.6\frac{B}{10^{12}\ {\rm G}}\ {\rm keV}. \tag{2.18}$$

The incident photons with the cyclotron energy or its integral multiple are absorbed by the electrons in a strong magnetic field and re-emitted at the same energies in all directions, so significant spectral features are produced. These structures are called the cyclotron resonance scattering features (CRSFs), which are more likely to appear in absorption than in emission (Mihara et al., 1990).

Her X-1 is the first cosmic X-ray source from which a CRSF was detected (Truemper et al., 1978). The CRSF is seen in the X-ray spectra from other accretion-powered pulsars (∼15 objects) (Coburn et al., 2002; Heindl et al., 2004). We cannot isolate the neutron star, the accretion matter, and the accretion disk spatially. Thus, the accretion mechanism (variation of accretion rate, velocity or accretion geometry) and magnetic field geometry are still unclear. The CRSF is one of the powerful tool to explore the physical conditions close to the neutron star, and thus is well investigated. For example the energies of CRSFs depend directly on the magnetic field strength in the line formation region. The luminosity dependance of the line energy is thought to be related to different accretion rates, which move the line forming region in the accretion column to higher or lower altitudes above the neutron star surface, resulting in different magnetic field strengths. In the past results, the variations of the properties of the CRSFs with the X-ray luminosity in the main-on peak and pulse phase was obtained (Staubert, 2013; Enoto et al., 2008; Klochkov et al., 2008). Thus, by measuring the changes of the CRSF, the physical conditions close to the neutron star can be inferred.

In addition to such a PL component a low-energy component that has often been modeled as a blackbody with its temperature $kT_{\rm BB} \sim 0.1$ keV. Some accretion-powered pulsars also exhibit a broad gaussian-like emission at ∼1 keV (e.g. Her X-1, LMC X-4 McCray et al. (1982); Hickox et al. (2004); Hung et al. (2010)). This line feature is considered as a line blending of Fe L-shell lines or He- and H-like Ne K-shell lines. Because there are many emission lines around 1 keV, the origin is still unclear. The soft excess below 1 keV is seen to be produced by a reprocessing of hard X-rays from the neutron star in the inner region of the accretion disk (Hickox et al., 2004).

The Fe K_α fluorescent emission line at ∼6.4 keV has been detected from many accretion-powered pulsars. Along with the soft excess, such a line is believed to be produced when the optically thick material at the inner edge of an accretion disk illuminated by hard X-rays from the central source (Basko, 1980). The Fe K-shell lines can be used to constrain the geometry and physical condition of the X-ray-emitting and reprocessing gas.

2.5 Polarized X-rays from accretion powered pulsars

X-rays generated at the accretion columns are transported through the highly magnetized plasma around the neutron star. During the transportation, the X-rays are suffered by the scattering and absorption by the plasma. The properties (e.g. the cross-sections of the scattering and absorption) depend on the polarization of the X-rays, being very different for the ordinary (O) mode and the extraordinary (E) mode. The O mode has its electric vector (which is the conventional definition of the direction of polarization) lying in the plane defined by the external (i.e., stellar) magnetic field $\boldsymbol{B}$ and the wave vector $\boldsymbol{k}$, while the E mode has its direction of polarization perpendicular to the $(\boldsymbol{k}, \boldsymbol{B})$ plane. This strong disparity between the transport of O and E modes leads to a strong polarization of the emergent radiation. At photon energies $E = h\nu$ far below $E_{\rm cycl}$, the opacity $\kappa_{\rm E}$ of the E mode is drastically reduced compared to that of the opacity $\kappa_{\rm O}$ of the O mode, scaling roughly as $\kappa_{\rm E} \sim (E/E_{\rm cycl})^2 \kappa_{\rm O}$ (Lai and Ho, 2003). Consequently, the emergent radiation is dominated by the E mode, which comes from the deeper and hotter layers of plasma, and so is strongly polarized in the direction of the E mode.

The X-ray emission from the accretion-powererd pulsars is characterized as either pencil- or fan-shaped beam. In the former, the opacity along the accretion column is sufficiently low that the beam emerges preferentially along the column, in a pencil shape. In the latter, the opacity along the column is so high that the beam emerges preferentially through the sides of the column, in a fan shape (Lamb et al., 1973). Pulse profiles for these beam geometries are different (Meszaros and Nagel, 1985), and so are the polarization properties (Meszaros et al., 1988).

In Figures 2.7 and 2.8, the X-ray pulse profiles of accretion-powered pulsars are shown, together with the linear X-ray polarization degree $P_{\rm L}$ and the polarization angle χ as functions

of the pulse phase ϕ, as obtained from the numerical scheme of (Meszaros et al., 1988). For the particular neutron-star and accreting-plasma parameters used in the results displayed in Figures 2.7 and 2.8, the cyclotron resonance energy is $E_{\rm cycl} \approx 38$ keV, and the vacuum resonance energy is $E_{\rm v} \approx 22$ keV. Comparison of the X-ray intensity (I), $\rm P_L$, and χ profiles to the data taken by future X-ray polarimetry satellites will be the most useful tool to probe for X-ray pulsars.

A key signature of the beam geometry (pencil or fan) is the phase correlation between the pulse profile and the $P_{\rm L}$-profile, which can be seen clearly in Figures 2.7 and 2.8. For pencil beams, the maximum in $P_{\rm L}$ is generally in phase with the pulse maximum for photon energies below $E_{\rm v}$, but generally out of phase for photon energies above $E_{\rm v}$. For fan beams, the situation is exactly the opposite. In a similar vein, the phase correlation between the pulse profile and the χ-profile is also a good diagnostic. For pencil beams, χ generally goes from positive to negative values at the pulse maximum, and from negative to positive values at the pulse minimum. Again, for fan beams, the situation is exactly the opposite.

Because of the technical difficulty, few X-ray polarimetries were performed until now. In recent years, thanks to advancements of technology, the movement toward the realization of the X-ray polarimetry observation is activated. The gravity and extreme magnetism small explorer (GEMS) led by NASA (and RIKEN is a core member institute) is the first satellite dedicated to the X-ray polarimetry (Swank et al., 2008). The X-ray polarimeter uses the time projection technique to image the photo-electron tracks ejected by incident X-ray. The polarimeter contains the gas electron multiplier which we have developed for use in space (Tamagawa et al., 2006). The gas electron multiplier is used in many fields such as high energy and nuclear physics, X-ray imaging, etc, and a key deice to multiply an electron cloud whilst retaining its shape. The our gas electron multipliers have high gain ($\sim 10^4$), which is the ratio of output charges to input ones, temporal gain stability ($\leq 2\%$ (FWHM)), and uniformity of the gain in two-dimension ($\sigma \sim 5\%$) (Tamagawa et al., 2009; Asami et al., 2009). The X-ray polarimetry is expected to reveal the radiation transfer underlying strong magnetic fields.

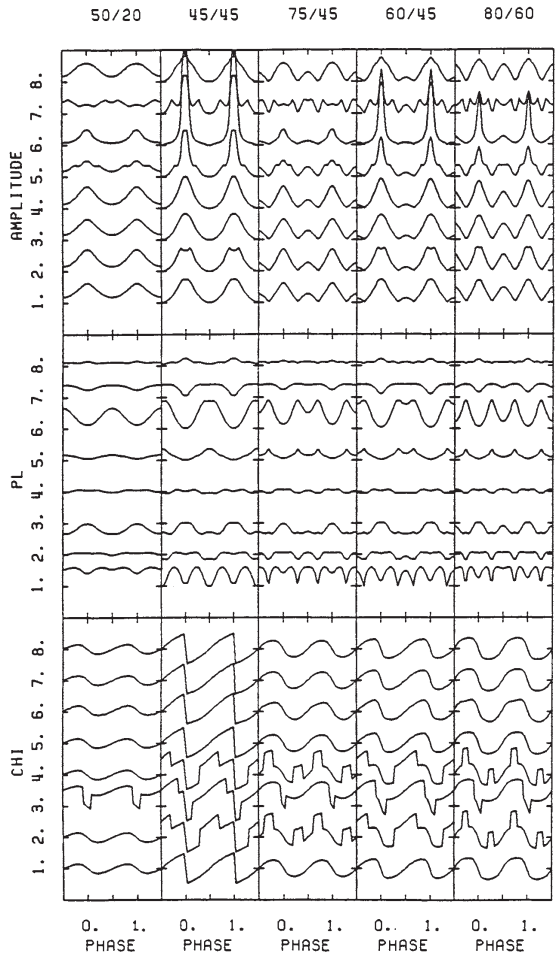

Figure 2.7: Pencil beam model, cyclotron energy $E_{\rm cycl} = 38$ keV, $T = 8$ keV, $\rho = 0.5$ g m^{-3} and $\tau_{\rm T} = 20$ (Meszaros et al., 1988). The pulse amplitude (upper), degree of linear polarization (middle), and polarization angle (bottom) are shown for eight frequencies. From bottom to top these are 1.6, 3.8, 9.0, 18.4, 29.1, 38.4, 51.7, and 84.7 keV, respectively. The cyclotron resonance is the sixth curve up. The pulse amplitude is normalized to the angle-integrated flux. The linear polarization goes from +100% to -100%, and the polarization angle goes from $+180^\circ$ to -180° ($\pm$ one tick mark from the base mark for each curve). The five panels from left to right correspond to five choices of the viewing angles i_1/i_2, indicated along the top of the figure, where i_1 is the inclination angle between the angular momentum and the direction to the observer, and i_2 is the inclination angle between the angular momentum and the stellar magnetic field.

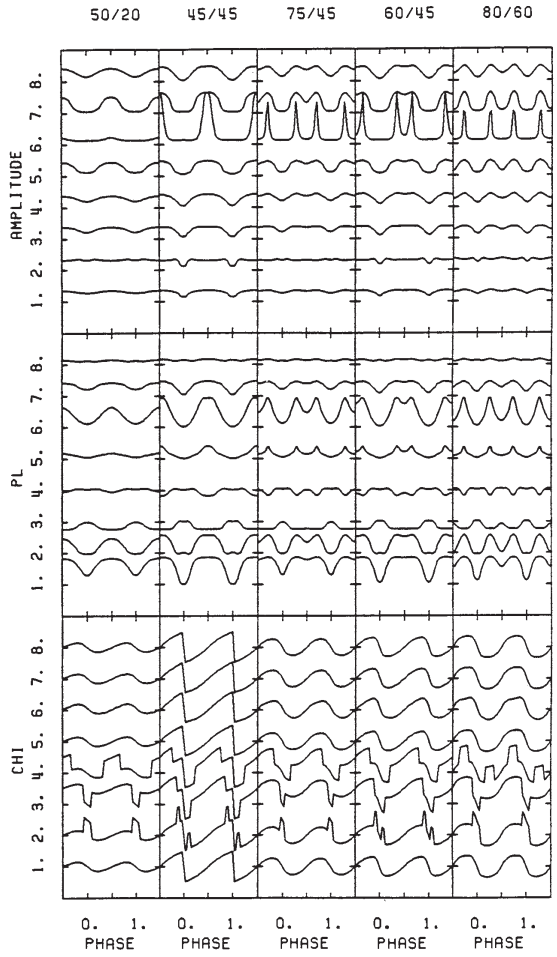

Figure 2.8: Fan beam model, same parameters and convention as in the previous Figure 2.7 (Meszaros et al., 1988).

2.6 Problems for accretion-powered pulsars

As mentioned above, accretion-powered pulsars, which consists of a magnetized neutron star in orbit with a normal stellar companion, would allow us to examine both of the high-density matters and the radiation transfer in a strong magnetic field. The X-ray timing, spectral, (and polarization) studies give information of them. In fact, the variations of pulse period and the cyclotron energy with the X-ray flux are probes of the orbital motion and the accretion mechanism (accretion rate, geometry etc...). However, these have not been clear entirely and we have not measure the masses and radii of the central neutron stars in the pulsars. The spectral analysis would give more information for the neutron star and its surrounding environment than the timing analysis, but the radiation system (radiation components and its emission region) has not been completely revealed because of its complexity and lack of the detectors with an adequate performance. Therefore, using the detailed spectral studies, we would be able to obtain new probes to explore pulsars.

Chapter 3

HERCULES X-1/HZ HERCULES

3.1 Overview

Her X-1 is one of the most studied accretion-powered pulsars discovered by the Uhuru satellite in 1972 (Tananbaum et al., 1972; Giacconi et al., 1973). The companion HZ Her is a A/F type star with a mass of $\sim 2M_{\odot}$, so the binary system of Her X-1 places in between HMXB and LMXB. This source exhibits characteristic periodicity at three different frequencies: a 1.24 s spin period of its neutron star, a 1.7 days orbital period of its binary motion, and a 35 day period as a result of the precession of a tilted, warped accretion disk (Tananbaum et al., 1972; Giacconi et al., 1973). The binary orbit is almost circular and has an inclination i ∼85–88° (Gerend and Boynton, 1976). Because of an edge-on view of the accretion disk, the X-rays from the central neutron star is periodically obscured. As shown in Figure 3.1 the 35-day cycle contains a "main-on" state lasting ∼10 days and a "short-on" state lasting ∼5 days. These states are separated by two "low" states lasting ∼10 days. The X-ray flux in the middle of the main-on state is 3–4 times higher than that in the middle of the short-on state. The X-ray luminosity of the source is typically $L_{\rm X}$ $\sim 10^{37}$ erg s^{-1} for a distance of ∼6.6 kpc found by Reynolds et al. (1997). Although the observed X-ray flux varies by more than an order of magnitude associated with the 35-d cycle, the optical flux averaged over an orbital period changes very little during the nominal 35-d cycle. This is because the optical flux from HZ Her is dominated by X-ray emission reprocessed in the stellar atmosphere (Gerend and Boynton, 1976). A small variation in the disk geometry will block direct X-rays from our line of sight, while the companion star's view remains largely unchanged over much of its surface area.

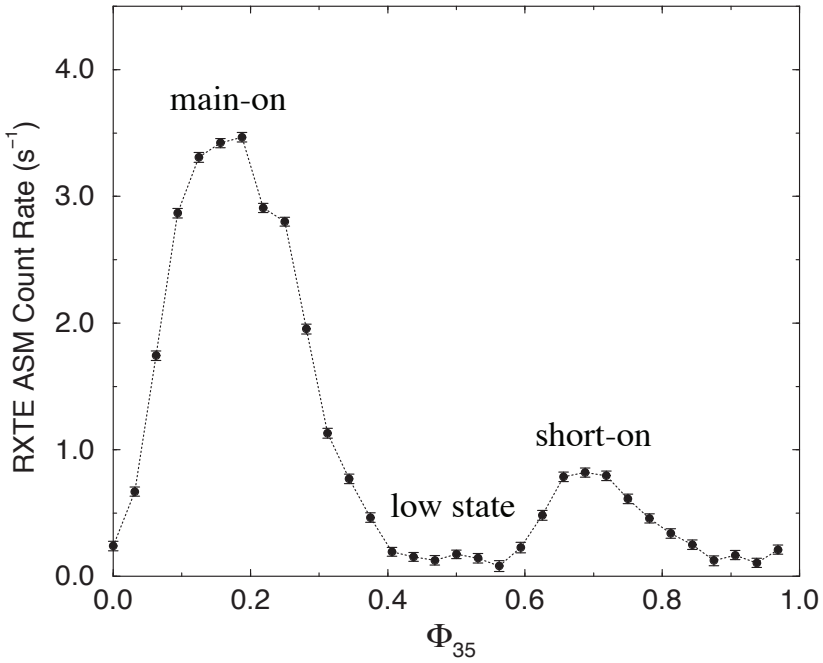

Figure 3.1: The mean 35 day intensity cycle of Her X-1 measured by the RXTE ASM (Oosterbroek et al., 2000). The phases, Φ35, of the main- and short-on, and low states are indicated.

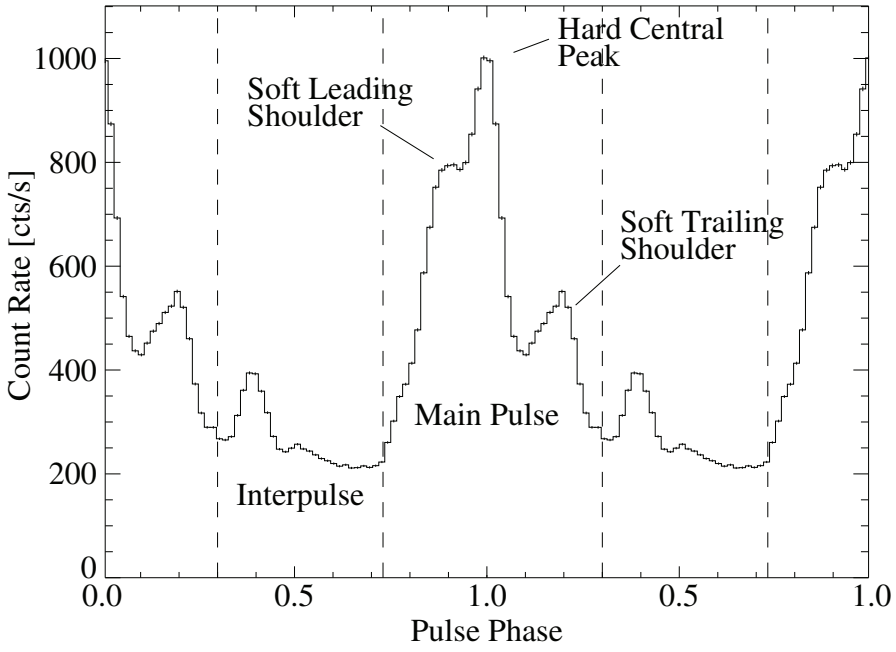

Figure 3.2: An example of Her X-1 X-ray pulse profile in the 9–13 keV energy range obtained with RXTE PCA during a main-on state (Kuster et al., 2005).

3.2 X-ray pulse profiles

Her X-1 has a 1.24 s period due to the spin of the central neutron star. The pulse profile, its long-term variability and energy dependance give us information for the binary system, i.e. geometry, motion of the accretion disk, a number of radiation components, its emission site, etc. Figure 3.2 shows the Her X-1 pulse profile (Kuster et al., 2005). The profile has a main peak, which consists of hard X-rays coming from the accretion column. One peak indicates that we see only one side of the magnetic poles of the central neutron star. As shown in Figure 3.3, it is known that the pulse profile changes associated with the 35-d cycle Truemper et al. (1986); Soong et al. (1990); Kuster et al. (2005). Some explanations for the pulse evolution were proposed. Truemper et al. (1986) interpreted the pulse evolution in terms of a freely precessing neutron star. On the other hand, Scott et al. (2000) explained the evolution with a phenomenological model based on an occultation of the pulse-emitting region by the tilted, inner edge of a precessing accretion disk.

The energy dependence of the pulse profile has also seen (Truemper et al., 1986; Endo et al., 2000; Ramsay et al., 2002; Kuster et al., 2005) and can be used to separate radiation components. For expample, Figure 3.4 shows the energy-resolved pulse profiles of Her X-1 with the ASCA data (Endo et al., 2000). The pulse profiles below 1 keV are clearly different from that above 2 keV, indicating that the low-energy X-rays are produced by the different radiation mechanism from the hard one. The phase shift between low- and high-energy suggests

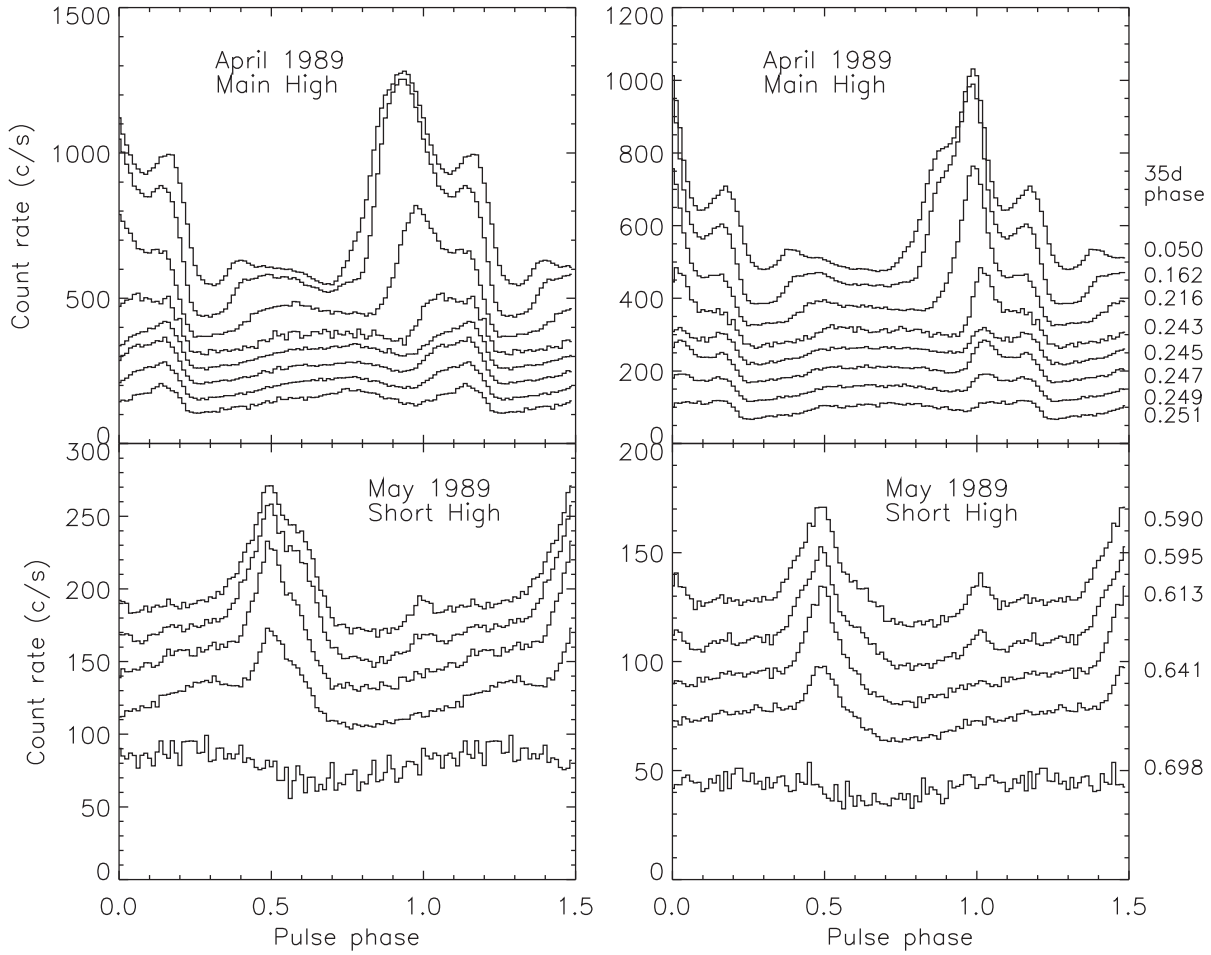

Figure 3.3: X-ray pulse profiles of Her X-1 observed with Ginga as a function of 35-d phase (Scott et al., 2000).

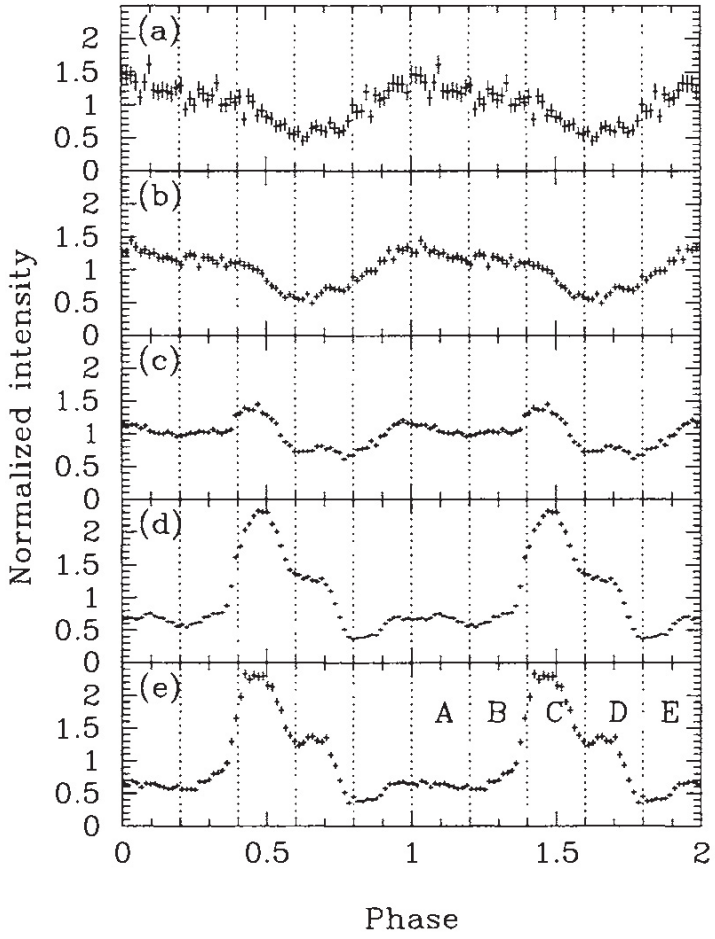

Figure 3.4: Pulse profiles of Her X-1 in different energy bands (Endo et al., 2000). (a) 0.37–0.5 keV, (b) 0.5–0.8 keV, (c) 0.8–1.2 keV, (d) 1.2–4.0 keV, (e) 4–10 keV.

that these X-rays come from different region. Ramsay et al. (2002) found that the phase shift between the low- and high-energy bands during the main-on state was considerably different from that observed in past, and the shift changed in different phase of the 35-d cycle. It is considered that the low-energy X-rays is radiated from the the inner region of the accretion disk illuminated by the high-enegy X-rays from the neutron star (Hickox et al., 2004). Therefore, Ramsay et al. (2002) suggested that the variation of the phase shift is caused by a substantial and continuous variation in the tilt of the accretion disk.

3.3 X-ray spectrum

The broad-band X-ray spectrum of Her X-1 is known to be complex and consists of at least the following components: (1) emission from the accretion column, which is described by a power-law (PL) model with a photon index of $\Gamma \sim 1$ in the energy range of 2–20 keV, (2) a black body with a temperature of $kT_{\rm BB}$ $\sim$0.1 keV that dominates the spectrum below 1 keV (McCray et al., 1982; Oosterbroek et al., 1997), (3) a broad emission feature around 1 keV, called "the broad 1 keV emission" by (Endo et al., 2000), which might be attributed to unresolved Fe L-shell lines (McCray et al. (1982); Oosterbroek et al. (1997, 2000) reported discrimination of two narrow lines, at 0.90 and 1.06 keV), (4) a broad Fe emission feature at 6.4 keV (Choi et al., 1994; Klochkov et al., 2008), which was resolved into 6.4 keV neutral and 6.7 keV He-like Fe K narrow lines by ASCA (Endo et al., 2000), and (5) a cyclotron resonance scattering feature (CRSF) at around 30–40 keV (Truemper et al., 1978; Mihara et al., 1990; dal Fiume et al., 1998; Coburn et al., 2002; Enoto et al., 2008; Klochkov et al., 2008; Fürst et al., 2013). Her X-1 was the first cosmic X-ray source from which a CRSF was detected (Truemper et al., 1978) as shown in Figure 3.5. A second-harmonic CRSF at $\sim$73 keV was also detected with Suzaku (Enoto et al., 2008). Figure 3.6 shows the emission site of the each component suggested by the energy-dependence pulse profile (Figure 3.4). It is considered that the 0.1 keV black body, broad 1 keV emission, and 6.4 keV may be reprocessed in the inner edge of the accretion disk due to the delay of the pulse peak.

Although there are a few observations with wide-band energy coverage, such as the BeppoSAX satellite (dal Fiume et al., 1998) and the Suzaku and NuSTAR satellites (Fürst et al., 2013), spectral decomposition of its wide-band spectrum has not been fully understood yet. For example, dal Fiume et al. (1998) showed that the fit resulted in the two best-fit models consisting of a 0.1 keV black body, a broad Gaussian around 1 keV, a Gaussian at 6.5 keV, and a broken PL plus a high-energy exponential cut-off together with Gaussian absorption or Lorentzian absorption features. Figure 3.7 displays the Her X-1 spectrum obtained by BeppoSAX. While the fitting results were formally unacceptable due to a reduced chi-square value of 1.984 (908) for the former and 1.987 (908) for the latter, they did not add extra components.

In addition above five spectral components Endo et al. (2000) showed that a hard component was required to explain the residuals deviation around 4–7 keV. Figure 3.8 displays the Her X-1 spectrum obtained by ASCA. A second PL with a very large ($N_{\rm H} \sim 5 \times 10^{23}$ cm^{-2}) absorption column density and with a common photon index of the primary PL fitted well the deviating structure around 4–7 keV. This highly absorbed component was also seen in the grating data with the Chandra satellite (Ji et al., 2009). On the other hand, the X-ray spectra obtained with RXTE (Coburn et al., 2002), XMM-Newton (Ramsay et al., 2002), INTEGRAL (Klochkov et al., 2008), NuSTAR (Fürst et al., 2013) in the main-on phase, did not exhibit the highly absorbed component, but a broad (σ $\sim$0.5 keV) gaussian was used to represent the Fe

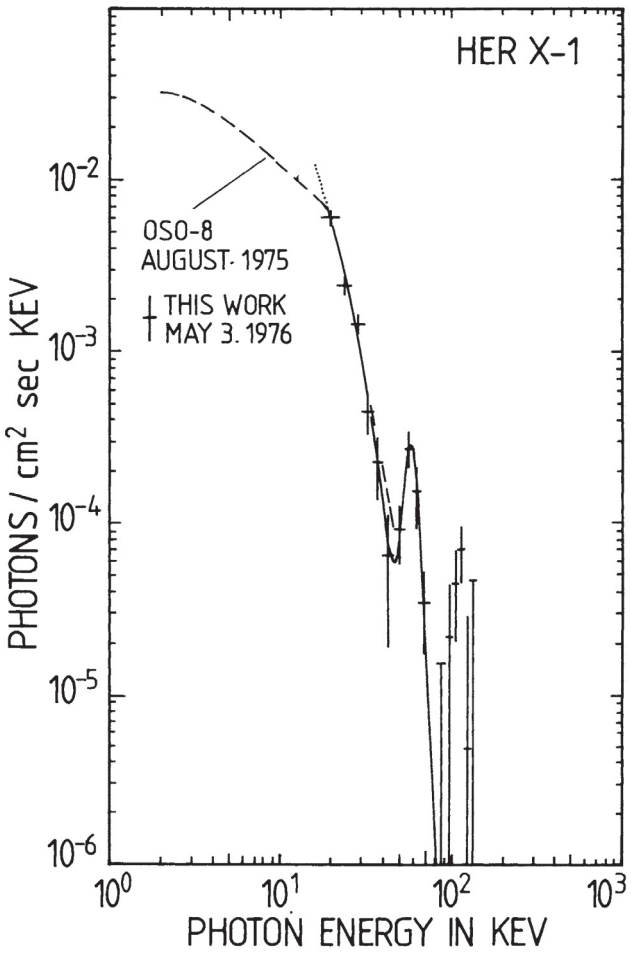

Figure 3.5: Deconvoluted X-ray spectrum of Her X-1 (Truemper et al., 1978).

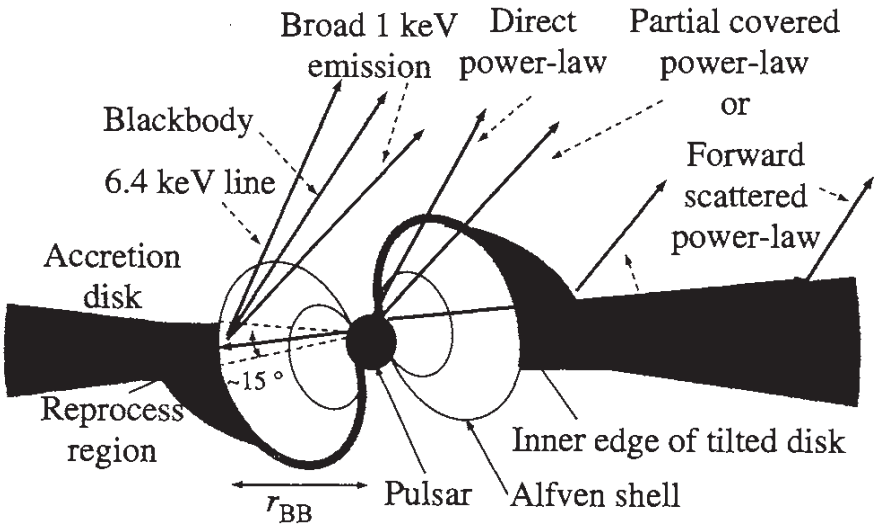

Figure 3.6: Schematic view of the different emission regions in the Her X-1 system (Endo et al., 2000).

K-shell line. Thus, the spectral features around 4–7 keV is complex and have not represented completely due to the additional component or Fe K-shell lines. It has not been clear that the spectral feature around 4–7 keV is stable and intrinsic in the Her X-1 spectra. To reveal the existence of the feature and its radiation mechanism, the multiple observations with the broad-band and the high energy resolution around 4–7 keV are required to regard a fake structure due to a failure modeling of the accretion-column continuum, and a superposition of Fe K-shell lines. In this thesis, we particularly investigate the spectral feature around 4–7 keV with the 0.4-100 keV broad-band spectroscopy of Her X-1 with the Suzaku satellite.

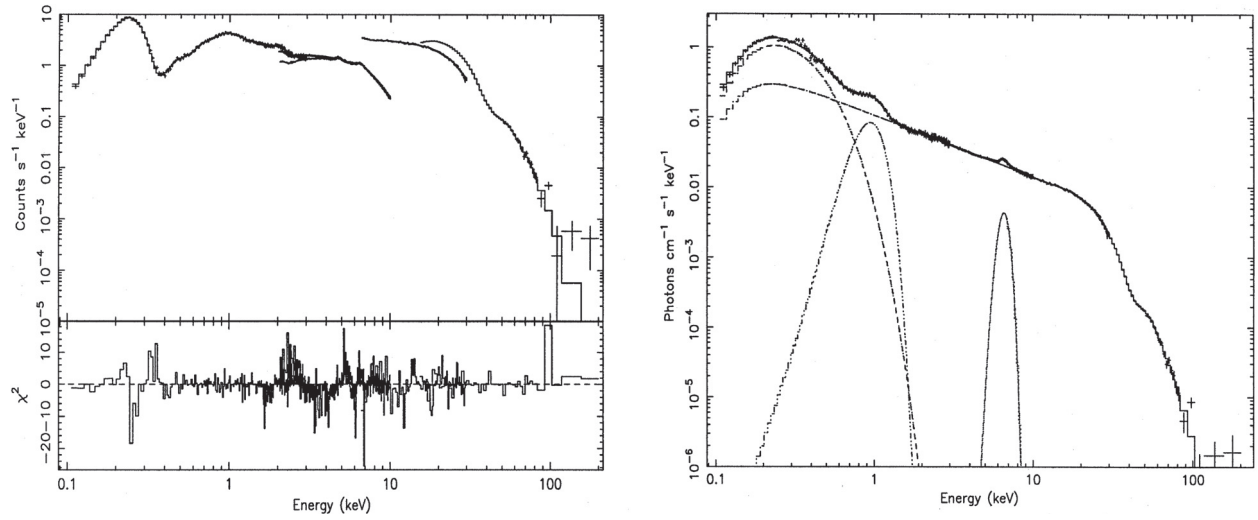

Figure 3.7: The spectrum of Her X-1 in the 0.1–200 keV energy range observed by the BeppoSAX (dal Fiume et al., 1998). Left panel: count rate spectrum and contribution to χ^2. The best-fit obtained model is shown as a histogram. Right panel: deconvoluted photon spectrum. The different spectral components used in the fit are indicated by the dashed lines.

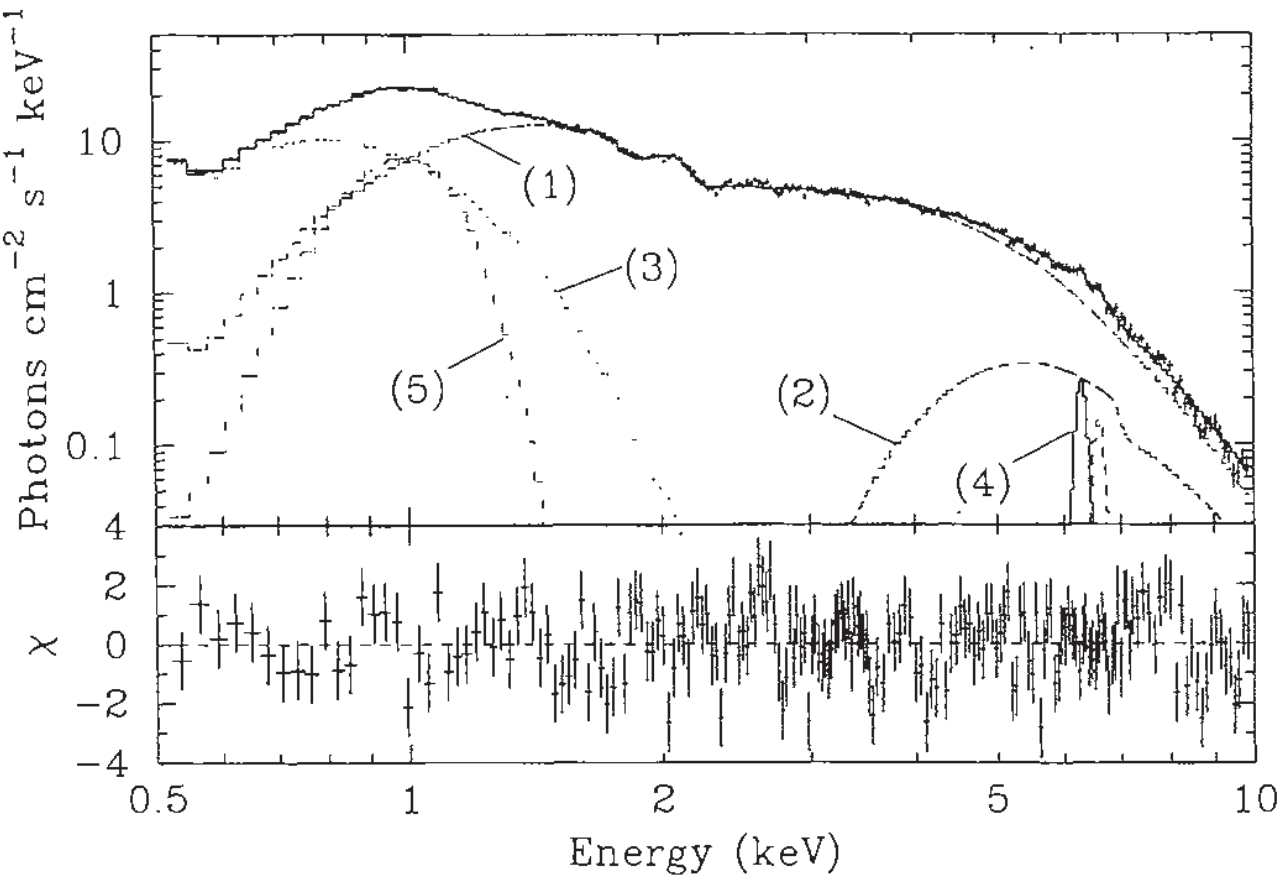

Figure 3.8: Energy spectrum of Her X-1 (Endo et al., 2000) Upper panel: observed data (crosses) and the best fitted model components; (1) direct power-law, (2) highly absorbed power-law, (3) blackbody, (4) iron lines, (5) broad 1 keV emission. Lower panel: residuals from the best-fit model.

Chapter 4

INSTRUMENTATION

4.1 Suzaku

4.1.1 Overview

Suzaku is the fifth Japanese X-ray satellite (Mitsuda et al., 2007) dedicated to observations of celestial X-ray sources, following the great success of Hakucho, Tenma, Ginga and ASCA. The mission is a joint Japanese-US mission, developed by the Institute of Space and Astronomical Science (part of the Japan Aerospace Exploration Agency, ISAS/JAXA) in collaboration with the National Aeronautics and Space Administration's Goddard Space Flight Center (NASA/GSFC) and many other institutions. Suzaku was launched in 2005 July 10 with a M-V-6 rocket from the Uchinoura Space Center of JAXA. The satellite orbit is circular with a height of 570 km from the earth with an inclination angle of 31°, and the orbital period is 96 minutes. Figure 4.1 shows a schematic view of Suzaku. The spacecraft has a weight of 1706 kg, and their height of 6.5 m. The electric power is ∼1700 W and ∼660 W for total and scientific instruments, respectively. The spacecraft pointing accuracy is ∼0.24'. Because the pointing direction of the telescope is limited by the orientation constraint of the solar paddle, the observable area is 65°–115° from the sun. Due to earth occultation and passages of the South Atlantic Anomaly (SAA) in which a huge number of charged particles hit the detector, the mean efficiency of the satellite is 45%. The one of the unique features of Suzaku is that the background environment by charged particles is low and stable. The reason this is the relatively low altitude and this merit is not expected in other satellites in a high altitude orbit. More details can be found in Suzaku technical description (http://www.astro.isas.jaxa.jp/suzaku/doc/).

The Suzaku is equipped with three different instruments: The X-ray imaging spectrometer covering the 0.2–12 keV energy range (XIS; Koyama et al. (2007)), which is a charge-coupled device camera at the focus of the X-ray telescope (XRT; Serlemitsos et al. (2007)), the Hard X-ray Detector (HXD; Takahashi et al. (2007)), which consists of PIN silicon diodes (HXD-PIN; 10–70 keV) and Gd_2SiO_5Ce (GSO; 50–600 keV) scintillators and the X-Ray Spectrometer (XRS; Kelley et al. (2007)), which is a microcalorimeter system at the focal plane of another

XRT module. The XRS was the first orbiting X-ray microcalorimeter spectrometer. However, due to the failure in the cryogen system, the operation was terminated just before the first light.

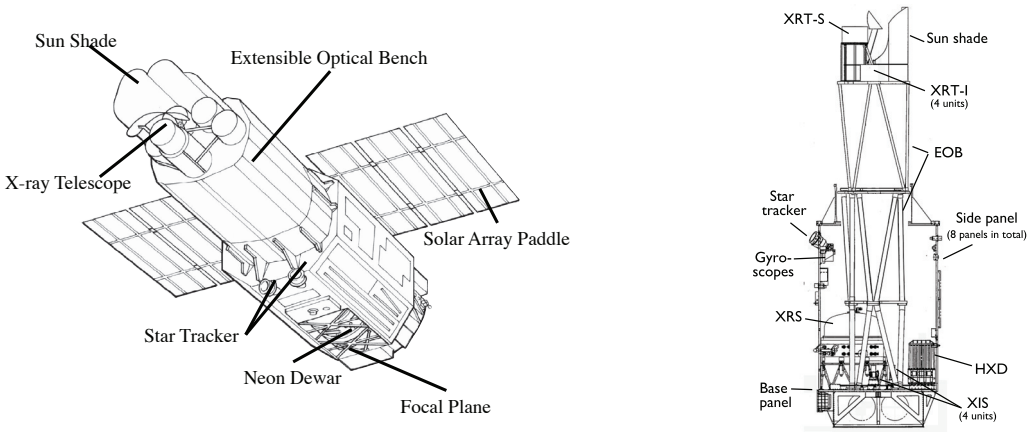

Figure 4.1: Schematic view of Suzaku (left), and its side view (right) (Mitsuda et al., 2007).

4.1.2 X-ray Telescope (XRT)

The XRT is the mirror assembly carried on Suzaku (Serlemitsos et al., 2007). A schematic view of XRT is shown at Figure 4.2. It consists of five thin-foil-nested Wolter-I type telescope. Five XRT modules are installed on the top plate of the Extensible Optical Bench (EOB) of the spacecraft (Figure 4.1). One is dedicated for the XRS, which is called XRT-S, and the other four modules are for each CCD of the XIS, which are called XRT-I0, I1, I2 and I3. The focal length of XRT-S and XRT-I are 4.50 m and 4.75 m, respectively. Actual focal lengths of the individual XRT quadrants deviate from the design values by a few cm. The optical axes of the quadrants of each XRT are aligned to within $2'$ from the mechanical axis. The field of view for the XRT-Is is about $20'$ at 1 keV and $14'$ at 7 keV. An XRT is a cylindrical structure, having the following layered components: (1) a thermal shield at the entrance aperture to help maintain a uniform temperature, (2) a pre-collimator mounted on metal rings for stray light elimination, (3) a primary stage for the first X-ray reflection, (4) a secondary stage for the second X-ray reflection, (5) a base ring for structural integrity and interfacing with the EOB of the spacecraft. All these components, except the base rings, are constructed in 90° segments. As shown in Figure 4.3, four of these quadrants are coupled together by interconnect-couplers and also by the top and base rings. The telescope housings are made of aluminum for an optimal strength to mass ratio. Each reflector consists of a substrate also made of aluminum and an epoxy layer that couples the reflecting gold surface to the substrate.

Including the alignment bars, collimating pieces, screws and washers, couplers, retaining plates, housing panels and rings, each XRT-I consists of over 4112 mechanically separated parts. In total, nearly 7000 qualified reflectors were used and over 1 million cm^2 of gold surface

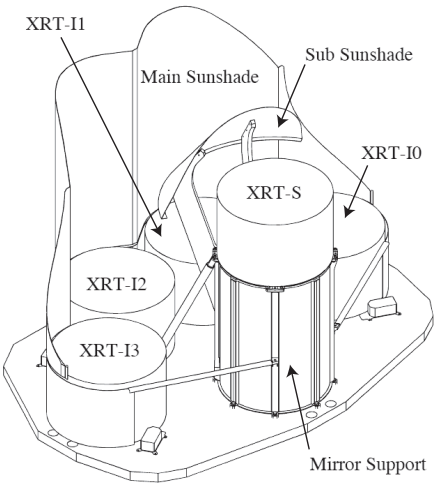

Figure 4.2: Schematic view of XRTs on the Suzaku spacecraft (Serlemitsos et al., 2007).

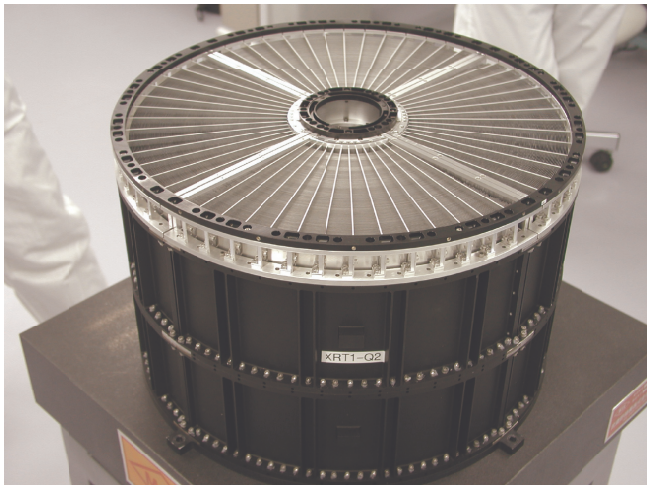

Figure 4.3: Picture of the module XRT-I1 (Serlemitsos et al., 2007).

was coated.

The total effective area of XRT is shown at Figure 4.4 in comparison with two other X-ray satellites. Point Spread Function (PSF) is a spatial distribution function over the detector surface of incident X-ray photons at a given energy for a point-like source at infinity. For the XRT, the PSF is approximately shaped Gaussian, and independent of the photon energy position. The sharpness of images is evaluated either by the Full Width at a Half Maximum (FWHM) or the encircled energy radius of PSF. A circle of 50% encircled energy radius, which is called a half power radius and equals to the half of FWHM if the PSF is exactly Gaussian, accumulates 50% of incident photons. Figure 4.5 shows the images, PSF and Encircled-Energy Fraction (EEF) of the four XRT-I modules for the four XIS sensors. The Half Power Diameter (HPD) is 1′.8, 2′.3, 2′.0 and 2′.0 for XRT 0,1,2, and 3, respectively. The design parameters and performance of XRT are summarized in Table 4.1.

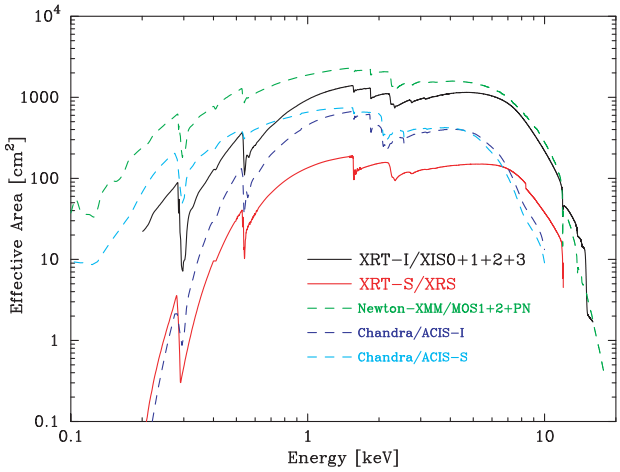

Figure 4.4: Total effective area of the four XRT-I modules compared with that of XMM-Newton and Chandra. Transmissions of the thermal shield and the optical blocking filter, and the quantum efficiency of the CCD are all taken into account (Serlemitsos et al., 2007).

Table 4.1: Design parameters and performance of the XRT (Serlemitsos et al., 2007).

Focal length	4.75 m
Substrate	Aluminum (152 μm)
Reflector	Gold ($>$ 0.1 μm)
Number of nesting	175
Inner / outer diameter	118 mm / 399 mm
Incident angle	0°.18–0°.60
Geometrical area	873 cm^2
Field of view	20′ at 1 keV / 14′ at 7 keV
Effective area	450 cm^2 at 1.5 keV / 250 cm^2 at 7 keV
Half Power diameter	2′.0

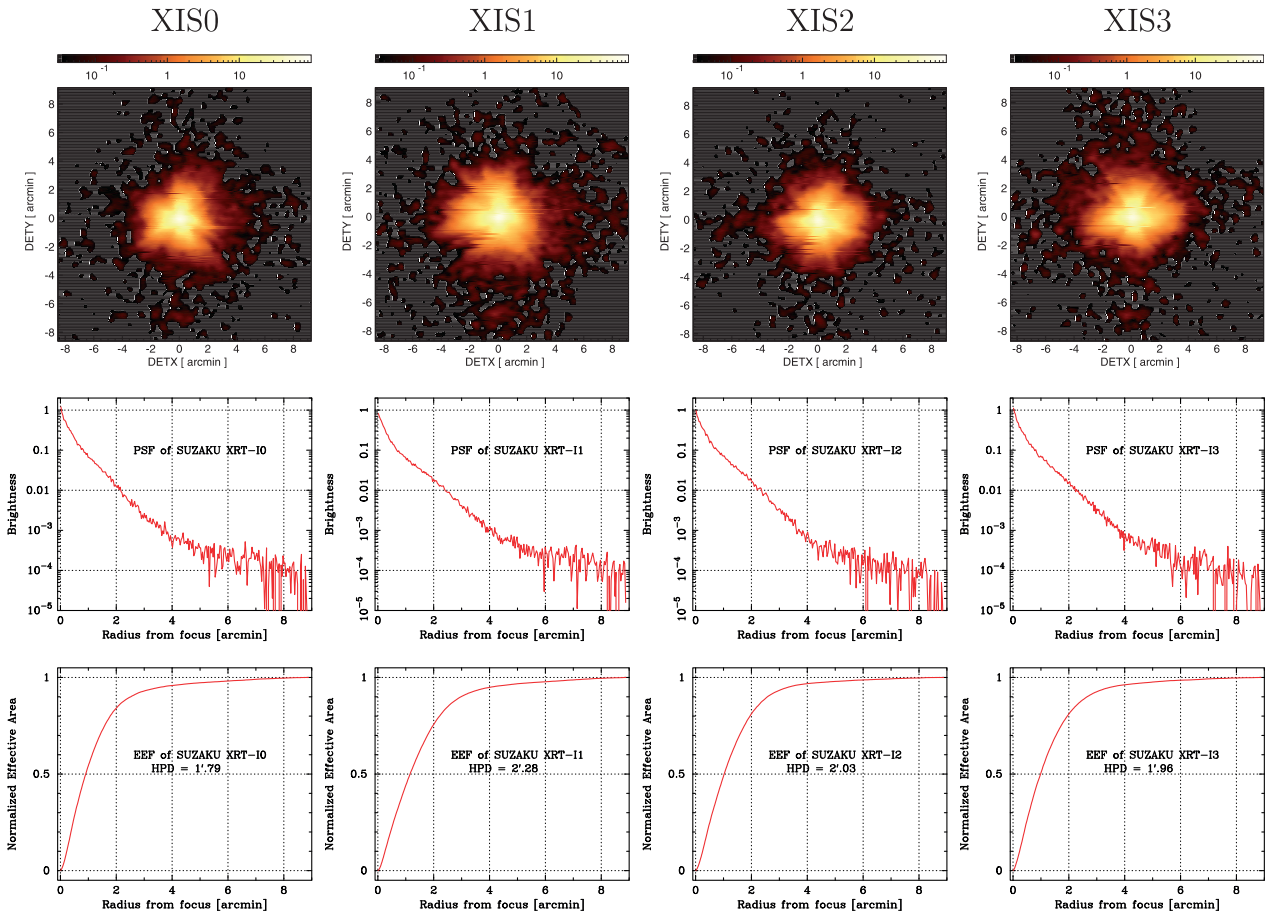

Figure 4.5: Image, Point-Spread Function (PSF), and Encircled Energy Fraction (EEF) of the four XRT-I modules for the four XIS sensors. (Serlemitsos et al., 2007).

4.1.3 X-ray Imaging Spectrometer (XIS)

Suzaku has four XISs, which are shown in Figure 4.6. These employ X-ray sensitive CCDs, which are operated in a photon-counting mode, similar to that used in the ASCA SIS, Chandra ACIS, and XMM-Newton EPIC. In general, X-ray CCDs operate by converting an incident X-ray photon into a charge cloud, with the magnitude of charge proportional to the energy of the absorbed X-ray. This charge is then shifted out onto the gate of an output transistor via an application of time-varying electrical potential. This results in a voltage level (often referred to as "pulse height") proportional to the energy of the X-ray photon. The four Suzaku XISs are named XIS0, 1, 2 and 3, each located in the focal plane of an X-ray Telescope. After the launch of Suzaku, we had operated the four XISs successfully for more than a year. However, a large amount of leaked charge suddenly appeared in one of the sensors, XIS2, in November 2006.Because we could not suppress the leak of charge, we stopped using XIS2 for scientific observations. A similar thing happened to the segment A of XIS0 in June 2009. However, the leak of charge is not serious this time. Although a part of the segment A cannot detect X-rays, we can still use XIS0 for scientific observations. Thus, three sensors (XIS0, XIS1, XIS3) are currently usable.

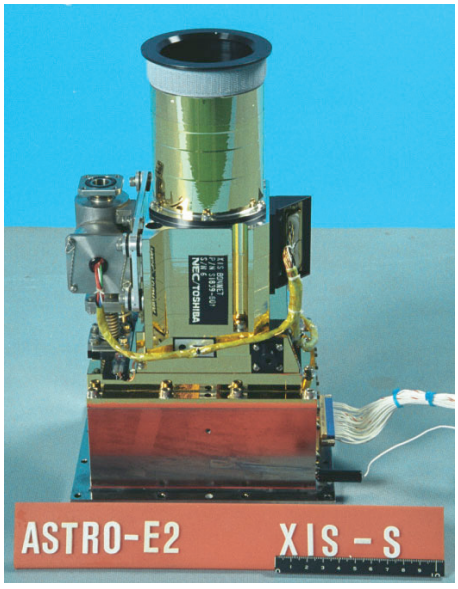

Figure 4.6: A picture of the XIS sensor (Koyama et al., 2007).

As shown in Figure 4.7 each CCD camera has a single CCD chip with an array of 1024×1024 picture elements ("pixels"), and covers an $18' \times 18'$ region on the sky. Each pixel is 24 μm square, and the size of the CCD is 25 mm $\times$ 25 mm. The design parameters and performance of the XIS are summarized in Table 4.2 One of the sensors, XIS1, uses a back-side illuminated CCD, while the other three use a front-side illuminated CCD. The XIS has been partially developed at MIT (CCD sensors, analog electronics, thermo-electric coolers, and temperature control electronics), while the digital electronics and a part of the sensor housing were developed

in Japan, jointly by Kyoto University, Osaka University, Rikkyo University, Ehime University, and ISAS.

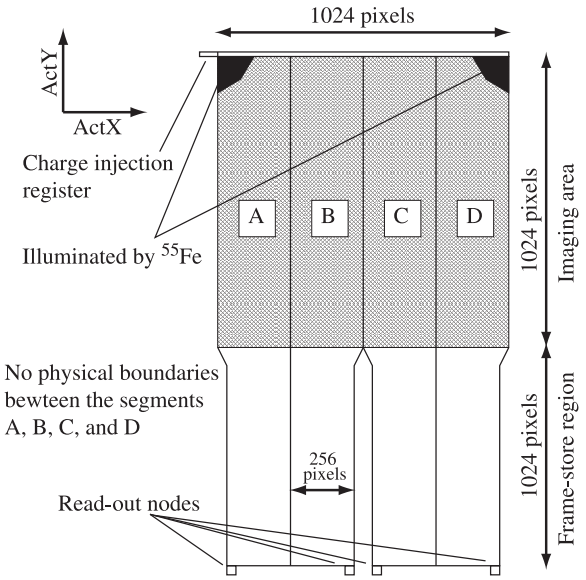

Figure 4.7: Schematic view of the XIS CCD (Koyama et al., 2007). The CCD consists of four segments (A, B, C and D), each with a dedicated read-out node.

Table 4.2: Design parameters and performance of the XIS (Serlemitsos et al., 2007).

Field of view	$18' \times 18'$
Energy range	0.2–12 keV
Format	1024×1024 pixels
Energy resolution	130 eV (FWHM; at 5.9 keV)
Readout noise	$\sim$2.5 electrons
Time resolution	8 s (normal) / 7.8 ms (p-sum)

A CCD has a gate structure on one of the surfaces to transfer the charge packets to the readout gate. The surface of the chip with the gate structure is called the "front side". A front-side illuminated CCD (FI CCD) detects X-ray photons that pass through its gate structures, i.e., from the front side. Because of the additional photo-electric absorption at the gate structure, the low-energy quantum detection efficiency (QDE) of the FI CCD is rather limited. Conversely, a back-side illuminated CCD (BI CCD) receives photons from "back", or the side without the gate structures. For this purpose, the undepleted layer of the CCD is completely removed in the BI CCD, and a thin layer to enhance the electron collection efficiency is added in the back surface. A BI CCD retains a high QDE even in a sub-keV energy band because of the absence of the gate structure on the photon-detection side. However, a BI CCD tends to have a slightly thinner depletion layer, and the QDE is therefore slightly lower in the high energy band. The decision to use only one BI CCD and three FI CCDs was made because of the slight additional

risk involved in the new technology BI CCDs and the need to balance the overall efficiency for low- and high-energy photons.

It is known that the CCD performance gradually degrades in space due to the radiation damage by cosmic rays. This is because charge traps are produced by charged particles and are accumulated in the CCD. One of the unique features of the XIS is the capability to inject small amounts of charge to the pixels. The charge injection is quite useful to fill the charge traps periodically, and to make them almost harmless. This method is called the spaced-row charge injection (SCI), and the SCI has been adopted as a standard method since AO-2 to cope with the increase of the radiation damage (Uchiyama et al., 2009). The charge injection capability is also used to measure the charge transfer efficiency (CTE) of each CCD column in the case of the no-SCI mode (Nakajima et al., 2008; Ozawa et al., 2009).

Data Processing Modes

There are two different kinds of on-board data processing modes. The Clock modes, describing how the CCD clocks are driven, determine the exposure time, the exposure region, and the time resolution. The Clock modes are determined by a program ("micro-code") loaded into the analog electronics. The Editing modes specify how detected events are edited, and determine the format of the XIS data telemetry. The Editing modes are determined by the digital electronics.

In principle, each XIS sensor can be operated with different mode combinations. However, we expect that most observations will use all three sensors in the Normal 5×5 or 3×3 mode (without the Burst or Window options). Other modes are useful for bright sources (when pile-up or telemetry limitations are a concern) or when a higher time resolution (< 8 s) is required.

Clock Modes

Here are two kinds of Clock modes in the XIS, the Normal and the parallel-sum (p-sum) mode. Furthermore, two options (the Window and the Burst options) may be used in combination with the Normal mode.

- Normal Mode: If neither Window nor Burst option (see below) is specified, the exposure time is eight seconds, and all the pixels on the CCD are read out every eight seconds. This can be combined with either of the 5×5, 3×3, and 2×2 Editing modes.

- Parallel-Sum Mode: The pixel data from multiple rows are summed in the Y-direction on the CCD, and the sum is put in the Pixel RAM as a single row. The number of rows to add is commandable, but only 128-row summation is supported at present. The p-sum mode can be used only with the Timing Editing mode, and the Y coordinate is used to determine the event arrival time. As a result, no spatial resolution is available in the Y-direction. The time resolution of the p-sum mode is 8 s/1024 $\sim$7.8 ms.

Window & Burst Options

Table 4.3 indicates that how the effective area and exposure time are modified by the Burst and the Window options. In the Normal Clock mode, the Window and the Burst options can modify the effective area and exposure time, respectively. The two options are independent, and may be used simultaneously. These options cannot be used with the p-sum mode.

- Burst option: All pixels are read out every eight seconds (if the Window option is not specified), but the exposure time can be reduced by introducing a dead time; X-ray events detected during the first t s are discarded, and the exposure time is $(8-t)$ s. This option may be used to avoid photon pile-up when observing a bright source.

- Window option: This option allows shorter exposure times by reading out only a portion of the CCD more frequently. Only a part of the chip within the Y-direction range specified by the commandable Window is used for exposure. The Window width in the Y-direction is 256 pixels around the aim point. When the Window width is 256 pixels (1/4 Window), the exposure time becomes a quarter of that without the Window option (i.e., 2 s), and the Pixel RAM is filled with the data from four successive exposures.

The Window width can be 128 pixels (1/8 Window). However, a significant fraction of the source photons may be lost due to the tail of the XRT point spread function. Furthermore, the fractional loss may be modulated by the attitude fluctuation of the satellite, which is synchronized with the orbital motion of the satellite. Thus the XIS team do not recommend the 1/8 Window option.

One of the disadvantages of the Window option is that the X-rays from the calibration sources ^{55}Fe are out of the window. This makes it difficult to check the gain and the energy resolution of the XIS.

Table 4.3: Effective area and exposure time for different Burst and Window options.

	Effective area	Exposure time
	(nominal: 1024 × 1024 pixels)	(in 8 s period)
None	1024 × 1024 pixels	8 s × 1 exposures
Burst	1024 × 1024 pixels	$(8-t)$ s × 1 exposures
Window	256 × 1024 pixels	2 s × 4 exposures
	128 × 1024 pixels	1 s × 8 exposures
Burst & Window	256 × 1024 pixels	$(2-t)$ s × 4 exposures

Photon Pile-Up

The XIS is essentially a position-sensitive integrating instrument, with a nominal interval of 8 s between readouts. If more than one photon strikes the same CCD pixel, or one of its immediate neighbors, one cannot be correctly measure the energy of each photon; this is the phenomenon

of photon pile-up. Although, the modest angular resolution of the Suzaku XRT is an advantage to avoid pile-up. The photon pile-up is potentially a problem when observing bright sources.

Once the pile-up occurs, both image and spectral data are distorted. The energy spectrum tends to become harder for the following reason. In most cases, the soft photon flux is much larger than the hard photon flux. This means that, when pile-up occurs, soft photons tend to pile up rather than the hard photons. When soft photons pile up, they may be either discarded as a non-X-ray event or regarded as a single hard photon. This results in a flux decrease in the soft band and a flux increase in the hard band, which results in the spectral hardening. Because the decrease of the soft photons overwhelms the increase of the hard photons, the pile-up tends to decrease the total photon flux. In an extreme case, all events may be discarded as non-X-ray events at the image center, and the local photon flux becomes effectively zero. This means that a point source image would have a hole at the center. This is the simplest method to detect the photon pile-up.

The impact of the pile-up on the energy spectrum is different from source to source. For example, if one tries to look for a weak hard tail in the energy spectrum from a soft source, the photon pile-up has to be strictly removed as it can easily mimic the hard tail. On the other hand, a heavily absorbed source with a hard spectrum may be rather insensitive to the photon pile-up.

The pile-up could be a problem when observing a bright point source; the pile-up does not usually come up when observing an object extended more than the point spread function of the XRT. However, to the pile-up, we reduce the exposure by selecting a Clock mode with some options in many cases. We give a detailed estimation below, but the results can be summarized as follows: In practice, point sources with < 12 counts/s can be observed in the Normal mode without any options (Full Window). If point sources have counting rates larger than 12 counts/s, guest observers first should consider to observe the targets at the HXD nominal position rather than the XIS nominal position; the change of the aim point would decrease the counting rates by 10%. If the change of the aim point is not enough, guest observers should think of the window and/or the burst options. Unfortunately, point sources with > 710 counts/s cannot be observed by the XIS without the pile-up. Figure 4.8 shows the range of the incident counting rate that we can observe without the pile-up. A detailed estimation of photon pile-up is discussed in Yamada et al. (2012).

4.1.4 Hard X-ray Detector (HXD)

The Hard X-ray Detector (HXD, Figure 4.9) is a non-imaging collimator instrument, which is a combination of silicon PIN diodes (PIN) and GSO scintillators (GSO) covering the 10–600 keV energy range. It has been developed jointly by the University of Tokyo, Aoyama Gakuin University, Hiroshima University, ISAS/JAXA, Kanazawa University, Saitama University, SLAC, and RIKEN. Its main purpose is to extend the bandpass of the Suzaku observatory to the

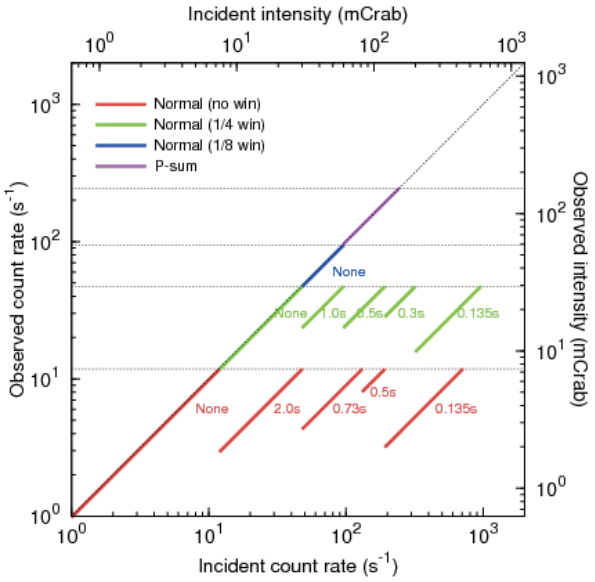

Figure 4.8: Incident versus observed count rates of a point source for the FI sensor. The thick colored lines show the range that can be observed without strong pile-up for a given window option (defined by the figure legend) and burst option (defined by the time values $t_{\rm b}$ indicated in the figure). Note that the window frame times $t_{\rm w}$ are 8, 2, and 1s for the full, 1/4, and 1/8 window options, respectively, with exposures per frame of $t_{\rm b}$ for a given burst option.

highest feasible energies, thus allowing broad-band studies of celestial objects.

The HXD sensor (HXD-S) is a compound-eye detector instrument, consisting of 16 main detectors (arranged as a 4 × 4 array) and the surrounding 20 crystal scintillators for active shielding. Each unit actually consists of two types of detectors: a GSO/BGO phoswich counter, and 2mm-thick PIN silicon diodes located inside the well, but in front of the GSO scintillator. The PIN diodes are mainly sensitive below ∼60 keV, while the GSO/BGO phoswich counter (scintillator) is sensitive above ∼40 keV. The scintillator signals are read out by photomultiplier tubes (PMTs). A schematic drawing of the HXD is given in Figure 4.10. The HXD features an effective area of ∼160 cm^2 at 20 keV, and ∼ 260 cm^2 at 100 keV (Figure 4.11). The energy resolution is ∼4.0 keV (FWHM) for the PIN diodes, and $7.6/\sqrt{E}$% (FWHM) for the scintillators, where E is energy in MeV. The HXD time resolution is 61 μs. The performance of HXD is summarized in Table 4.4

GSO/BGO Counter Units

Each main detector unit is of a well-type design with active anti-coincidence shields. The shields and the coarse collimator itself are made of Bismuth Germanate (BGO, Bi4Ge3O12) crystals, while the X-ray sensing material “inside the well” consists of Gadolinium Silicate (GSO, Gd2SiO5(Ce)) crystals. The aspect ratio of the coarse collimators yields an acceptance angle for the GSO of 4°.5 (FWHM). Each unit forms a 2 × 2 matrix, containing four 24 mm × 24 mm, 5mm thick GSO crystals, each placed behind a PIN diode. BGO crystals are also placed

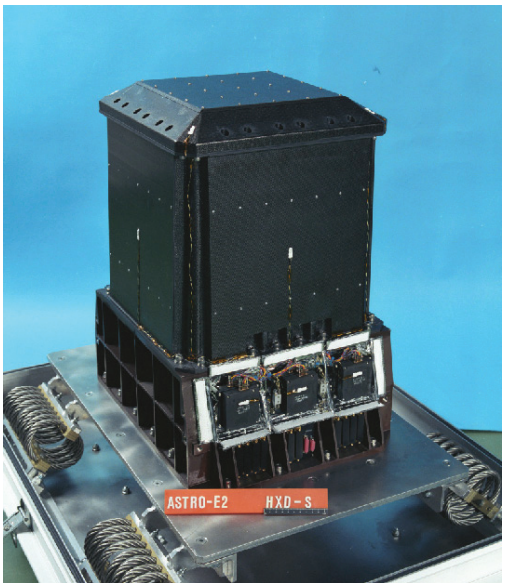

Figure 4.9: Picture of the HXD (Takahashi et al., 2007).

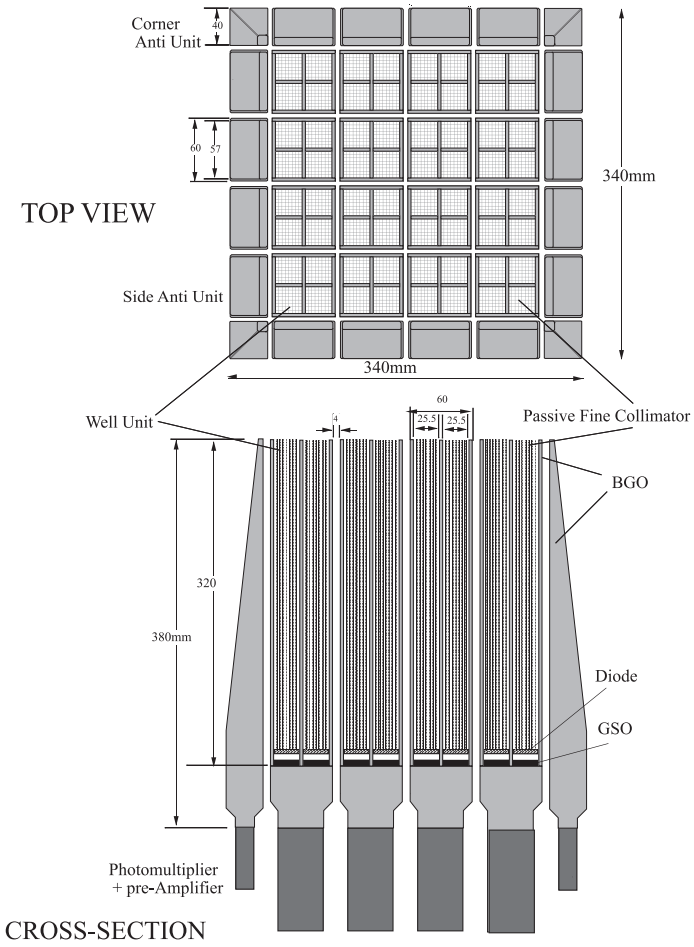

Figure 4.10: Schematic view of the HXD (Takahashi et al., 2007).

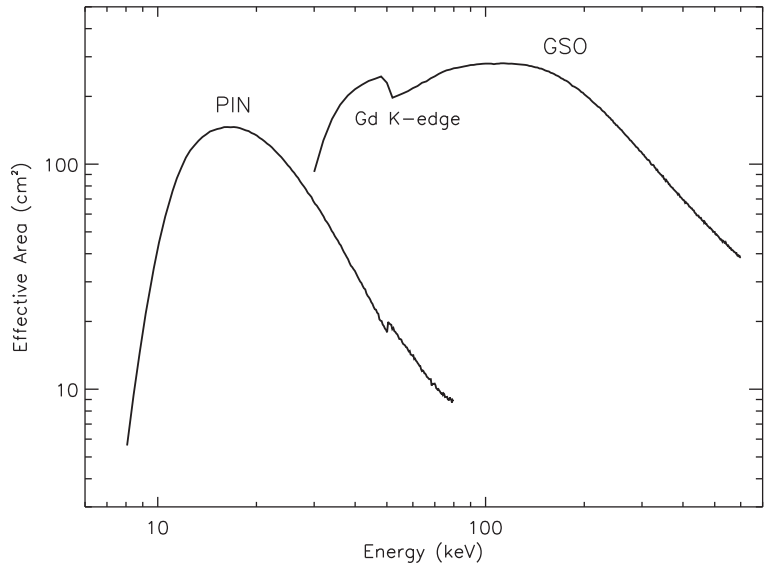

Figure 4.11: Total effective area of the HXD detectors, PIN and GSO, as a function of energy (Takahashi et al., 2007).

Table 4.4: Performance of the HXD (Takahashi et al., 2007).

HXD	Field of view	$34' \times 34'$ ($\leq$ 100 keV) / $4°.5 \times 4°.5$ ($\geq$ 100 keV)
	Bandpass	10–70 keV (PIN) / 40–600 keV (GSO)
	Energy resolution	$\sim$3.0 keV (PIN) / $7.6/\sqrt{E_{\rm MeV}}$% (GSO)
	Effective area	$\sim$160 cm^2 at 20 keV / $\sim$260 cm^2 at 100 keV
	Time resolution	61 μs or 31 μs
HXD-WAM	Field of view	2π (non-pointing)
	Bandpass	50 keV–5 MeV
	Effective area	800 cm^2 at 100 keV / 400 cm^2 at 1 MeV
	Time resolution	15.625 ms or 31.25 ms for GRB, 1 s for All-Sky-Monitor

underneath of the GSO sensors, and thus each well is a five-sided anti-coincidence system. The effective thickness of the BGO active shield is about 6 cm for any direction from the PIN and GSO, except for the pointing direction.

The reason for the choice of the two different crystals for the sensor and the shield is dictated by the large stopping ability of both, yet the very different rise/decay times, of ∼700 ns for BGO, and ∼120 ns for GSO, at a working temperature of −20°C. This allows for an easy discrimination of the shield vs. X-ray sensor signals, where a single PMT can discriminate between the events at the two types of scintillators. Any particle events or Compton events that are registered by both the BGO and GSO can be rejected by this phoswich technique, utilizing custom-made pulse-shaping LSI circuits.

PIN-Si Dinodes

The low energy response of the HXD is provided by 2 mm thick PIN silicon diodes, placed in front of each GSO crystal. The geometrical area of the diodes is 21.5 × 21.5 mm^2, while the effective area is limited to ∼16.5 × 16.5 mm^2 by the guard ring structure. The temperature of the PIN diodes is controlled to be -15 ± 3°C to suppress electrical noise caused by the leakage current, and they are almost fully depleted by applying a bias voltage of ∼500 V. The PIN diodes absorb X-rays with energies below ∼70 keV, but gradually become transparent at harder X-rays, which reach and are registered by the GSO detectors. The X- rays are photoelectrically absorbed in the PIN diodes, and the signal is amplified, converted to digital form, and read out by the associated electronics. The PIN diodes are of course also actively shielded from particle events by the BGO shields, as they are placed inside the deep BGO wells. In addition, in order to reduce contamination by the cosmic X-ray background, passive shields called “fine collimators” are inserted in the well-type BGO collimator above the PIN diodes. The fine collimator is made of 50 μm-thick phosphor-bronze sheets, arranged to form 8 × 8 square meshes, 3 mm wide and 300 mm long. The passive fine collimators define a $34' \times 34'$ FWHM square opening below ∼100 keV. Thus, the field of view of the PIN is $34' \times 34'$ (Table 4.4).

Energy response of HXD-PIN and HXD-GSO

The energy response of HXD-PIN have been constructed for individually for the 64 PIN diodes, through Monte Calro simulations using GEANT4 toolkit. The bias voltage on-board and low energy threshold in the ground processing of various subsets of PIN units have been adjusted since launch to reduce noise events. This changes the characteristics of these PIN units in several discrete steps.

The energy response of HXD-GSO was also produced using GEANT4, in the sane way as that of HXD-PIN. However, there is an apparent change in the energy scale of HXD-GSO. Recently, the in-orbit calibration of HXD-GSO is improved by HXD team (Yamada et al.,

2011). They updated the data processing, the response, and the auxiliary files of GSO, and reproduced the HXD-PIN and HXD-GSO spectra of the Crab Nebula over 12–300 keV by a broken power-law with a break energy of ∼110 keV.

In-Orbit HXD Background

Although the HXD is a non-imaging instrument, its instantaneous background can be reproduced through modeling, without requiring separate off-source observations. The HXD has been designed to achieve an extremely low in-orbit background (∼10–4 cps cm^{-2} keV^{-1}), based on a combination of novel techniques: (1) the five-sided tight BGO shielding as mentioned above, (2) the use of the 20 shielding counters made of thick BGO crystals which surround the 16 main GSO/BGO counters, (3) sophisticated on-board signal processing and on-board event selection, employing both high-speed parallel hardware circuits in the analog electronics, and CPU-based signal handling in the digital electronics, and (4) the careful choice of materials that do not become strongly activated under in-orbit particle bombardment. Finally, (5) the narrow field of view below ∼100 keV defined by the fine collimator effectively reduces both the CXB contribution and the source confusion.

The non X-ray background (NXB) of the PIN diodes, measured in orbit, is plotted in the left panel of Figure 4.12. The average background count rate summed over the 64 PIN diodes is ∼0.6 counts s^{-1}, which is roughly equal to an intensity of 10 mCrab (1 Crab means the X-ray flux of Crab nebula, which is considered as good standard light source in a X- ray regime). In addition, almost no long-term growth has been observed in the PIN-NXB during the first three years of Suzaku, thanks to the small amount of activation in silicon. In contrast, as shown in the right panel of Figure 4.12, a significant long-term increase caused by in-orbit activation has been observed for the GSO-NXB, especially during the early phase of the mission. The background spectrum of the GSO contains several activation peaks, with intensities exponentially increasing with their half-lives.

Figure 4.13 illustrates the comparison between detector backgrounds of several hard X-ray missions. The lowest background level per effective area is achieved by HXD in an energy range of 12–70 and 150–500 keV. The in-orbit sensitivity of the experiment can be roughly estimated by comparing the background level with celestial source intensities indicated by dotted lines. Below 30 keV, the level is smaller than 10 mCrab, which means a sensitivity better than 0.3 mCrab can be obtained, if an accuracy of 3% is achieved in the background modeling.

Since the long-term variation of both PIN-NXB and GSO-NXB can be expected to be stable, the main uncertainties of the background come from temporal and spectral short-term variations. As shown in Figure 4.14, the PIN-NXB displays significant short-term variability, with a peak-to-peak amplitude of a factor of 3, anti-correlated with the Cut-Off Rigidity (COR) over the orbit. Since the COR affects the flux of incoming primary cosmic-ray particles, most of the PIN-NXB is considered to originate in the secondary emission produced by interactions between cosmic-ray particles and materials surrounding the detector. When a selection criterion

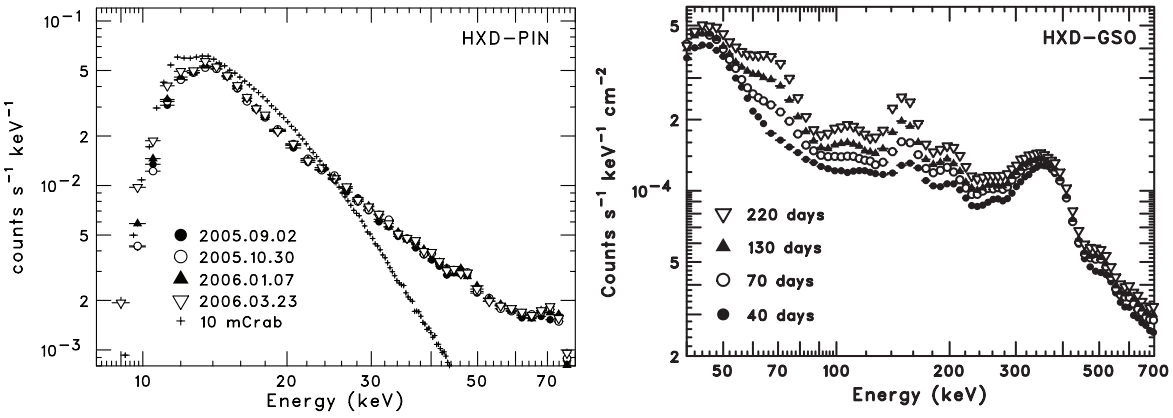

Figure 4.12: (Left) Comparison of four average NXB spectra measured by HXD-PIN, on 4 occasions separated by two months (Kokubun et al., 2007). Each observation has an exposure longer than two days. The Crab spectrum, scaled down by two orders of magnitude, are also shown. (Right) Evolution of the averaged GSO-NXB spectra during the first half year after the launch.

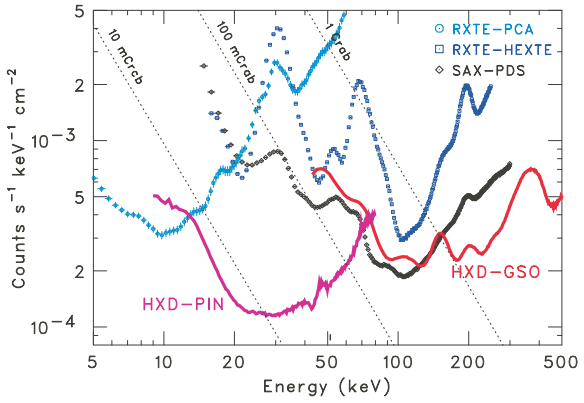

Figure 4.13: Comparison of the in-orbit detector background of PIN/GSO, averaged over 2005 August to 2006 March and normalized by individual effective areas (Kokubun et al., 2007). The dotted lines indicate 1 Crab, 100 mCrab, and 10mCrab intensities.

of COR > 6, a standard value used in the pipeline processing, is applied for the event extraction, the amplitude decreases to a factor of ∼2. During this temporal variation of the PIN-NXB, its spectral shape also changes slightly (larger deviations from the average are observed at a higher energy range, Kokubun et al. (2007)). In case of the GSO-NXB the temporal variation differs for different energy bands, as shown in the right panel of Figure 4.14. In the lowest energy range a rapid decline after the SAA passage is clearly observed, in addition to a similar anti-correlation with the COR. All these temporal and spectral behaviors have to be properly handled in the background modeling.

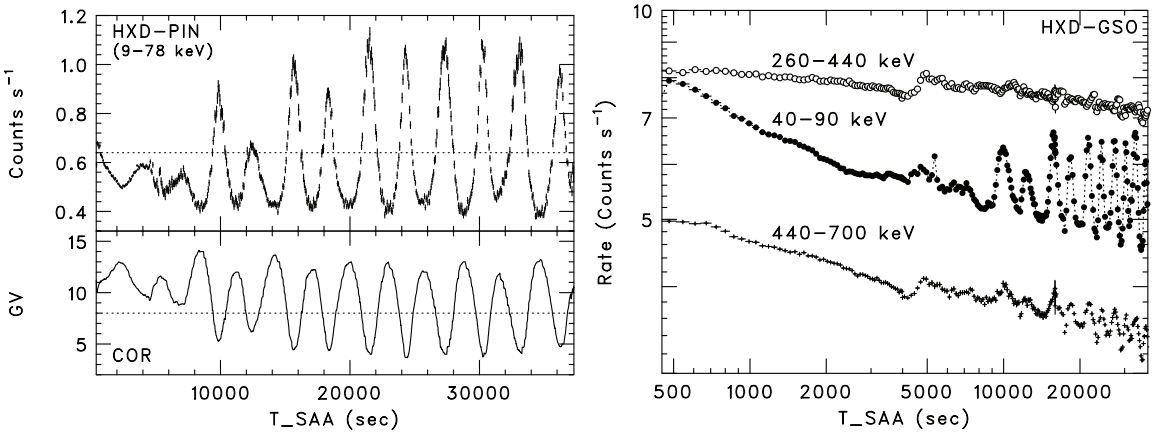

Figure 4.14: Light curves of the PIN- and GSO-NXB folded with an elapsed time from the SAA (T_SAA) (Kokubun et al., 2007).

Background Modeling

As is the case for every non-imaging instrument (and in particular, for those sensitive in the hard X-ray range), the limiting factor for the sensitivity of the HXD is the reproducibility of the background estimation. To make sufficiently accurate modeled NXB, we utilize the two methods.

1. PINUDLCUNIT: One method employs the database which is made by the data of Earth occultation. The parameter of this database is $\mathrm{PINUD}_{\mathrm{buildup}}$ defined as

$$\mathrm{PINUD}_{\mathrm{buildup}}(t) = \int_{-\infty}^{t} \mathrm{PINUD}(t_0) \exp\left(\frac{t_0 - t}{\tau}\right) dt_0 \tag{4.1}$$

2. LCFITDT: The other one, called “tuned” method, predicts the NXB count rates of individual energy bands, based on an empirical background model (Fukazawa et al., 2009). Although this method is released 1.0–1.5 month after the observation, LCFITDT develop more precise predictions of NXBs. The reproducibility of PIN and GSO NXB are shown at Table 4.5 and Table 4.6 (Fukazawa et al., 2009).

Table 4.5: Standard deviation (1σ) of residuals between the PIN Earth data and model (Fukazawa et al., 2009).

15–40 keV	10 ks		20 ks		40 ks	
	PINUDLCUNIT	LCFITDT	PINUDLCUNIT	LCFITDT	PINUDLCUNIT	LCFITDT
Standard deviation (σ)	3.75%	2.31%	3.23%	1.72%	2.96%	0.99%
Statistical error ($\sigma_{\rm stat}$)	1.83%		1.36%		0.93%	
Systematic error ($\sigma_{\rm sys}$)	3.27%	1.40%	2.93%	1.05%	2.81%	0.34%
40–70 keV	10 ks		20 ks		40 ks	
	PINUDLCUNIT	LCFITDT	PINUDLCUNIT	LCFITDT	PINUDLCUNIT	LCFITDT
Standard deviation (σ)	5.53%	4.92%	4.34%	3.51%	3.39%	2.87%
Statistical error ($\sigma_{\rm stat}$)	4.03%		3.01%		2.03%	
Systematic error ($\sigma_{\rm sys}$)	3.78%	2.82%	3.12%	1.81%	2.71%	2.02%

Table 4.6: Standard deviation (1σ) of residuals between the GSO Earth data and model in each energy band (Fukazawa et al., 2009).

	50–100 keV	100–200 keV	200–300 keV	300–500 keV
Standard deviation (σ)	0.72%	0.59%	0.87%	0.71%
Statistical error ($\sigma_{\rm stat}$)	0.40%	0.36%	0.46%	0.34%
Systematic error ($\sigma_{\rm sys}$)	0.60%	0.47%	0.74%	0.63%

4.2 Rossi X-ray Timing Explorer/All Sky Monitor

The Rossi X-ray Timing Explorer (RXTE) was launched on December 30, 1995. The satellite is designed to explore the variability of X-ray sources, which were the fast-moving, high-energy worlds of black holes, neutron stars, X-ray pulsars and X-ray bursts, using its good time resolution in combination with moderate spectral resolution. Time scales from microseconds to months are covered in a wide energy range from 2 to 250 keV. The mission carries two pointed instruments, the Proportional Counter Array (PCA, Jahoda et al. (2006)) which covers the lower part of the energy range (3–20 keV), and the High Energy X-ray Timing Experiment (HEXTE, Rothschild et al. (1998)) covering the upper energy range (18–250 keV). These instruments are equipped with collimators yielding a FWHM of one degree. The spacecraft was operating in a low-earth circular orbit at an altitude of 580 km, corresponding to an orbital period of about 90 minutes. Figure 4.15 shows the schematic view of RXTE.

In addition above two instruments, RXTE carries the All-Sky Monitor (ASM, Levine et al. (1996)) that scans about 80% of the sky every orbit, allowing monitoring at the shortest time scales of 90 minutes (and longer). The ASM consists of three Scanning Shadow Cameras (SSCs) whose the energy range is 2–10 keV. Figure 4.16 shows a schematic view of the SSC. Each SSC equips a one-dimensionally position-sensitive proportional counter (PSPC) with Xenon for the target gas. The PSPC is used to measure the displacements and strengths of the shadow patterns cast by X-ray sources within the field of view, and thereby to infer the directions to and intensities of the sources. The instrumental properties of ASM are summarized in Table 4.7.

ASM results was being used to alert observers to the appearance of transients and to other time-variable phenomena and to record long-term intensity histories of ∼150 bright X-ray sources. For the convenience of users, an overview of ASM data is published on the web site. Originally designed for a required lifetime of two years with a goal of five, RXTE passed that goal and and completed 16 years of observations before being decommisioned on January 5, 2012.

Table 4.7: ASM instrumental parameters

Energy range	2–12 keV
Time resolution	80% of the sky every 90 min
Spatial resolution	3' × 15'
Number of shadow cameras	3 each with 6 × 90 degrees FOV
Collecting area	90 cm^2
Detector	Xenon proportional counter, position-sensitive
Sensitivity (for one 90 s "dwell")	30 mCrab

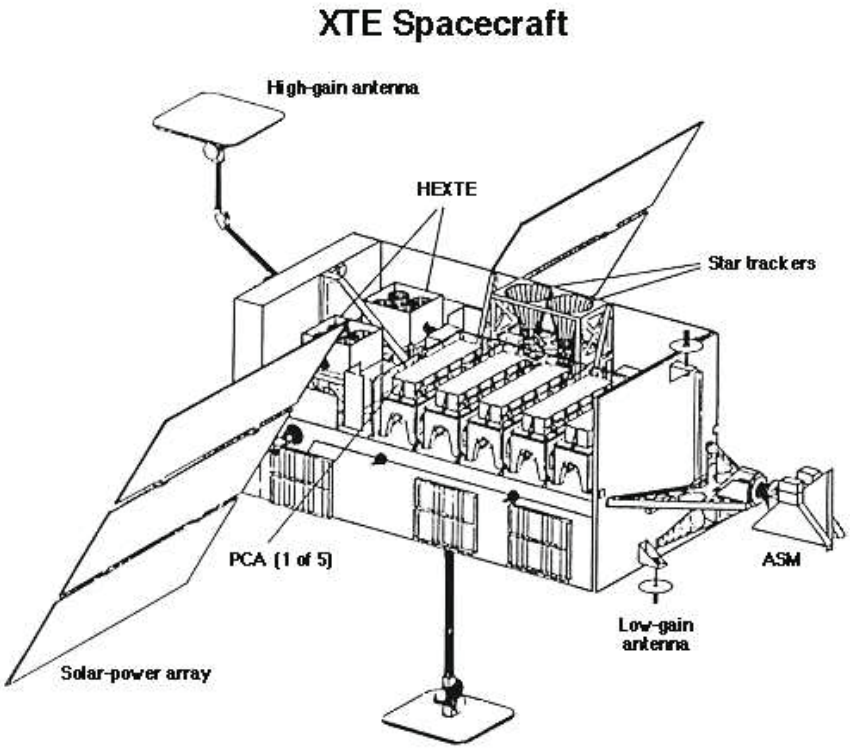

Figure 4.15: The schematic view of RXTE.

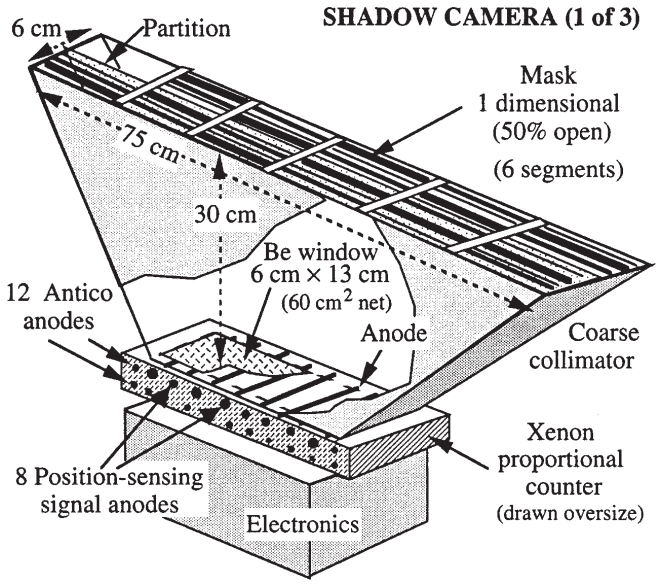

Figure 4.16: Diagram of a single ASM shadow camera.

Chapter 5

OBSERVATIONS AND DATA REDUCTION

5.1 Observations

Her X-1 was observed seven times with Suzaku from 2005 through 2010, as summarized in Table 5.1[1]. The XIS nominal pointing position was adopted in 2008 (Obs. 3), and the other six observations were performed at the HXD nominal pointing position. The XIS was operated with the "1/8 window" option in Obs. 1 and the 0.1 s burst mode in Obs. 3. In the other observations, the "1/4 window" option was employed with a 2 s time resolution. In the former half of Obs. 2, the XIS0, 2, and 3 data were not acquired due to an operation error for 10 ks, and these three sensors were operated in the p-sum mode with a time resolution of 7.8 ms for 6 ks. In Obs. 4–7, XIS3 was also operated in p-sum mode. Since XIS2 became suddenly unusable on 2006 November 9, we did not use XIS2 data in and after Obs. 3.

Figure 5.1 shows the Suzaku observation periods of the light curves of Her X-1 obtained with RXTE ASM[2]. Obs. 1–3 were taken in the main-on phase of the 35 day period of Her X-1, while Obs. 4–7 were obtained at the rising- and falling-edge of the main-on phase.

In this study, we performed XIS data reduction for only five (Obs. 2, 4, 5, 6 and 7) out of seven Suzaku observations because of the detector response uncertainty for the "1/8 window" mode and a poor effective exposure for the "0.1 s burst" mode.

[1] In the following chapters 5, 6, 7, and 8, we have referred to Asami et al. (2014).
[2] ⟨http://xte.mit.edu/asmlc/⟩

Table 5.1: Suzaku observations of Hercules X-1

Obs#	Start (UT)	End (UT)	On-source time	XIS obs. mode		Pointing	Orbital	35-d
			[ks]	window	clock		phase*	phase†
1	2005-10-05 15:12	2005-10-06 10:25	69.2	1/8 win.	normal	HXD	0.05–0.52	0.12
2	2006-03-29 18:12	2006-03-30 15:22	76.2	1/4 win.	normal	HXD	0.06–0.58	0.20
				full	p-sum (XIS0, 2, 3)‡			
3§	2008-02-21 15:50	2008-02-22 11:40	71.4	full win.	0.1 s burst	XIS	0.19–0.67	0.19
4	2010-09-21 23:45	2010-09-22 10:47	39.1	1/4 win.	normal	HXD	0.02–0.29	0.05
				full	p-sum (XIS3)			
5	2010-09-22 18:42	2010-09-23 05:55	40.4	1/4 win.	normal	HXD	0.49–0.76	0.07
				full	p-sum (XIS3)			
6	2010-09-28 18:34	2010-09-29 05:40	40.0	1/4 win.	normal	HXD	0.01–0.29	0.24
				full	p-sum (XIS3)			
7	2010-09-29 16:37	2010-09-30 05:25	46.1	1/4 win.	normal	HXD	0.55–0.87	0.26
				full	p-sum (XIS3)			

* For the orbital phasing we used the ephemeris of Still et al. (2001) and set phase 0.0 corresponding to the middle of X-ray eclipse.
† For the 35-d phasing we employed the same method as Zane et al. (2004).
‡ The p-sum mode was operated in a part of the observation.
§ The XIS2 was not operated after 2006 November 9.

52

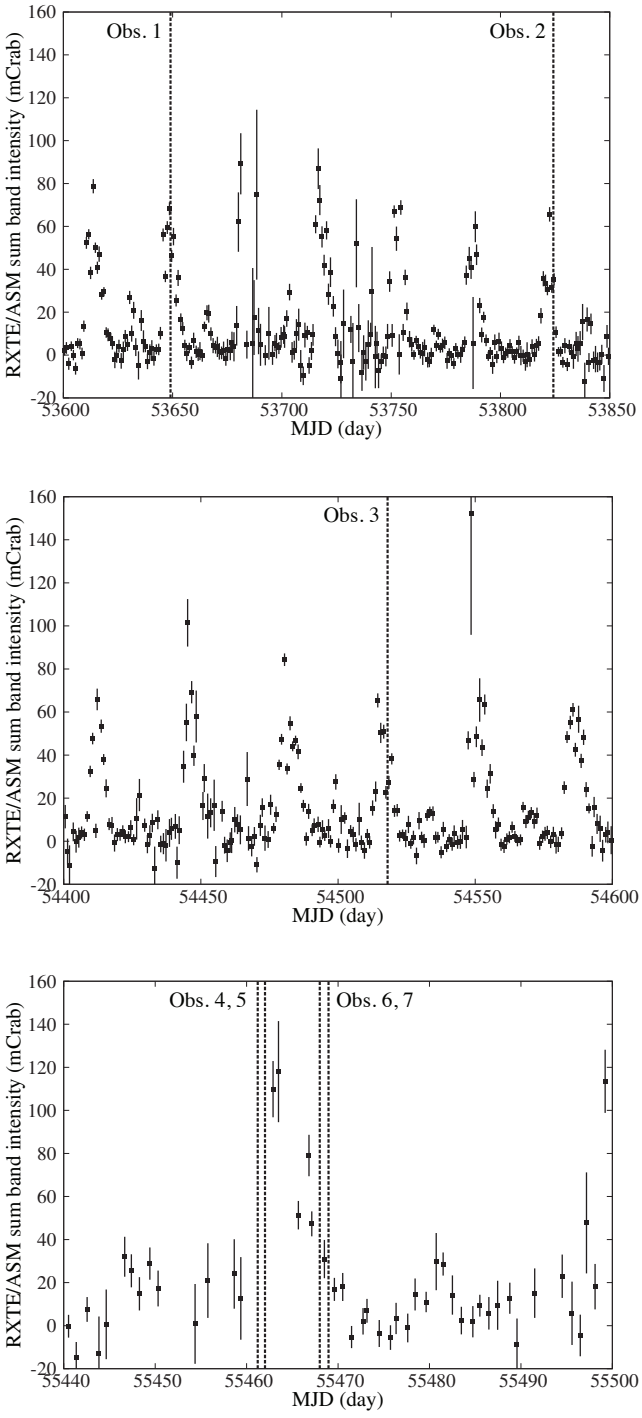

Figure 5.1: The 2–10 keV RXTE/ASM light curve of Her X-1. Suzaku observations are indicated by dashed lines. The intensity of 100 mCrab corresponds to $\sim$7.5 count s^{-1} of the 2–10 keV ASM count rate.

Table 5.2: Net exposure of XIS sensors, PIN, and GSO after event screenings, excluding the dip phase.

Obs#	Exposure [ks]					
	XIS0	XIS1	XIS2	XIS3	PIN	GSO
2	21.4	29.9	21.4	21.4	24.7	24.7
4	19.9	19.9	–	–	16.4	16.4
5	19.3	19.4	–	–	16.0	18.6
6	21.4	21.4	–	–	17.8	17.8

5.2 Data Reduction

5.2.1 Data Reduction of XIS

We used XSELECT to extract XIS images, light curves, and spectra from the XIS cleaned event files, which were screened with the standard selection criteria as described by the Suzaku ABC guide[3]. As shown in Figures 5.3 and 5.4, the source region was a rectangle of $4' \times 8'$ centered on the source. The background events were extracted from a rectangle region of $4' \times 2'$, on an edge of the effective area of CCD. To eliminate pile-up events, we excluded the core of the CCD image with a radius of 0.8–1.0 arcmin, which was large enough to reduce the pile-up fraction below $\sim$1% (Yamada et al., 2012).

Figure 5.2 shows the background-subtracted 0.4–10 keV XIS0 light curves of Obs. 2, 4, 5, 6 and 7. As shown in Figures 5.2 (a), (c) and (d), the dips, when the X-ray intensity suddenly dropped (Giacconi et al., 1973; Klochkov et al., 2008; Endo et al., 2000), were seen in the latter part of Obs. 2 and 5, and over the entirety of Obs. 7. Nakazawa et al. (2010) shows that the spectra in the dip phase of Obs. 2 indicated the existence of absorption materials with a high column density of $\sim 10^{23}$ cm^{-2}. More complex features, such as the O VII edge, were also seen. Since we did not pursue the origin of such absorption materials, we excluded those dip events from the analysis. The net exposures of Obs. 2, 4, 5, and 6 were 19.4–29.9 ks, as summarized in Table 2. Since the light curves were flat during Obs. 2, we considered that there is no spectral variation. Thus, X-ray spectra were extracted by using data over the each net exposure time although the exposures were different between XIS-FI and XIS-BI in Obs. 2.

We used `xisrmfgen` and `xissimarfgen` to create the XIS response and auxiliary files, respectively. Following the recommendations in the Suzaku ABC guide, we generated 400,000 photons to simulate the auxiliary file.

[3] ⟨http://heasarc.nasa.gov/docs/suzaku/analysis/abc/⟩

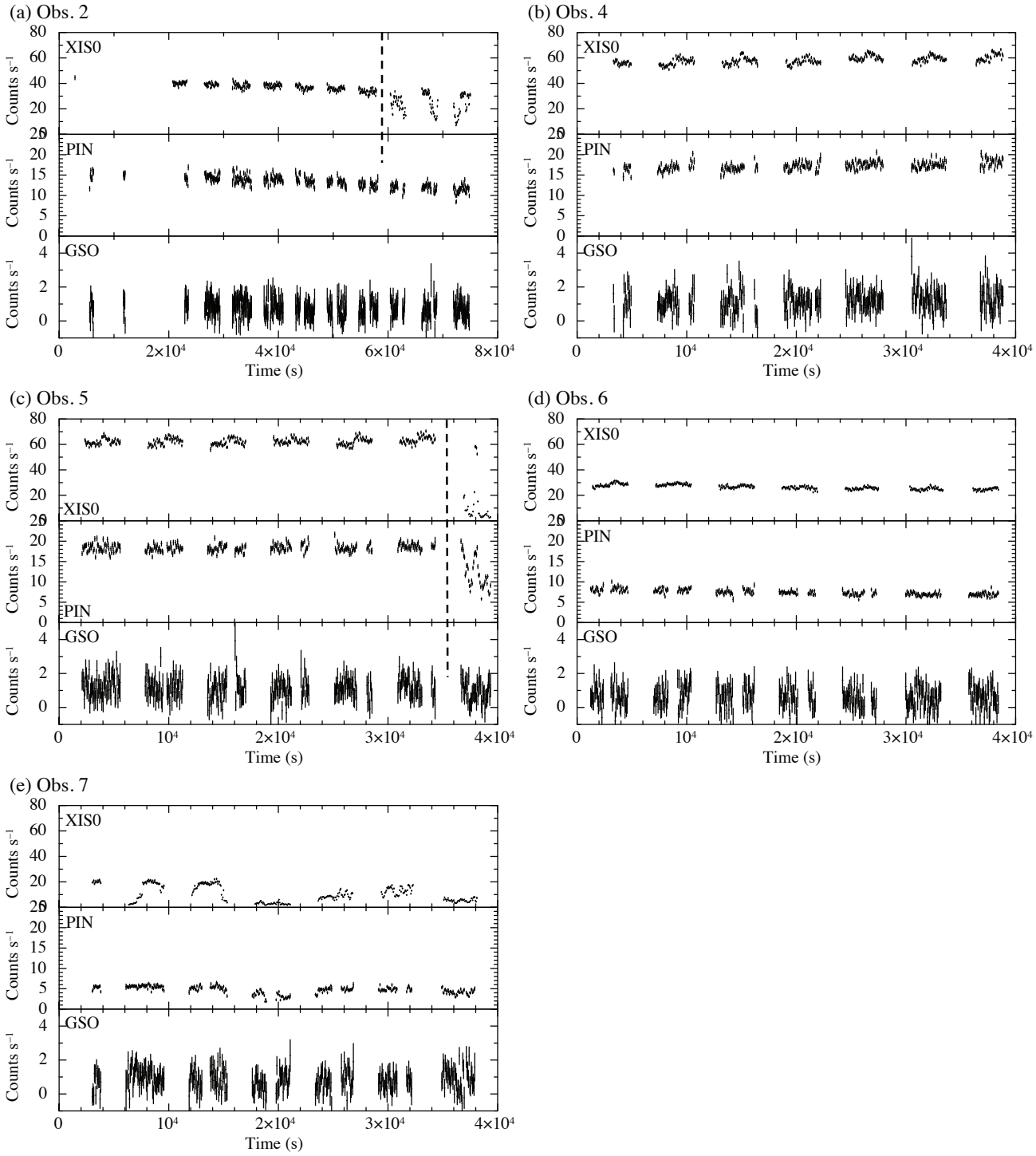

Figure 5.2: (a) The background-subtracted XIS0, PIN, and GSO light curves of Obs. 2 (2006). From the top, the three panels refer to XIS0 (0.4–10 keV), PIN (10–70 keV), and GSO (50–100 keV). (b)–(e) The same as (a), but these were obtained on Obs. 4 (2010 first), 5 (2010 second), 6 (2010 third), and 7 (2010 fourth). The bin size of the each detector is 64 s. Dashed lines in Obs. 2 and 5 indicate the boundary between the no-dip and dip phases.

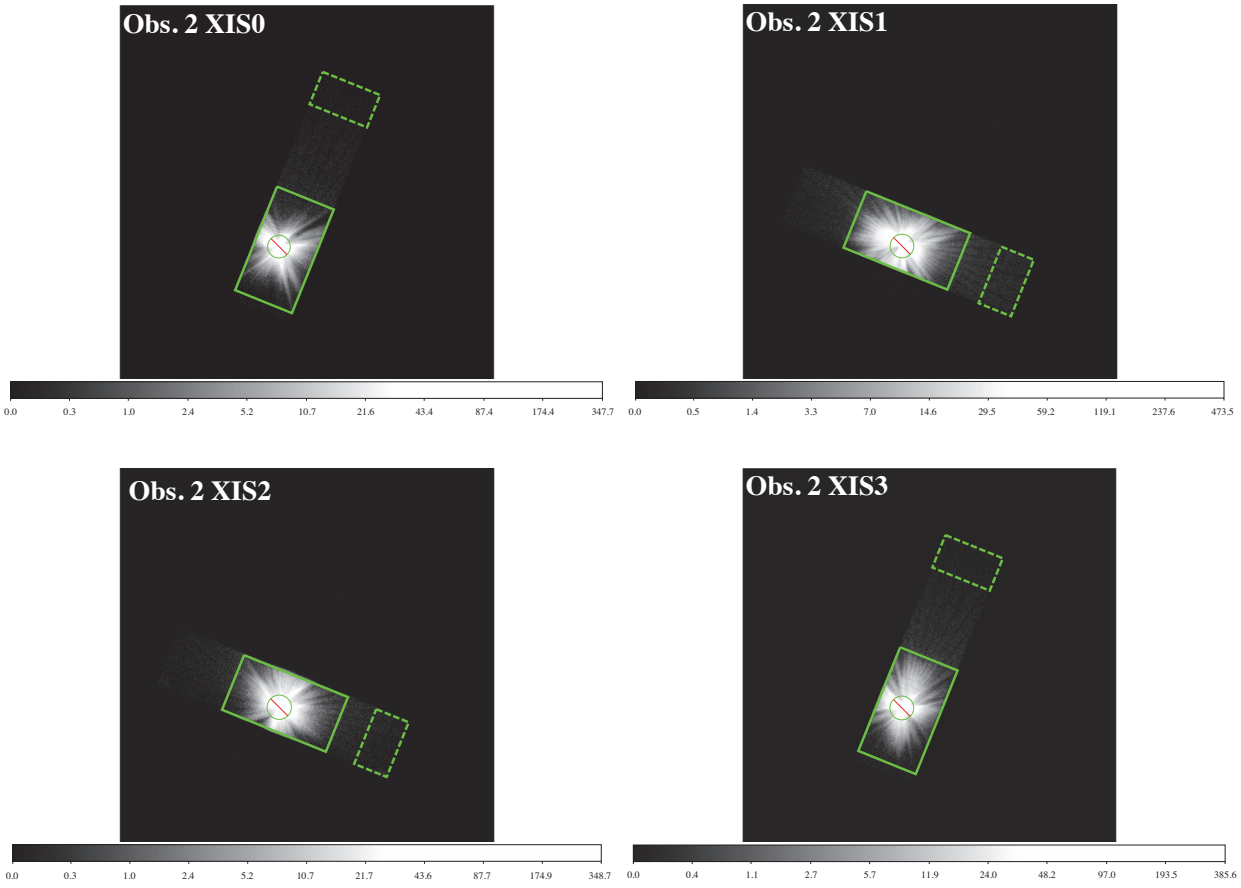

Figure 5.3: Source (solid) and background (dashed) regions for analysis of Suzaku observations of Her X-1. Circle regions were excluded from the source regions to eliminate pile-up events.

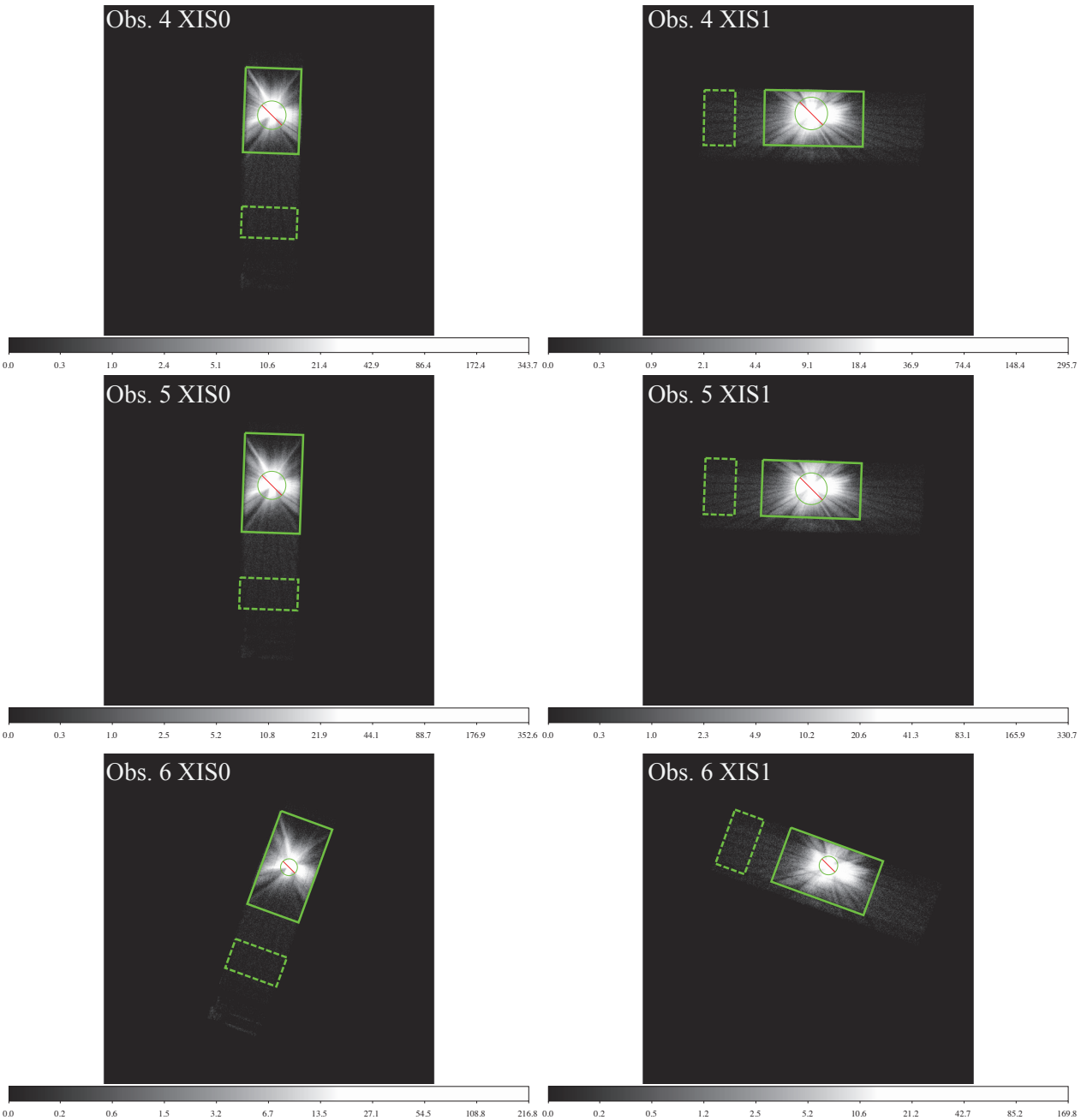

Figure 5.4: The same as Figure 5.3, but for analysis of Obs.4, 5, and 6.

5.2.2 Date Reduction of HXD

Because HXD is a non-imaging detector, we first confirmed absence of the contaminating sources. According to the INTEGRAL General Reference Catalog[4], there is no high energy source in the PIN and GSO field of view (< 100 keV) other than Her X-1.

We applied `aepipeline` version 1.1.0 to the HXD raw data to extract the cleaned events, which were screened with the following normal selection criteria; (a) the distance from mean pointing position is less than 1.5 arcmin, (b) the time after passage South Atlantic Anomaly should be larger than 500 seconds, (c) the cut-off rigidity is larger than 6 GeV, (d) the target object should be above the Earth rim by at least 5°. The details are shown in the Suzaku ABC guide. We created the background-subtracted and dead-time corrected light curves of PIN (10–70 keV) and GSO (50–100 keV) from the cleaned event files, the pseudo (PSE) event files used in the dead-time correction, and non-X-ray background (NXB) event files with `hxdpinxblc` for PIN and `hxdgsoxblc` for GSO. We used the version 2.0 "tuned" background event files for PIN[5], and the NXB files version 2.5 and 2.6 for the GSO data[6] in 2006 and 2010, respectively. The second and third panels of figure 5.2 display the light curves of PIN and GSO. Only in the PIN data of Obs. 5 did the dip appear, so those events were excluded along with XIS. The net exposure of HXD was 16–25 ks, and the average 15–70 keV PIN and 50–100 keV GSO intensities were 5.4–13.7 counts s^{-1} and 0.12–0.54 counts s^{-1}, respectively.

We adopted `hxdpinxbpi` to create the source and background PIN spectra, which produced the dead-time corrected PIN source spectrum and the PIN background spectrum using the cleaned, PSE, and NXB event files. The tool first merged the good time interval (GTI) file with the cleaned event and background files, and extracted the source and NXB background spectra using the GTI file. It next produced simulated cosmic X-ray background (CXB) events. Finally, it applied the dead-time correction to the source spectrum, and the CXB spectrum was added to the NXB spectrum. We similarly used `hxdgsoxbpi` to generate the source and background GSO spectra.

[4] ⟨http://www.isdc.unige.ch/integral/science/catalogue⟩
[5] ⟨http://www.astro.isas.ac.jp/suzaku/analysis/hxd/pinnxb/pinnxb_ver2.0_tuned/⟩
[6] ⟨http://www.astro.isas.ac.jp/suzaku/analysis/hxd/gsonxb/⟩

Chapter 6

ANALYSIS AND RESULTS

6.1 Spectral Components

Since the results of spectral decomposition can depend on the fitting model, here we estimate the number of components for the broad-band spectrum without the aid of detailed modeling. The spectral ratio of Her X-1 to the Crab nebula is frequently used when searching for the spectral feature line CRSF (dal Fiume et al., 1998; Enoto et al., 2008). In accordance with this method, we derived the ratio of the data (XIS0, PIN and GSO) to the PL model with $\Gamma = 1$, and presented them in Figure 6.1.

The excess below 2 keV indicates that the soft band contains components different from those of the hard band. The ratios below 0.6 keV differed between Obs. 2 and Obs. 4, 5, and 6, suggesting that there are at least two spectral components below 2 keV. In the energy band above 2 keV, the ratios were similar among the observations. This suggests there are three continuum components in each energy band below 0.6 keV, in 0.6–2 keV, and above 2 keV, which agree with past results (Oosterbroek et al., 1997; dal Fiume et al., 1998; Ramsay et al., 2002). In all observations a spectral cutoff and an absorption structure are seen at around 20–30 keV and 30–40 keV, respectively, which was consistent with studies by BeppoSAX, RXTE, INTEGRAL, and NuSTAR (dal Fiume et al., 1998; Coburn et al., 2002; Klochkov et al., 2008; Fürst et al., 2013).

Narrow line features are seen between 6 and 7 keV, which could be separated into two narrow lines (inset of Figure 6.1). The details of analysis of these lines are shown in section 6.2.

Klochkov et al. (2008) showed that the 2.5–20 keV spectra are reproduced by PL and Fe line models. However, in Figure 6.1 there is a broad humped structure around 4–9 keV that does not seem to be described by the PL model except for a narrow peak at 6–7 keV; this implies that some additional components might be required.

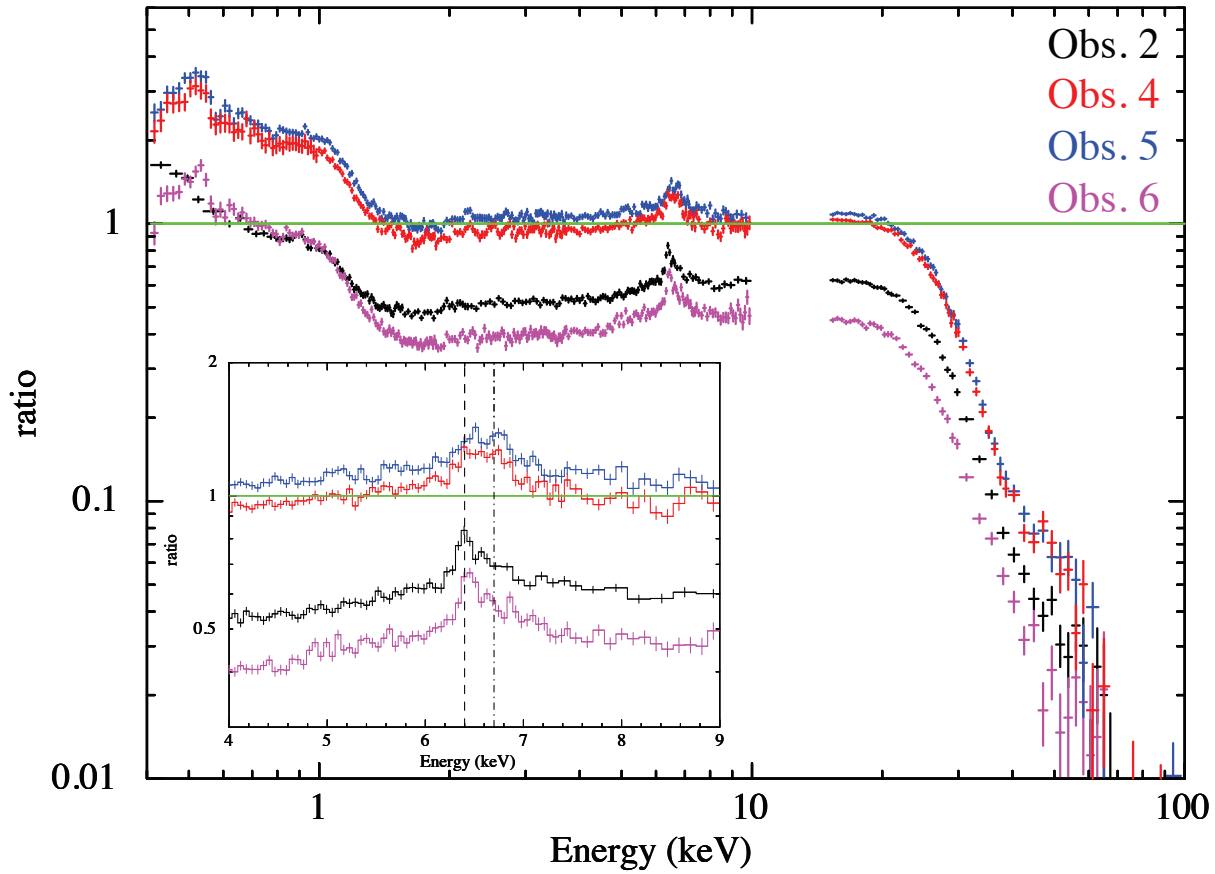

Figure 6.1: Data-to-model ratios of the four Suzaku observations. The PL model with fixed photon index ($\Gamma = 1$) is normalized by the values of Obs. 4. The inset shows an enlargement of the 4–9 keV band. The 6.4 and 6.7 keV bands are indicated by dashed and dash-dotted lines, respectively

6.2 Modeling of the Broad-band Spectra

In addition to the soft excess at around 1 keV and the black body with a temperature of $kT_{\rm BB}$ ∼0.1 keV, we tried three empirical models for the accretion-column emission. Since a widely accepted model describing the accretion-column emission is not established yet, we employed those three empirical models to reveal spectral features independent of the continuum models. The first one is (1) PL with high energy exponential cut-off (HECUT), which was used in the analysis of XMM-Newton and INTEGRAL data (Ramsay et al., 2002; Klochkov et al., 2008). The HECUT model is expressed as

$$f(E) = \begin{cases} 1 & E < E_{\rm cut} \\ \exp[-(E - E_{\rm cut})/E_{\rm fold}] & E > E_{\rm cut}, \end{cases} \tag{6.1}$$

where E is the X-ray energy, $E_{\rm cut}$ is the cut-off energy, and $E_{\rm fold}$ is the folding energy describing the cut-off steepness. The second is broken PL (BPL) with HECUT, which was used to fit the BeppoSAX 0.1–200 keV broad-band data (dal Fiume et al., 1998). The BPL model is written by

$$f(E) \begin{cases} AE^{-\Gamma_1} & E < E_{\rm break} \\ AE^{\Gamma_2-\Gamma_1}(E/1\ {\rm keV})^{-\Gamma_2} & E > E_{\rm break}, \end{cases} \tag{6.2}$$

where f is the photon number flux, Γ_1 and Γ_2 are photon indices, and $E_{\rm break}$ is a spectral breaks ("cut-off energy"). The third one is the negative and positive power-law with exponential cut-off (NPEX), which was proposed by Mihara (1995); Makishima et al. (1999) and used to express the Suzaku HXD spectra of Her X-1 (Enoto et al., 2008). We multiplied the three empirical models by a factor e^{-S}, where S represents the cyclotron scattering cross-section, given as

$$S = \frac{D_{\rm cycl}E^2}{(E - E_{\rm cycl})^2 + W^2} \times \left(\frac{W_{\rm cycl}}{E_{\rm cycl}}\right)^2, \tag{6.3}$$

with $E_{\rm cycl}, D_{\rm cycl}, W_{\rm cycl}$ being the energy, depth, and width of the resonance (Makishima et al., 1999). The second harmonics of CRSF were not taken into account in the model fitting, because Enoto et al. (2008) demonstrated that adding the second harmonics did not improve the fitting quality much. The soft excess and continuum component models were multiplied by the same absorption column density which accounts for the interstellar absorption toward Her X-1. Here we describe details of the analysis of Obs. 2 as a representative for all observations, because its total exposure was the longest. The results of analysis of the other observations are shown in section 6.4.

Figure 6.2 shows the fitting results of the data in the 0.4–100 keV energy band for the three empirical continuum models. The second panels in Figures 6.2 (a2), (b2), and (c2) show the residuals of the soft excess and of the three empirical continuum models from the data. In the spectral fitting, we ignored the 1.6–2.0 keV band which is around the Si K-edge energy

(1.8 keV), and 10–15 keV energy band in the PIN data because of calibration uncertainty and electrical noise. We ignored the XIS0, 2, and 3 data below 0.7 keV due to the calibration uncertainty from material contamination and added systematic errors at a level of 1% to all XIS, PIN, GSO spectral in order to include for uncertainties in the detector response. The XIS0, 2 and 3 (FI chips) data were added using `addascaspec`, which add the source spectra, background spectra, and response files with appropriate and consistent weighting. The cross-normalization between FI and BI chips was set free in the fitting to cope with the calibration uncertainty of the effective area. On the other hand, following the recommendation in the Suzaku ABC guide, the cross normalization between FI and HXD was fixed as 1.18.

In those residuals (Figures 6.2 (a2), (b2), and (c2)), a narrow peak structure is seen at around 6–7 keV, indicating the existence of Fe lines in the spectrum. To reproduce the residuals, we inserted the 6.4 keV and 6.7 keV Fe lines, which were originally discovered by ASCA (Endo et al., 2000), into the fitting models. The center energies of the lines were fixed at 6.4 and 6.7 keV, but the widths and normalizations have been left free in the fit. As shown in Figures 6.2 (a3), (b3), and (c3), the narrow peak in the residual plots at 6–7 keV disappeared, but the entire dataset could not be represented by the soft excess and the continuum models with 6.4 and 6.7 keV Fe lines.

In all accretion-column models, a hump structure still remains around 4–9 keV (Figure 6.2). The reduced chi-square was $\chi^2_\nu(\nu) = 3.47$ (463) for PL×HECUT, 3.15 (461) for BPL×HECUT, and 3.35 (463) for NPEX. The local hump in the residual is statistically significant, which urges us to quantify it in the way of using detailed models.

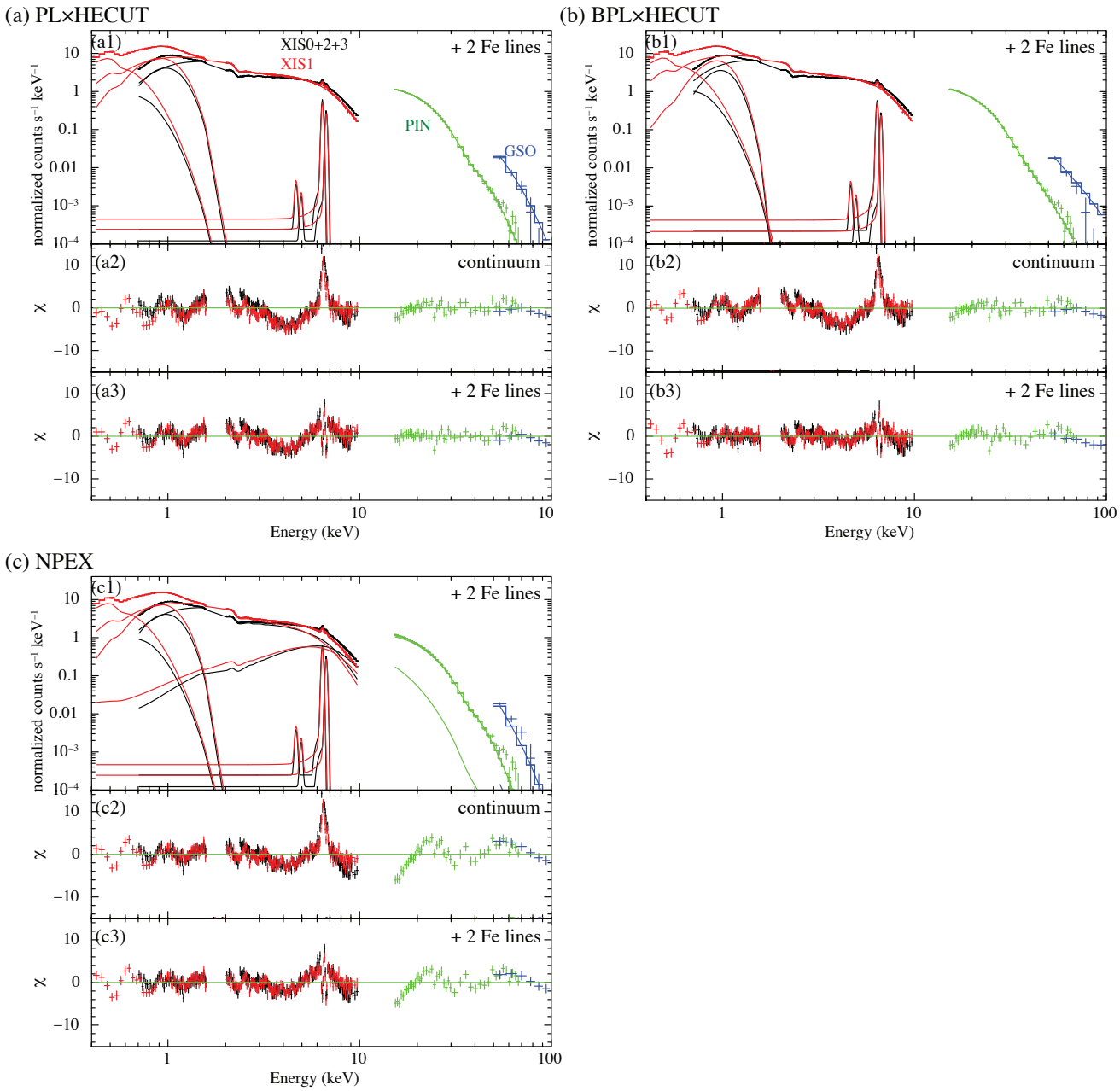

Figure 6.2: Broad-band spectral fitting with different continuum models of Obs. 2 (2006): (a1) PL×HECUT, (b1) BPL×HECUT, and (c1) NPEX. The XIS0+2+3 (black cross), XIS1 (red), HXD-PIN (green), and HXD-GSO (blue) are simultaneously fitted with two narrow Fe lines at 6.4 and 6.7 keV. Corresponding residuals are displayed in (a3), (b3), and (c3). The residuals from each continuum model are shown in (a2), (b2), and (c2).

6.3 Modeling of the 4–9 keV hump

It is likely that such a broad structure around Fe K-line energies can be reproduced by either of a partial covering, reflection, and a broad line model. In this section, we compare these models to search for the plausible model representing the 4–9 keV hump.

6.3.1 Partial Covering model

Cold absorber

To describe the 4–9 keV hump, we first consider a partial covering. According to Endo et al. (2000), the PL component was directly emitted from the accretion column and the highly absorbed PL component resulted from absorption of the emission by blobs of circumstellar accreting matter in the line of sight or from loss due to forward scattering by the accretion disk. Ramsay et al. (2002) also adopted the partial covering model to express the Her X-1 spectra in dim phases of the 35 day period, such as the low and short-on states. We thus tried to fit the spectrum with the accretion-column emission models introduced in Section 6.2, multiplied by a partial covering factor (practically, using the `pcfabs` model in `XSPEC`) , of the form

$$\mathrm{CF}(E) = f \exp[-N_{\mathrm{H}}\sigma(E)] + (1 - f), \tag{6.4}$$

where N_{H} is the equivalent hydrogen column, $\sigma(E)$ is the photo-electric cross-section, and f is the covering fraction.

Figure 6.3 (a1) shows the spectrum of Obs. 2 and NPEX with the partial covering model. Figure 6.3 (a2), (a3) and (a4) present the residuals from PL×HECUT, BPL×HECUT and NPEX with the partial covering model. In the case of PL×HECUT and NPEX, relatively large residuals are seen in the whole energy band. On the other hand, BPL×HECUT with the partial covering model slightly improved the fitting quality $\chi^2_\nu = 1.48$ (459). However, large residuals are still recognized in the 7-9 keV band. These residuals might indicate that the higher energy part of the 4–9 keV hump could not be represented by the partial covering model. We consider that the 4-9 keV hump does not have a sharp structure, and any models including a sharp structure, such as a partial covering model with neutral Fe K-edge at 7.1 keV, cannot reproduce it.

Ionized absorber

To suppress the sharp structure in the partial covering model, we tried ionized partial covering model. We employed `zxipcf`, one of the simplified photo-ionized absorption models implemented in XSPEC (Reeves et al., 2008) to mimic the ionized absorption features. The model is calculated by using Xstar (v2.11), and assumes a single zone absorber with a microturbulent

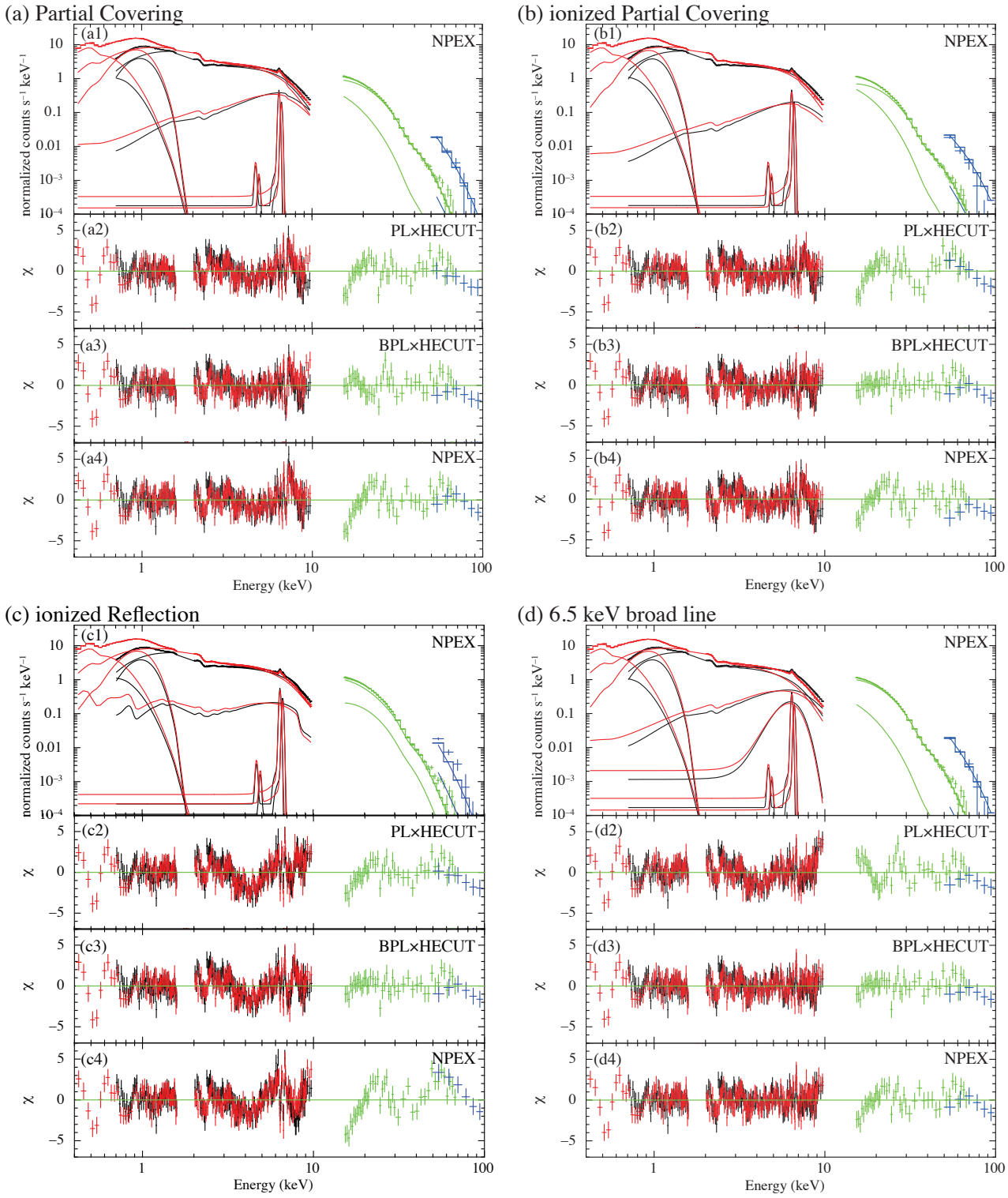

Figure 6.3: The same as Figure 6.2, but the partial covering model (a), the ionized partial covering model (b), ionized reflection model (c), and the 6.5 keV broad line (d) were added to the fitting model. Panel 1 of (a), (b), (c) and (d) used NPEX as the accretion-column emission model. Panel 2, 3, and 4 display the residuals from the fits with PL×HECUT, BPL×HECUT, and NPEX, respectively.

Table 6.1: Partial covering model fit parameters of Obs. 2.*

	Parameter	PL×HECUT	BPL×HECUT	NPEX
Accretion-column emission	$N_{\rm H}$†	≤ 0.8	≤ 0.8	≤ 0.8
	Γ_1‡	0.931 ± 0.008	$0.924^{+0.009}_{-0.008}$	0.57 ± 0.01
	Γ_2‡	–	1.32 ± 0.04	-2 (fixed)
	$E_{\rm break}$ (keV)	–	7.6 ± 0.1	–
	$E_{\rm cut}$ (keV)	$25.8^{+0.8}_{-0.6}$	$21.9^{+0.4}_{-0.3}$	5.7 ± 0.1
	$E_{\rm fold}$ (keV)	11 ± 1	$11.6^{+0.6}_{-0.5}$	–
	I_1§	0.110 ± 0.003	$0.120^{+0.005}_{-0.004}$	$0.132^{+0.005}_{-0.004}$
	I_2§	–	–	$(3.6 \pm 0.3) \times 10^{-4}$
	$N_{\rm H}$†	49 ± 3	66^{+6}_{-5}	42 ± 2
	f‖	$0.31^{+0.02}_{-0.01}$	$0.38^{+0.03}_{-0.02}$	0.38 ± 0.02
soft black body	$kT_{\rm BB}$ (keV)	0.087 ± 0.002	0.087 ± 0.003	0.085 ± 0.003
	$I_{\rm BB}$#	$(2.9 \pm 0.1) \times 10^{-3}$	$2.9^{+0.2}_{-0.1} \times 10^{-3}$	$3.2^{+0.2}_{-0.1} \times 10^{-3}$
broad 1 keV emission	$E_{\rm c}$ (keV)	0.87 ± 0.01	0.87 ± 0.01	0.85 ± 0.01
	σ (keV)	0.194 ± 0.006	0.196 ± 0.007	0.214 ± 0.007
	I**	$(3.2 \pm 0.2) \times 10^{-2}$	$3.3^{+0.3}_{-0.2} \times 10^{-2}$	$(4.1 \pm 0.3) \times 10^{-2}$
6.4 keV line	$E_{\rm c}$ (keV)	6.402 ± 0.008	6.40 ± 0.01	$6.406^{+0.006}_{-0.009}$
	I**	$9.0^{+0.5}_{-0.7} \times 10^{-4}$	$8.0^{+0.5}_{-0.8} \times 10^{-4}$	$8.7^{+0.5}_{-0.8} \times 10^{-4}$
6.7 keV line	$E_{\rm c}$	$6.63^{+0.01}_{-0.03}$	$6.60^{+0.02}_{-0.03}$	$6.63^{+0.01}_{-0.03}$
	I**	$(4.4 \pm 0.5) \times 10^{-4}$	$(3.5 \pm 0.6) \times 10^{-4}$	$(4.1 \pm 0.5) \times 10^{-4}$
CRSF‡‡	$E_{\rm cycl}$ (keV)	30 ± 1	$36.7^{+0.8}_{-0.7}$	35.6 ± 0.4
	$W_{\rm cycl}$ (keV)	19^{+3}_{-2}	6 ± 2	6 ± 1
	$D_{\rm cycl}$	1.0 ± 0.1	0.6 ± 0.1	0.78 ± 0.07
	$\chi^2_\nu(\nu)$	1.72 (461)	1.48 (459)	1.91 (461)

* All errors denote 90% error levels.
† Equivalent hydrogen column density in units of 10^{22} atoms cm^{-2}.
‡ Γ represents the photon index of the BPL and NPEX models. Γ_2 is fixed as -2 for NPEX.
§ Normalization in units of photons keV^{-1} cm^{-2} s^{-1} at 1 keV. Only NPEX has I_2, which corresponds to normalization of a positive PL.
‖ Covering Fraction.
Normalization in units of 10^{39} erg s^{-1}/(10 kpc)^2.
** Normalization in units of total photons cm^{-2} s^{-1} in the line.
†† $E_{\rm cycl}$, $W_{\rm cycl}$ and $D_{\rm cycl}$ are the fundamental cyclotron energy, width, and depth, respectively.

Table 6.2: The same as Table 6.1, but `zxipcf` was used instead of `pcfabs`.*

	Parameter	PL×HECUT	BPL×HECUT	NPEX
Accretion-column emission	$N_{\rm H}$†	≤ 0.001	≤ 0.8	≤ 0.8
	Γ_1‡	$0.919^{+0.009}_{-0.003}$	$0.929^{+0.008}_{-0.007}$	0.62 ± 0.01
	Γ_2‡	–	1.4 ± 0.1	-2
	$E_{\rm break}$ (keV)	–	7.7 ± 0.2	–
	$E_{\rm cut}$ (keV)	$25.2^{+0.4}_{-0.3}$	36^{+4}_{-2}	6.4 ± 0.2
	$E_{\rm fold}$ (keV)	$11.1^{+0.9}_{-0.5}$	8.3 ± 0.7	–
	I_1§	$0.119^{+0.002}_{-0.001}$	$0.14^{+0.02}_{-0.01}$	0.19 ± 0.01
	I_2§	–	–	$(2.2 \pm 0.2) \times 10^{-4}$
	$N_{\rm H}$†	65^{+2}_{-5}	85^{+14}_{-13}	42^{+3}_{-2}
	$\log(\xi)$	1.91 ± 0.02	$1.6^{+0.2}_{-0.1}$	$0.62^{+0.09}_{-0.08}$
	f‖	$0.37^{+0.02}_{-0.01}$	0.47 ± 0.05	0.56 ± 0.02
soft black body	$kT_{\rm BB}$ (keV)	0.087 ± 0.001	0.087 ± 0.003	$0.087^{+0.001}_{-0.003}$
	$I_{\rm BB}$#	$(2.9 \pm 0.1) \times 10^{-3}$	$2.9^{+0.2}_{-0.1} \times 10^{-3}$	$3.1^{+0.2}_{-0.1} \times 10^{-3}$
broad 1 keV emission	$E_{\rm c}$ (keV)	$0.872^{+0.009}_{-0.005}$	0.87 ± 0.01	0.86 ± 0.01
	σ (keV)	0.196 ± 0.005	0.194 ± 0.007	$0.204^{+0.008}_{-0.007}$
	I **	$(3.3 \pm 0.1) \times 10^{-2}$	$(3.2 \pm 0.2) \times 10^{-2}$	$(3.7 \pm 0.3) \times 10^{-2}$
6.4 keV line	$E_{\rm c}$ (keV)	$6.402^{+0.008}_{-0.005}$	6.40 ± 0.01	6.40 ± 0.01
	I **	$8.8^{+0.5}_{-0.6} \times 10^{-4}$	$8.2^{+0.5}_{-0.7} \times 10^{-4}$	$8.8^{+0.5}_{-0.8} \times 10^{-4}$
6.7 keV line	$E_{\rm c}$	$6.61^{+0.01}_{-0.02}$	$6.60^{+0.02}_{-0.03}$	$6.62^{+0.01}_{-0.03}$
	I**	$(4.1 \pm 0.5) \times 10^{-4}$	$(3.6 \pm 0.6) \times 10^{-4}$	$4.2^{+0.6}_{-0.5} \times 10^{-4}$
CRSF††	$E_{\rm cycl}$ (keV)	$24.1^{+0.1}_{-1.6}$	35 ± 1	36.7 ± 0.5
	$W_{\rm cycl}$ (keV)	24^{+2}_{-1}	$9.1^{+1.3}_{-0.8}$	9 ± 1
	$D_{\rm cycl}$	$0.71^{+0.04}_{-0.07}$	1.6 ± 0.2	$1.03^{+0.09}_{-0.06}$
	$\chi^2_\nu(\nu)$	1.61 (460)	1.35 (458)	1.64 (460)

* All errors denote 90% error levels.
† Γ represents the photon index of the BPL and NPEX models. Γ_2 is fixed as -2 for NPEX.
‡ Normalization in units of photons keV^{-1} cm^{-2} s^{-1} at 1 keV. Only NPEX has I_2, which corresponds to normalization of a positive PL.
§ Equivalent hydrogen column density in units of 10^{22} atoms cm^{-2}.
‖ Covering Fraction.
Normalization in units of 10^{39} erg s^{-1}/(10 kpc)^2.
** Normalization in units of total photons cm^{-2} s^{-1} in the line.
†† $E_{\rm cycl}$, $W_{\rm cycl}$ and $D_{\rm cycl}$ are the fundamental cyclotron energy, width, and depth, respectively.

velocity of 200 km/s illuminated by a PL emission with a photon index of 2.2. As shown in Figure 6.3 (b3), the ionized partial covering model with BPL×HECUT could represent the 4–9 keV hump better than the `pcfabs` model could (Figure 6.3 (a3)). In the case of PL×HECUT and NPEX, the residuals in 7–9 keV were not significantly improved with the `zxipcf` model (the second and forth panels of Figures 6.3 (a) and (b)). The ionized partial covering model with BPL×HECUT gave a reasonable value (< 1.4) of $\chi^2_\nu = 1.35$ (458). In the case of PL×HECUT and NPEX, the χ^2_ν was slightly worse (greater than 1.6).

6.3.2 Reflection on ionized matter

X-ray reflection on an accretion disk is observed in the several class of accreting compact objects (Rea et al., 2005; Cackett et al., 2010). The continuum spectrum is affected by photoelectric

Table 6.3: The same as Table 6.1, but `ireflect` was used instead of `pcfabs`.*

	Parameter	PL×HECUT	BPL×HECUT	NPEX
Accretion-column emission	Γ_1†	0.93 ± 0.01	$0.974^{+0.005}_{-0.010}$	0.58 ± 0.01
	Γ_2 †	–	$1.43^{+0.06}_{-0.04}$	-2 (fixed)
	$E_{\rm break}$ (keV)	–	$9.4^{+0.5}_{-0.3}$	–
	$E_{\rm cut}$ (keV)	27.3 ± 0.7	35^{+4}_{-3}	$5.12^{+0.05}_{-0.04}$
	$E_{\rm fold}$ (keV)	11 ± 1	9.1 ± 0.9	–
	I_1‡	$7.38^{+0.06}_{-0.07} \times 10^{-2}$	$7.61^{+0.05}_{-0.03} \times 10^{-2}$	$(8.27 \pm 0.09) \times 10^{-2}$
	I_2‡	–	–	$(4.2 \pm 0.2) \times 10^{-4}$
	$rel_{\rm ref}$	-3.7 ± 0.3	-5.5 ± 0.4	-2.0 ± 0.2
soft black body	$kT_{\rm BB}$ (keV)	0.084 ± 0.003	0.086 ± 0.003	0.086 ± 0.003
	$I_{\rm BB}$#	$(3.0 \pm 0.2) \times 10^{-3}$	$2.91^{+0.09}_{-0.14} \times 10^{-3}$	$3.1 \pm 0.2 \times 10^{-3}$
broad 1 keV emission	$E_{\rm c}$ (keV)	0.86 ± 0.01	0.873765 ± 0.01	$0.85^{+0.01}_{-0.02}$
	σ (keV)	$0.206^{+0.008}_{-0.007}$	0.194 ± 0.007	$0.214^{+0.009}_{-0.008}$
	I **	$(3.6 \pm 0.3) \times 10^{-2}$	$(3.2 \pm 0.2) \times 10^{-2}$	$(4.0 \pm 0.3) \times 10^{-2}$
CRSF††	$E_{\rm cycl}$ (keV)	29 ± 1	$35.4^{+1.3}_{-1.1}$	35.1 ± 0.5
	$W_{\rm cycl}$ (keV)	18 ± 2	$8.6^{+1.0}_{-0.8}$	$2.2^{+0.8}_{-0.7}$
	$D_{\rm cycl}$	1.0 ± 0.1	1.6 ± 0.3	$0.6^{+0.2}_{-0.1}$
	$\chi^2_\nu(\nu)$	2.19 (468)	1.81 (466)	2.48 (468)

* All errors denote 90% error levels.
† Γ represents the photon index of the BPL and NPEX models. Γ_2 is fixed as -2 for NPEX.
‡ Normalization in units of photons keV^{-1} cm^{-2} s^{-1} at 1 keV. Only NPEX has I_2, which corresponds to normalization of a positive PL.
§ Equivalent hydrogen column density in units of 10^{22} atoms cm^{-2}.
‖ Covering Fraction.
Normalization in units of 10^{39} erg s^{-1}/(10 kpc)^2.
** Normalization in units of total photons cm^{-2} s^{-1} in the line.
†† $E_{\rm cycl}$, $W_{\rm cycl}$ and $D_{\rm cycl}$ are the fundamental cyclotron energy, width, and depth, respectively.

absorption forming a hump structure just below the energy of Fe K-edge. We fitted the broad-band spectrum with the ionized reflection model `ireflect` (Magdziarz and Zdziarski, 1995) in XSPEC. In the fitting, we used three empirical column emission models multiplied by `ireflect`, and fixed the disk temperature to 3×10^4 K, and the abundance to the solar one.

The fitting result is shown in Figure 6.3 (c) and the best-fit parameters are shown in Table 6.3. The reflection scale factor in the `ireflect` model is defined as $rel_{\rm ref} \equiv \Omega/2\pi$, where Ω is a solid angle of the reflector seen from the light source. The best-fit parameter of $rel_{\rm ref}$ is 2.0 $\pm$ 0.2, requiring the large ($> 2\pi$) solid angle of the reflection matter which requires unphysical condition in the Her X-1 binary system. In addition, since the χ^2_ν value was large (> 1.8), we conclude that the reflection model is not favored to describe the 4-9 keV hump.

6.3.3 Additional Broad Line around 6.5 keV

As shown in Figure 6.1 and the third panels of Figures 6.2 (a3), (b3), and (c3), the 4–9 keV hump seems to be a Gaussian-like symmetric structure about 6.5 keV. We considered adding a line component to represent the 4–9 keV hump. We fitted the Obs. 2 data with a model consisting of the soft excess, the continuum with three accretion-column emission models, narrow Fe lines at 6.4 and 6.7 keV (these were introduced in section 6.2), and the broad line around 6.5 keV

with width ∼1 keV.

Figure 6.3 (d1) shows the fitting model with NPEX and the Obs. 2 data. As shown in Figure 6.3 (d2), in the case of PL×HECUT, the residuals remained over the 0.4–100 keV band. On the other hand, BPL×HECUT and NPEX with the additional broad-line models could generally represent the whole spectrum (Figures 6.3 (d3) and (d4)). The reduced chi-square was 1.86 (460) for PL×HECUT, 1.28 (458) for BPL×HECUT, and 1.36 (460) for NPEX. Thus, both the BPL×HECUT and NPEX models with the 6.5 keV broad line gave reasonable values of χ^2_ν. Table 6.4 summarizes the fitting parameters for each accretion-column emission model. The additional line has center energy at ∼6.5 keV and width σ ∼1 keV, so we call this component the "6.5 keV broad line".

The fitting quality of the BPL×HECUT or NPEX continuum model combined with the 6.5 keV broad-line emission were statistically comparable to that of the BPL×HECUT continuum model with the partial covering, so we used the three models to represent the broad-band spectra in the following sections.

Table 6.4: Accretion-column emission with the 6.5 keV broad line model fit parameters of Obs. 2.*

	Parameter	PL×HECUT	BPL×HECUT	NPEX
Accretion-column emission	$N_{\rm H}$†	≤ 0.8	≤ 0.8	≤ 0.8
	Γ_1‡	0.878 ± 0.004	$0.920^{+0.008}_{-0.007}$	0.62 ± 0.01
	Γ_2‡	–	0.74 ± 0.01	-2
	$E_{\rm break}$ (keV)	–	4.2 ± 0.1	–
	$E_{\rm cut}$ (keV)	$20.7^{+0.2}_{-0.1}$	39^{+3}_{-5}	5.8 ± 0.1
	$E_{\rm fold}$ (keV)	10.3 ± 0.4	7.1 ± 0.5	–
	I_1 §	$(7.16 \pm 0.04) \times 10^{-2}$	$7.48^{+0.06}_{-0.05} \times 10^{-2}$	$(8.37 \pm 0.09) \times 10^{-2}$
	I_2 §	–	–	$(3.6 \pm 0.2) \times 10^{-4}$
soft black body	$kT_{\rm BB}$ (keV)	0.083 ± 0.003	0.087 ± 0.002	0.086 ± 0.003
	$I_{\rm BB}$ ‖	$(3.1 \pm 0.2) \times 10^{-3}$	$(2.9 \pm 0.1) \times 10^{-3}$	$3.1^{+0.2}_{-0.1} \times 10^{-3}$
broad 1 keV emission	$E_{\rm c}$ (keV)	0.85 ± 0.01	0.87 ± 0.01	0.86 ± 0.01
	σ (keV)	0.217 ± 0.007	$0.196^{+0.006}_{-0.005}$	0.208 ± 0.007
	I #	$4.0^{+0.3}_{-0.2} \times 10^{-2}$	$3.3 \pm 0.2 \times 10^{-2}$	$(3.8 \pm 0.3) \times 10^{-2}$
6.4 keV line	$E_{\rm c}$ (keV)	6.404 ± 0.008	$6.407^{+0.009}_{-0.004}$	$6.407^{+0.009}_{-0.008}$
	I#	$8.4^{+0.5}_{-0.8} \times 10^{-4}$	$(7.9 \pm 0.5) \times 10^{-4}$	$8.2^{+0.6}_{-0.7} \times 10^{-4}$
6.7 keV line	$E_{\rm c}$	$6.63^{+0.01}_{-0.02}$	$6.62^{+0.02}_{-0.03}$	$6.63^{+0.02}_{-0.03}$
	I #	$3.9^{+0.6}_{-0.5} \times 10^{-4}$	$(3.6 \pm 0.6) \times 10^{-4}$	$3.8^{+0.5}_{-0.6} \times 10^{-4}$
6.5 keV broad line	$E_{\rm c}$	$6.73^{+0.05}_{-0.06}$	$6.48^{+0.05}_{-0.03}$	6.46 ± 0.05
	σ (keV)	$0.96^{+0.07}_{-0.08}$	$0.72^{+0.07}_{-0.08}$	$1.01^{+0.07}_{-0.08}$
	I #	$(4.6 \pm 0.3) \times 10^{-3}$	$(3.0 \pm 0.3) \times 10^{-3}$	$(5.7 \pm 0.5) \times 10^{-3}$
CRSF**	$E_{\rm cycl}$ (keV)	36.9 ± 0.6	$35.5^{+0.8}_{-2.5}$	35.6 ± 0.4
	$W_{\rm cycl}$ (keV)	5 ± 1	12^{+1}_{-2}	8 ± 1
	$D_{\rm cycl}$	0.60 ± 0.08	$2.2^{+0.2}_{-0.5}$	0.85 ± 0.07
	$\chi^2_\nu(\nu)$	1.86 (460)	1.28 (458)	1.36 (460)

* All errors denote 90% error levels.
† Equivalent hydrogen column density in units of 10^{22} atoms cm^{-2}.
‡ Γ represents the photon index of the BPL and NPEX models. Γ_2 is fixed as -2 for NPEX.
§ Normalization in units of photons keV^{-1} cm^{-2} s^{-1} at 1 keV. Only NPEX has I_2, which corresponds to normalization of a positive PL.
‖ Normalization in units of 10^{39} erg s^{-1}/(10 kpc)^2.
Normalization in units of total photons cm^{-2} s^{-1} in the line.
** $E_{\rm cycl}$, $W_{\rm cycl}$ and $D_{\rm cycl}$ are the fundamental cyclotron energy, width, and depth, respectively.

6.4 Spectral Fit of Suzaku Observations

We fitted the models introduced in section 6.3.3 to the data of Obs. 4, 5, and 6. The best-fit parameters and 90% confidence errors for the BPL×HECUT with the ionized partial covering model and the NPEX with the 6.5 keV broad-line model are summarized in Tables 6.5 and 6.7, respectively. The fitting results using NPEX with the 6.5 keV broad-line model are shown in Figure 6.7. The BPL×HECUT with the ionized partial covering model and the NPEX with the 6.5 keV broad-line model result in a similar quality of fit for all four observations. There were also no significant differences in the parameter values between the two models, except for CRSF parameters. For the 6.5 keV broad line model, the choice of the continuum has some influence on the 6.5 keV broad-line parameters as shown in Figures 6.8 and 6.9.

In all the observations, there were both 6.4 and 6.7 keV Fe lines, even during the main-on phase. This double-peak line feature in the main-on phase has been detected in only our study and the ASCA observations (Endo et al., 2000). In addition to the double-peak Fe lines, the 4–9 keV hump was found constantly, indicating the partial covering or the 6.5 keV broad line were required around Fe K line energy in all observations.

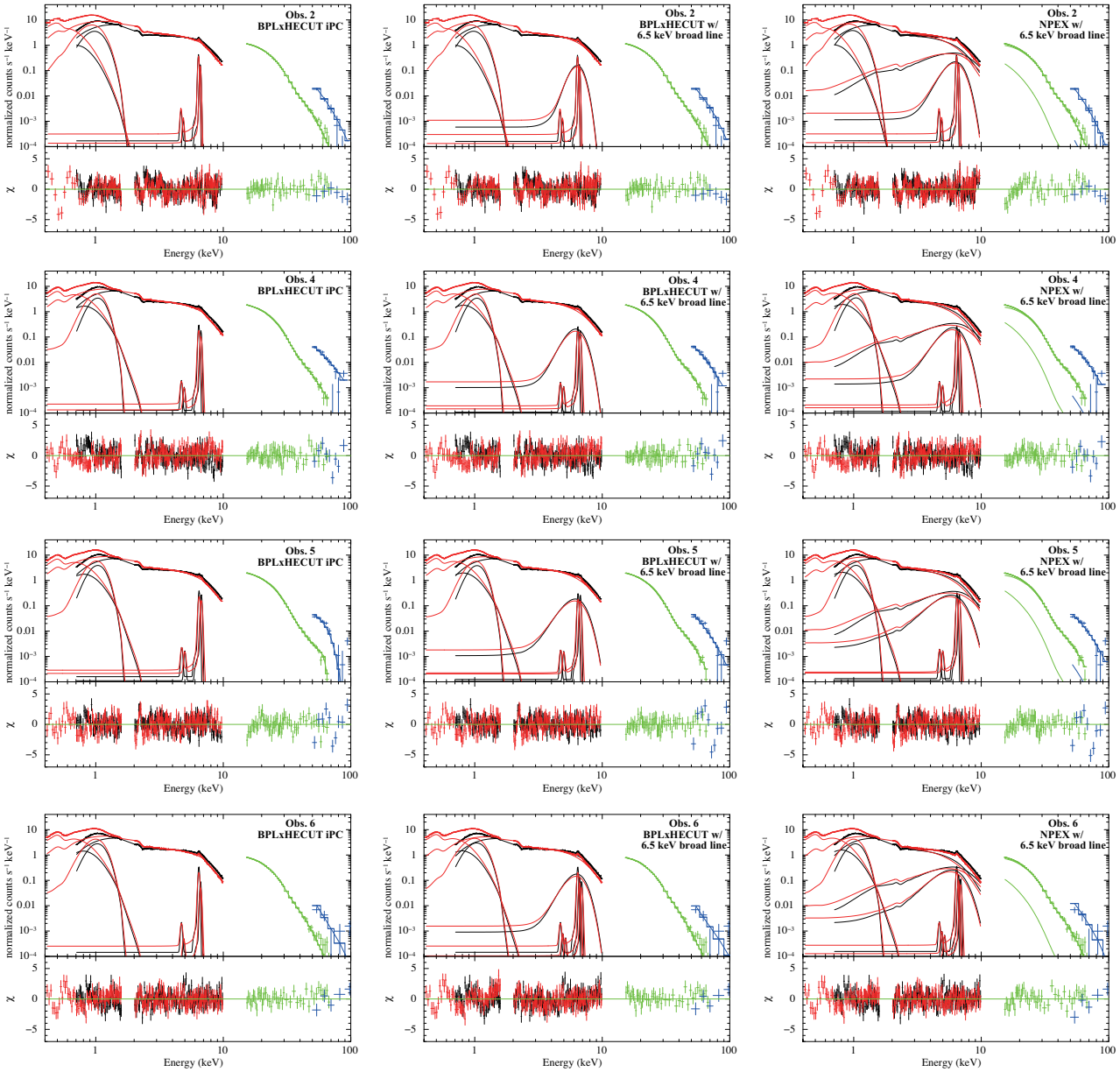

Figure 6.4: Her X-1 spectra from Obs. 2, 4, 5 and 6 with the BPL×HECUT with the ionized partial covering model (left), the BPL×HECUT with the 6.5 keV broad line model (middle) and the NPEX with the 6.5 keV broad line model (right).

Table 6.5: BPL×HECUT with ionized partial covering model fit parameters of Obs. 2, 4, 5 and 6.*

	Parameter	Obs. 2	Obs. 4	Obs. 5	Obs. 6
BPL×HECUT	$N_{\rm H}$†	≤ 0.8	≤ 0.8	≤ 0.8	≤ 0.8
	Γ_1‡	$0.929^{+0.008}_{-0.007}$	$1.01^{+0.02}_{-0.01}$	1.02 ± 0.01	1.02 ± 0.02
	Γ_2‡	1.4 ± 0.1	-0.5 ± 0.5	$2.9^{+0.4}_{-0.3}$	1.9 ± 0.2
	$E_{\rm break}$ (keV)	7.7 ± 0.2	$16.9^{+0.6}_{-0.7}$	$25.0^{+0.7}_{-0.5}$	$7.9^{+0.2}_{-0.3}$
	$E_{\rm cut}$ (keV)	36^{+4}_{-2}	$28.2^{+1.1}_{-0.9}$	62^{+2}_{-4}	28^{+10}_{-3}
	$E_{\rm fold}$ (keV)	8.3 ± 0.7	9 ± 1	$0.9^{+2.8}_{-0.9}$	10 ± 3
	I_1§	$0.14^{+0.02}_{-0.01}$	$0.32^{+0.05}_{-0.06}$	$0.23^{+0.02}_{-0.01}$	$0.18^{+0.04}_{-0.03}$
	$N_{\rm H}$†	85^{+14}_{-13}	113^{+8}_{-11}	65^{+14}_{-5}	116^{+16}_{-20}
	$\log(\xi)$	$1.6^{+0.2}_{-0.1}$	$2.07^{+0.04}_{-0.06}$	$2.25^{+0.07}_{-0.06}$	2.00 ± 0.05
	CF‖	0.47 ± 0.05	$0.53^{+0.08}_{-0.12}$	$0.26^{+0.03}_{-0.02}$	$0.66^{+0.06}_{-0.07}$
soft black body	$kT_{\rm BB}$ (keV)	0.087 ± 0.003	$0.112^{+0.002}_{-0.003}$	0.111 ± 0.002	0.108 ± 0.003
	$I_{\rm BB}$#	$2.9^{+0.2}_{-0.1} \times 10^{-3}$	$5.0^{+0.4}_{-0.1} \times 10^{-3}$	$(5.7 \pm 0.1) \times 10^{-3}$	$2.95^{+0.09}_{-0.08} \times 10^{-3}$
broad 1 keV emission	$E_{\rm c}$ (keV)	0.87 ± 0.01	0.977 ± 0.008	$0.976^{+0.006}_{-0.007}$	0.95 ± 0.01
	σ (keV)	0.194 ± 0.007	0.150 ± 0.006	0.152 ± 0.005	$0.169^{+0.009}_{-0.008}$
	I**	$(3.2 \pm 0.2) \times 10^{-2}$	$(4.1 \pm 0.3) \times 10^{-2}$	$(4.9 \pm 0.3) \times 10^{-2}$	$(2.3 \pm 0.2) \times 10^{-2}$
	EW (eV)	340 ± 20	210^{+20}_{-10}	230^{+200}_{-20}	260^{+30}_{-20}
6.4 keV line	$E_{\rm c}$ (keV)	6.40 ± 0.01	6.43 ± 0.02	$6.46^{+0.02}_{-0.01}$	6.44 ± 0.01
	I**	$8.2^{+0.5}_{-0.7} \times 10^{-4}$	$(1.2 \pm 0.2) \times 10^{-3}$	$1.5 \pm 0.2 \times 10^{-3}$	$(8 \pm 1) \times 10^{-4}$
	EW (eV)	50 ± 3	42^{+8}_{-4}	49^{+60}_{-5}	61^{+10}_{-7}
6.7 keV line	$E_{\rm c}$	$6.60^{+0.02}_{-0.03}$	6.69 ± 0.04	6.74 ± 0.02	$6.64^{+0.05}_{-0.03}$
	I**	$(3.6 \pm 0.6) \times 10^{-4}$	$8 \pm 2 \times 10^{-4}$	$(1.2 \pm 0.2) \times 10^{-3}$	$(2.1 \pm 0.9) \times 10^{-4}$
	EW (eV)	21 ± 3	26 ± 7	39^{+30}_{-4}	16^{+8}_{-6}
CRSF††	$E_{\rm cycl}$ (keV)	35 ± 1	28 ± 2	36^{+1}_{-2}	30 ± 2
	$W_{\rm cycl}$ (keV)	$9.1^{+0.8}_{-1.3}$	18 ± 2	19 ± 1	8^{+5}_{-2}
	$D_{\rm cycl}$	1.6 ± 0.2	1.9 ± 0.3	$1.4^{+0.1}_{-0.2}$	$0.7^{+0.8}_{-0.2}$
	$\chi^2_\nu(\nu)$	1.39 (458)	1.38 (475)	1.38 (468)	1.20 (458)

* All errors denote 90% error levels.
† Γ represents the photon index of the BPL model.
‡ Normalization in units of photons keV^{-1} cm^{-2} s^{-1} at 1 keV.
§ Equivalent hydrogen column density in units of 10^{22} atoms cm^{-2}.
‖ Covering Fraction.
Normalization in units of 10^{39} erg s^{-1}/(10 kpc)^2.
** Normalization in units of total photons cm^{-2} s^{-1} in the line.
†† $E_{\rm cycl}$, $W_{\rm cycl}$ and $D_{\rm cycl}$ are the fundamental cyclotron energy, width, and depth, respectively.

Table 6.6: BPL×HECUT with the 6.5 keV broad line model fit parameters of Obs. 2, 4, 5 and 6.*

	Parameter	Obs. 2	Obs. 4	Obs. 5	Obs. 6
BPL×HECUT	$N_{\rm H}$	≤ 0.8	≤ 0.8	≤ 0.8	≤ 0.8
	Γ_1 †	$0.920^{+0.008}_{-0.007}$	0.99 ± 0.01	0.99 ± 0.01	0.918 ± 0.006
	Γ_2 †	0.74 ± 0.01	0.68 ± 0.04	0.73 ± 0.05	2.8 ± 0.4
	$E_{\rm break}$ (keV)	4.2 ± 0.1	7.6 ± 0.4	$8.2^{+0.8}_{-0.9}$	$19.5^{+0.5}_{-0.6}$
	$E_{\rm cut}$ (keV)	39^{+3}_{-5}	35 ± 2	34^{+3}_{-1}	25^{+2}_{-1}
	$E_{\rm fold}$ (keV)	7.1 ± 0.5	8.3 ± 0.5	8.0 ± 0.4	15^{+3}_{-2}
	I_1 ‡	$7.48^{+0.06}_{-0.05} \times 10^{-2}$	$(14.8 \pm 0.2) \times 10^{-2}$	$(16.4 \pm 0.2) \times 10^{-2}$	$5.79^{+0.06}_{-0.05} \times 10^{-2}$
soft black body	$kT_{\rm BB}$ (keV)	0.087 ± 0.002	$0.114^{+0.002}_{-0.003}$	0.113 ± 0.002	0.107 ± 0.003
	$I_{\rm BB}$ §	$(2.9 \pm 0.1) \times 10^{-3}$	$(5.2 \pm 0.1) \times 10^{-3}$	$5.9^{+0.2}_{-0.1} \times 10^{-3}$	$3.13^{+0.09}_{-0.08} \times 10^{-3}$
broad 1 keV emission	$E_{\rm c}$ (keV)	0.87 ± 0.01	0.982 ± 0.008	$0.982^{+0.007}_{-0.008}$	0.93 ± 0.02
	σ (keV)	$0.196^{+0.006}_{-0.005}$	$0.149^{+0.007}_{-0.006}$	$0.151^{+0.003}_{-0.006}$	0.19 ± 0.01
	I ‖	$3.3 \pm 0.2 \times 10^{-2}$	$(4.0 \pm 0.3) \times 10^{-2}$	$(4.7 \pm 0.3) \times 10^{-2}$	$(2.9 \pm 0.3) \times 10^{-2}$
	EW (eV)	340 ± 20	206^{+20}_{-14}	217^{+12}_{-14}	330 ± 30
6.4 keV line	$E_{\rm c}$ (keV)	$6.407^{+0.009}_{-0.004}$	6.44 ± 0.02	$6.46^{+0.02}_{-0.01}$	6.43 ± 0.01
	I ‖	$(7.9 \pm 0.5) \times 10^{-4}$	$(1.0 \pm 0.2) \times 10^{-3}$	$(1.2 \pm 0.2) \times 10^{-3}$	$(7.9 \pm 0.9) \times 10^{-4}$
	EW (eV)	48^{+4}_{-3}	35^{+7}_{-5}	38^{+6}_{-5}	61^{+9}_{-8}
6.7 keV line	$E_{\rm c}$	$6.62^{+0.02}_{-0.03}$	6.72 ± 0.03	6.74 ± 0.02	6.64 ± 0.03
	I ‖	$(3.6 \pm 0.6) \times 10^{-4}$	$(8 \pm 2) \times 10^{-4}$	$(1.1 \pm 0.2) \times 10^{-3}$	$3.4^{+0.8}_{-1.0} \times 10^{-4}$
	EW (eV)	21^{+4}_{-3}	29^{+8}_{-7}	37 ± 5	25^{+7}_{-8}
6.93 keV line	$E_{\rm c}$ (keV)	–	–	–	6.89 ± 0.04
	I ‖	–	–	–	$2.5^{+0.8}_{-0.9} \times 10^{-4}$
	EW (eV)	–	–	–	20 ± 7
6.5 keV broad line	$E_{\rm c}$	$6.48^{+0.05}_{-0.03}$	$6.42^{+0.07}_{-0.08}$	$6.41^{+0.09}_{-0.07}$	6.54 ± 0.07
	σ (keV)	$0.72^{+0.07}_{-0.08}$	1.0 ± 0.1	1.1 ± 0.2	$1.03^{+0.09}_{-0.08}$
	I ‖	$(3.0 \pm 0.3) \times 10^{-3}$	$(9 \pm 1) \times 10^{-3}$	$10^{+3}_{-2} \times 10^{-3}$	$(5.1 \pm 0.4) \times 10^{-3}$
	EW (eV)	180 ± 20	350^{+70}_{-40}	350^{+60}_{-70}	430 ± 40
CRSF#	$E_{\rm cycl}$ (keV)	$35.5^{+0.8}_{-2.5}$	$34.2^{+0.9}_{-0.8}$	$33.8^{+1.2}_{-0.7}$	33 ± 1
	$W_{\rm cycl}$ (keV)	12^{+1}_{-2}	$11.0^{+0.8}_{-0.7}$	$10.4^{+0.7}_{-0.6}$	≤ 4
	$D_{\rm cycl}$	$2.2^{+0.2}_{-0.5}$	2.0 ± 0.2	$1.9^{+0.3}_{-0.2}$	0.4 ± 0.2
	$\chi^2_\nu(\nu)$	1.28 (458)	1.31 (475)	1.31 (468)	1.43(456)

* Γ represents a photon index of BPL.
† Normalization in units of photons keV^{-1} cm^{-2} s^{-1} at 1 keV.
‡ Normalization in units of 10^{39} erg s^{-1}/(10 kpc)^2.
§ Normalization in units of total photons cm^{-2} s^{-1} in the line.
‖ $E_{\rm cycl}$, $W_{\rm cycl}$ and $D_{\rm cycl}$ are a fundamental cyclotron energy, width and depth, respectively.

Table 6.7: NPEX with the 6.5 keV broad line model fit parameters of the Obs. 2, 4, 5 and 6.*

	Parameter	Obs. 2	Obs. 4	Obs. 5	Obs. 6
NPEX	$N_{\rm H}$†	≤ 0.8	≤ 0.8	≤ 0.8	≤ 0.8
	Γ_1‡	0.62 ± 0.01	0.71 ± 0.02	0.73 ± 0.03	0.75 ± 0.04
	$E_{\rm cut}$ (keV)	5.8 ± 0.1	6.6 ± 0.2	6.5 ± 0.2	$5.8^{+0.6}_{-0.3}$
	Flux§	$4.81^{+0.02}_{-0.03}$	$8.18^{+0.03}_{-0.06}$	$8.79^{+0.01}_{-0.09}$	$3.50^{+0.01}_{-0.06}$
soft black body	$kT_{\rm BB}$ (keV)	0.086 ± 0.01	$0.115^{+0.002}_{-0.003}$	$0.114^{+0.003}_{-0.002}$	0.110 ± 0.003
	$I_{\rm BB}$‖	$3.1^{+0.2}_{-0.1} \times 10^{-3}$	$(5.5 \pm 0.1) \times 10^{-3}$	$6.2^{+0.3}_{-0.1} \times 10^{-3}$	$3.09^{+0.08}_{-0.07} \times 10^{-3}$
broad 1 keV emission	$E_{\rm c}$ (keV)	0.86 ± 0.003	$0.980^{+0.008}_{-0.009}$	$0.981^{+0.007}_{-0.006}$	0.95 ± 0.01
	σ (keV)	0.208 ± 0.007	0.153 ± 0.007	0.153 ± 0.006	0.168 ± 0.009
	I#	$3.8 \pm 0.3 \times 10^{-2}$	$(4.3 \pm 0.3) \times 10^{-2}$	$4.9^{+0.4}_{-0.3} \times 10^{-2}$	$2.3^{+0.3}_{-0.2} \times 10^{-2}$
	EW (eV)	390 ± 20	220^{+20}_{-10}	230^{+10}_{-20}	260 ± 30
6.4 keV line	$E_{\rm c}$ (keV)	$6.407^{+0.009}_{-0.008}$	6.44 ± 0.02	$6.46^{+0.02}_{-0.01}$	6.43 ± 0.01
	I #	$8.2^{+0.6}_{-0.7} \times 10^{-4}$	$(1.1 \pm 0.2) \times 10^{-3}$	$1.3^{+0.3}_{-0.2} \times 10^{-3}$	$(8.6 \pm 0.9) \times 10^{-4}$
	EW (eV)	50 ± 4	38 ± 6	41 ± 6	66^{+7}_{-8}
6.7 keV line	$E_{\rm c}$	$6.63^{+0.02}_{-0.03}$	6.72 ± 0.03	6.74 ± 0.02	6.64 ± 0.03
	I #	$3.8^{+0.5}_{-0.6} \times 10^{-4}$	$(9 \pm 2) \times 10^{-4}$	$(1.2 \pm 0.2) \times 10^{-3}$	$(4 \pm 1) \times 10^{-4}$
	EW (eV)	23^{+4}_{-3}	32^{+5}_{-7}	41^{+6}_{-7}	30^{+6}_{-8}
6.93 keV line	$E_{\rm c}$	–	–	–	$6.90^{+0.03}_{-0.04}$
	I #	–	–	–	$(3.2 \pm 0.8) \times 10^{-4}$
	EW (eV)	–	–	–	26^{+8}_{-5}
6.5 keV broad line	$E_{\rm c}$	6.46 ± 0.05	$6.24^{+0.08}_{-0.09}$	$6.11^{+0.09}_{-0.17}$	6.2 ± 0.1
	σ	$1.01\ ^{+0.07}_{-0.08}$	1.1 ± 0.1	$1.5^{+0.3}_{-0.2}$	1.5 ± 0.2
	I #	$(5.7 \pm 0.5) \times 10^{-3}$	$(1.2 \pm 0.2) \times 10^{-2}$	$1.7^{+0.6}_{-0.3} \times 10^{-2}$	$1.0^{+0.3}_{-0.2} \times 10^{-2}$
	EW (eV)	370^{+30}_{-40}	460^{+70}_{-50}	700 ± 100	900^{+200}_{-100}
CRSF **	$E_{\rm cycl}$ (keV)	35.6 ± 0.4	36.1 ± 0.3	36.2 ± 0.3	$34.4^{+0.7}_{-0.6}$
	$W_{\rm cycl}$ (keV)	8 ± 1	11 ± 1	$10.4^{+0.7}_{-0.8}$	10^{+5}_{-3}
	$D_{\rm cycl}$	0.85 ± 0.07	1.3 ± 0.1	1.28 ± 0.05	$0.9^{+0.3}_{-0.2}$
	$\chi^2_\nu(\nu)$	1.36 (460)	1.35 (477)	1.37 (470)	1.27 (458)

* All errors denote 90% error levels.
† Γ is a photon index of a negative PL. A positive PL photon index is fixed as -2.
‡ The 0.01–100 keV flux in units of erg s^{-1} cm^{-2}.
§ Normalization in units of 10^{39} erg s^{-1}/(10 kpc)^2.
‖ Normalization in units of total photons cm^{-2} s^{-1} in the line.
$E_{\rm cycl}$, $W_{\rm cycl}$ and $D_{\rm cycl}$ are a fundamental cyclotron energy, width and depth, respectively.

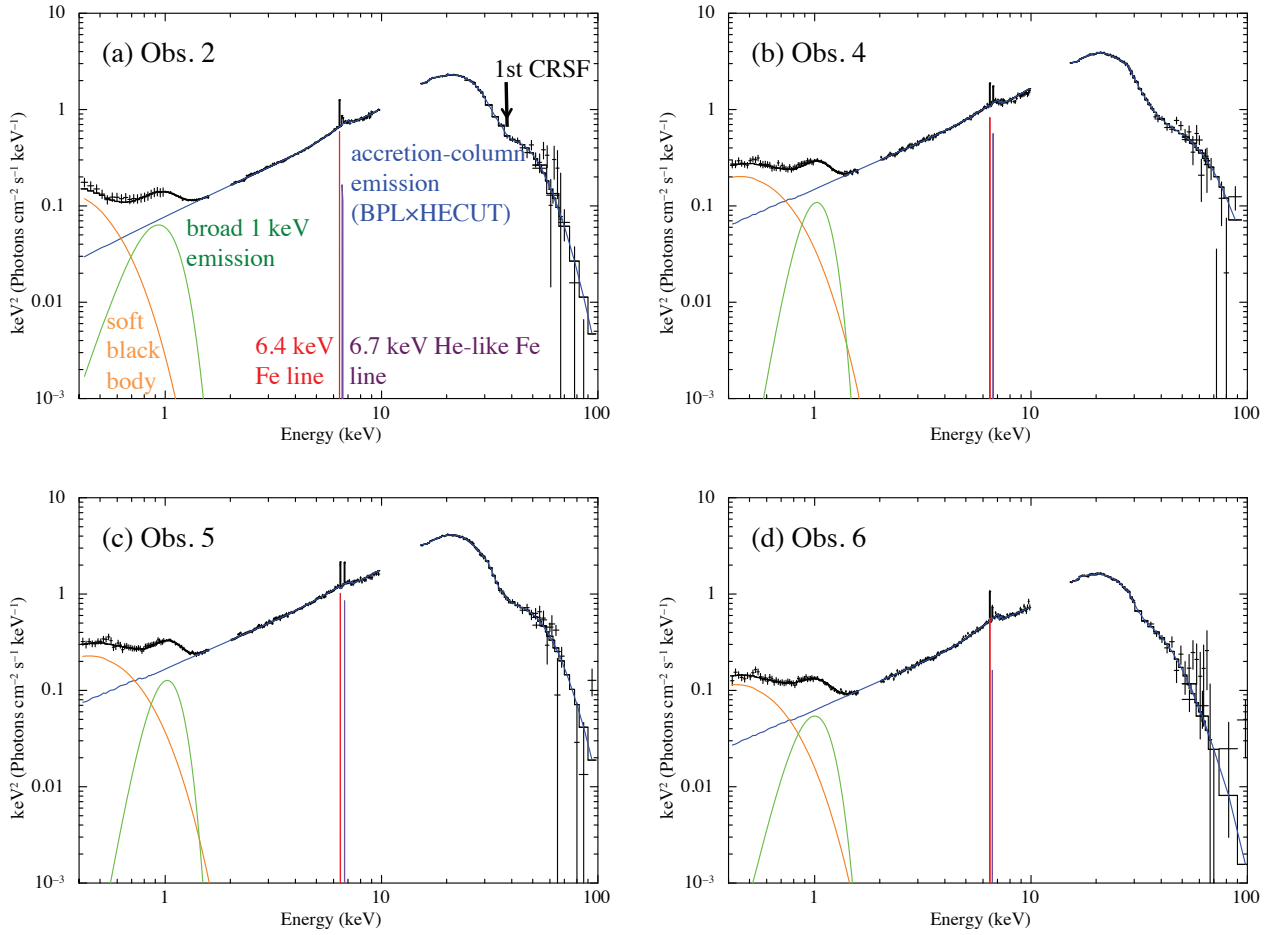

Figure 6.5: Her X-1 spectra from Obs. 2, 4, 5, and 6, shown in the νF_ν form after removing detector responses. The XIS data refer to XIS0, except in Obs. 2, in which XIS0+2+3 is used. The fitting model is BPL×HECUT with the ionized partial covering model. The accretion-column emission (blue), soft black body (orange), broad 1 keV emission (green), 6.4 keV Fe line (red), 6.7 keV He-like Fe line (purple), and 6.5 keV broad line (magenta) are shown as different colors.

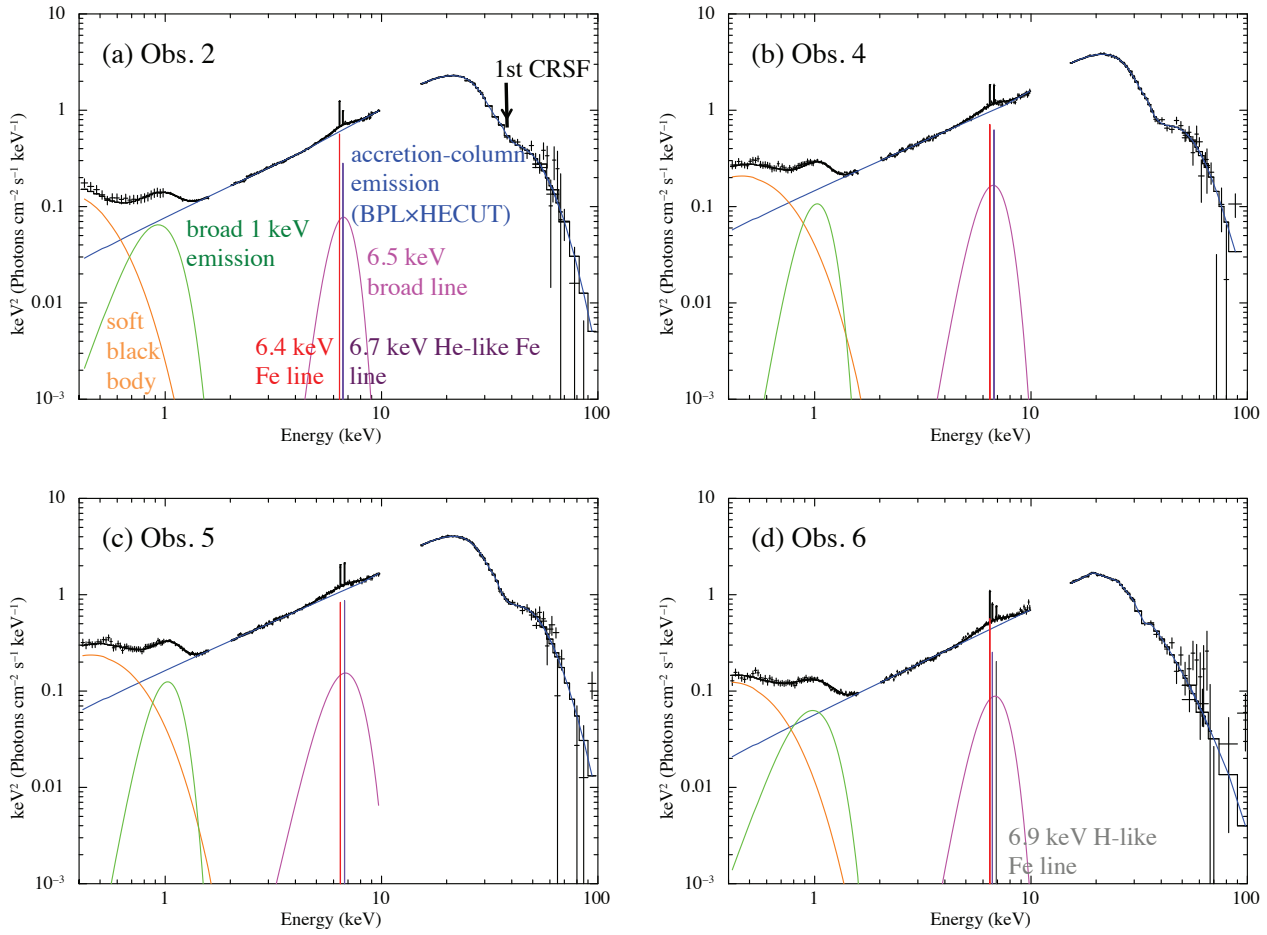

Figure 6.6: The same as Figure 6.5, but the BPL×HECUT with the 6.5 keV broad line model is used. The 6.5 keV broad line is shown in magenta. The 6.9 keV Fe line is indicated by gray and present in Obs. 6 only.

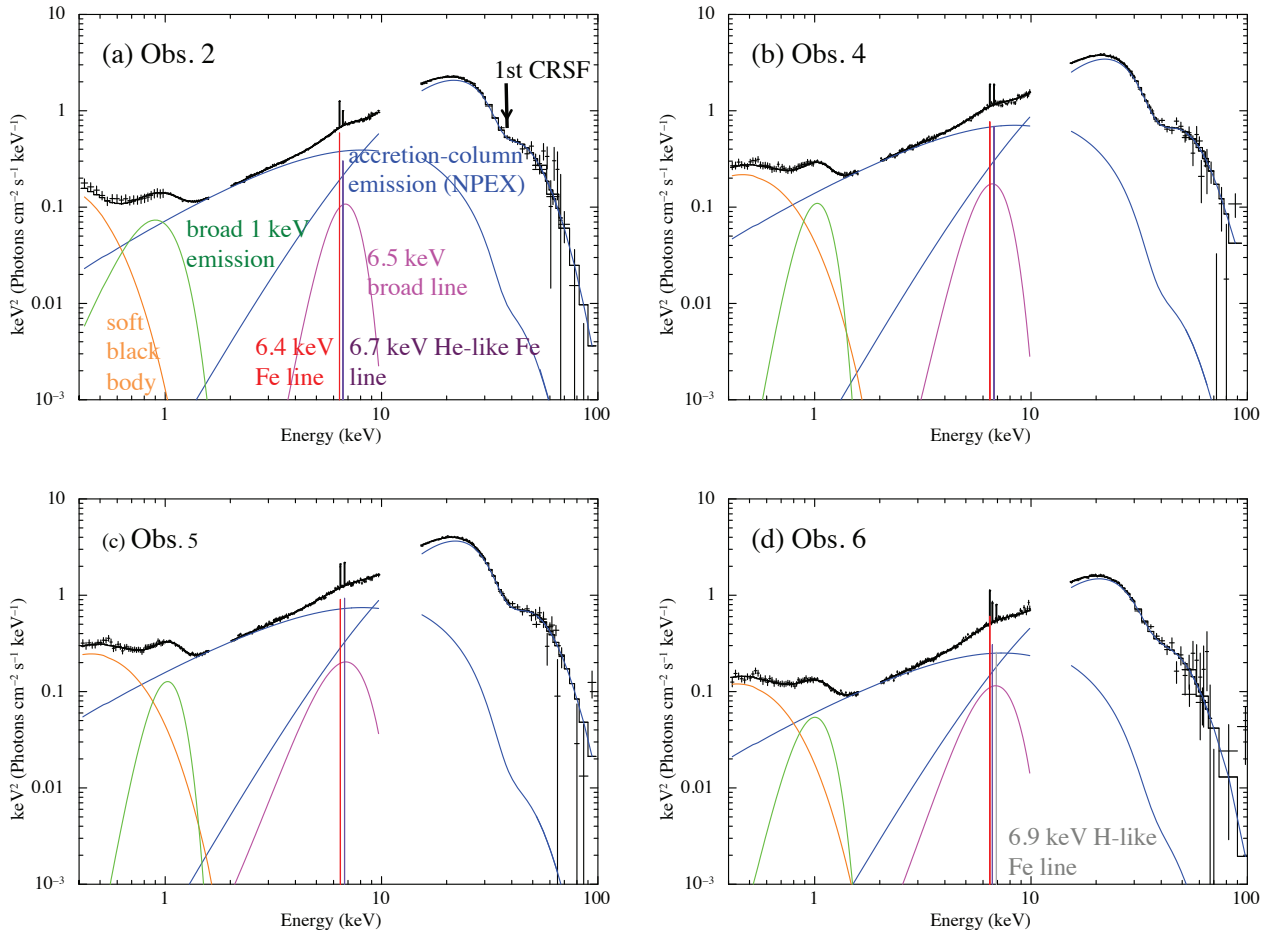

Figure 6.7: The same as Figure , but the NPEX model is used as the accretion-column emission.

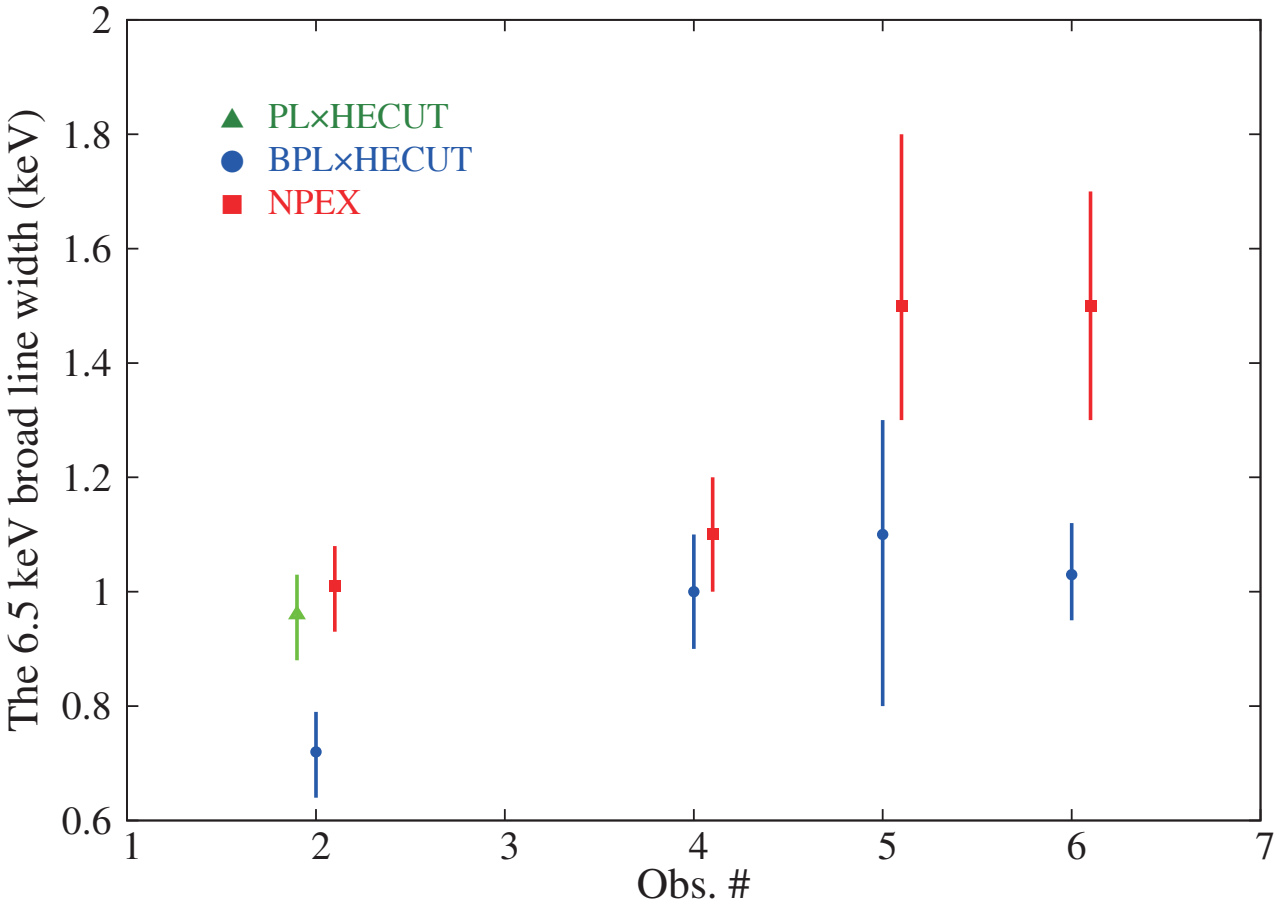

Figure 6.8: The 6.5 keV broad line width in Obs. 2, 4, 5 and 6 for the two accretion-continuum models, BPL×HECUT (circle) and NPEX (square). Only in Obs. 2, the case of the PL×HECUT with the 6.5 keV broad line model is also indicated by triangle.

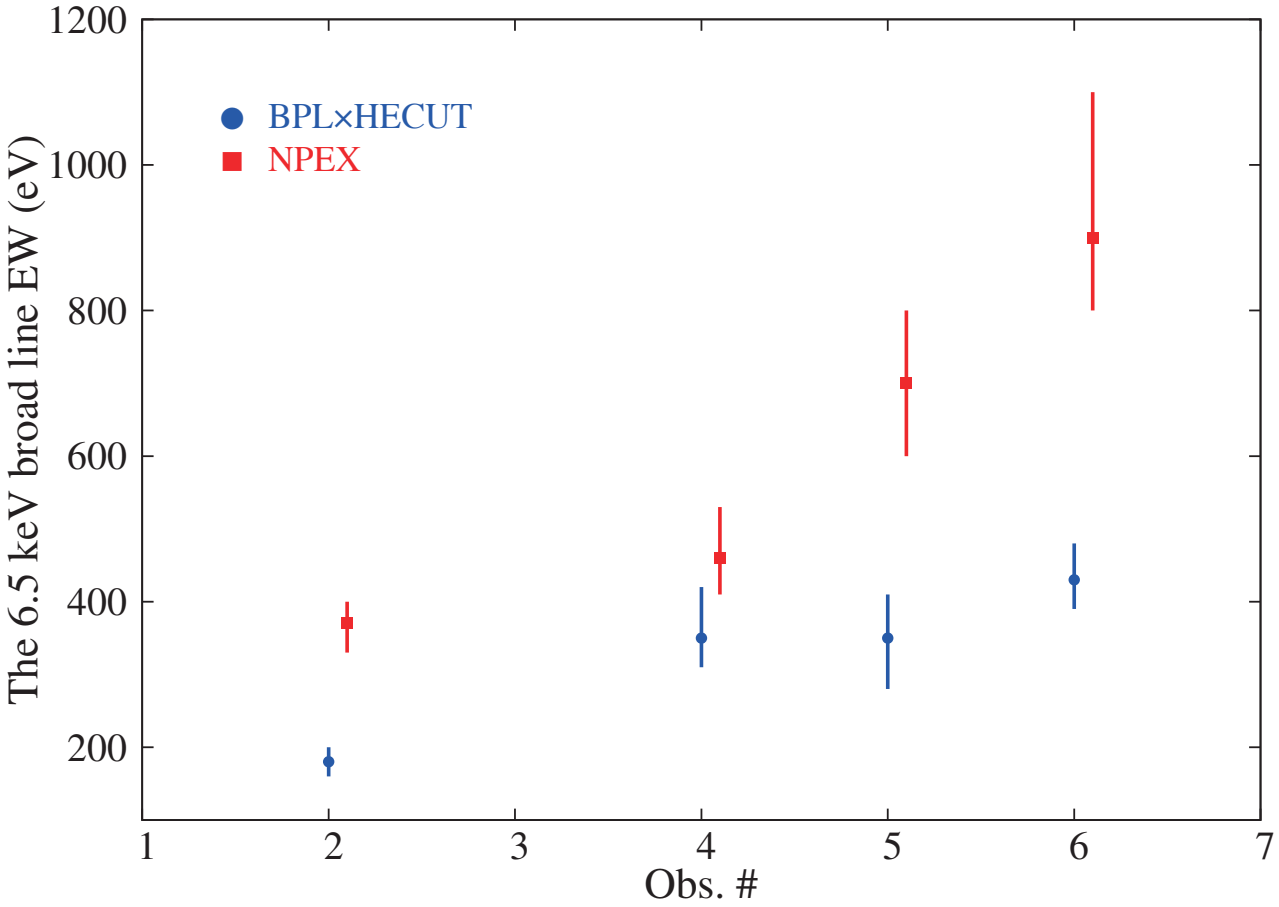

Figure 6.9: The same as Figure 6.8, but for the 6.5 keV broad line EW.

Chapter 7

Discussion

We have revisited the 0.4–100 keV broad-band spectroscopy of Her X-1 with Suzaku, following the 1998 broad-band study with BeppoSAX (dal Fiume et al., 1998). Energy coverage spanning three orders of magnitude includes different components from the soft excess in 0.4–1.8 keV, a continuum from the accretion column, and Fe lines to the CRSF at ∼35 keV. Four Suzaku observations were performed during the main-on phase in 2006 and 2010. The X-ray intensity was 20–90 mCrab and the analyzed exposure was ∼78 ks. The observed flux in the 0.4–100 keV energy band was 3.5–8.8×10^{-9} erg cm^{-2} s^{-1}, a typical value in the main-on state. Assuming a source distance of 6.6 kpc (Reynolds et al., 1997), the observed luminosity was 1.8–4.6×10^{37} erg s^{-1}.

As described in section 6.2, we demonstrated that the 4-9 keV hump feature exists besides the 6.4 and 6.7 keV Fe lines independently of selecting the continuum models. In the main-on phase, only ASCA (Endo et al., 2000) and our study resolved the Fe K line into two narrow lines at 6.4 and 6.7 keV. This excellent energy resolution around 6 keV and the broad band spectroscopic ability of Suzaku help us to confirm the underlying 4-9 keV broad hump. Our data analysis in section 6.3.1 and 6.3.2 revealed that the hump did not originate from the absorption by and the reflection on the cold matter because the no sharp Fe K-edge at 7.1 keV was seen. (In the dim phase of 35 day period, the sharp edge was clearly seen as shown in Figure 7.1.) We discuss the origin of this hump in the following section.

Our data analysis also confirmed that the intense ∼0.1 keV black body and the broad emission feature at ∼1 keV as pointed out in previous observations (Oosterbroek et al., 1997; dal Fiume et al., 1998; Endo et al., 2000; Fürst et al., 2013).

7.1 Partial covering vs. 6.5 keV broad Fe line

In section 6.3, to model the 4–9 keV hump we tried two different spectral models: BPL×HECUT with an ionized partial covering, and the BPL×HECUT or NPEX with a 6.5 keV broad line. These models give reasonable chi-square values, χ^2_ν/dof = 1.35/458, 1.28/458, and 1.36/460, to

the 0.4–100 keV spectra of Obs. 2, respectively (Tables 6.1 and 6.4).

The ionized partial covering model requires that the absorber persistently exist between the observer and the emission region. In previous studies of broad-band spectra including above 10 keV with Ginga (Mihara et al., 1991), RXTE (Coburn et al., 2002), INTEGRAL (Klochkov et al., 2008), and NuSTAR (Fürst et al., 2013) during the main-on, there was no evidence for absorption except a contribution from the galactic interstellar medium. On the other hand, ASCA (Endo et al., 2000) and Chandra (Ji et al., 2009) observations require the partial covering by the cold matter to explain their spectra, though the model was excluded by our study. The ionized partial covering model, however, cannot be excluded because the model has huge uncertainty in abundance or ionizing radiation. A possible origin of such absorber is blob-like one surrounding Her X-1. Nagase et al. (1986) considered such absorber model in Vela X-1 with Ginga. However, the existence and configuration of the ionized absorber is actually unknown.

The 6.5 keV broad-line shape was represented by the Gaussian with a center energy at 6.1–6.5 keV, width of 1.1–1.5 keV, and EW of 400–900 eV with the choice of NPEX continuum (section 6.3.3). The EW is one order of magnitude larger than the 6.4 and 6.7 keV narrow Fe lines. The line width is broader by a factor of $\sim$5 than the similar broad lines seen in other X-ray binaries (Hung et al., 2010; Asai et al., 2000). If the 4–9 keV hump is a broadened Fe line, then this broad-line feature should be attributed to one of the following three interpretations: (1) superposition and blending of lines from Fe ions in various ionization states, (2) Comptonization from an accretion disk corona (ADC), or (3) Doppler broadening in a radiation region, such as the inner edge of an accretion disk or flow. Some of these have been suggested for the line broadening in some X-ray binaries (Asai et al., 2000; Ramsay et al., 2002; Hung et al., 2010). In following subsections, we discuss the details of these possibilities.

7.2 The possible origins of the 6.5 keV broad line

7.2.1 Line blending

If there is a variety of Fe ionization states in the accretion flow, inner edge, or disc corona of Her X-1, then the center energies of fluorescent Fe K-lines will range from 6.40 keV (Fe_{I}) to 6.93 keV (Fe_{XXVI}) as shown in Figure 7.2, and those different states will make the blended line broader. To explore this possibility, we briefly considered a model spectrum consisting of a double Gaussian at 6.4 and 6.93 keV. The model spectrum was used to create a simulated spectrum with the `XSPEC fakeit` command. We fitted the emission lines from Fe_{I} and Fe_{XXVI} by a single Gaussian, but the line width was about $\sigma = 200$ eV. Asai et al. (2000) simulated spectra from a plasma composed of a range of ionization parameters ξ, ($\log \xi = 2 - 3.5$ which represent the ionization state as shown in Figure 7.3), for the ASCA SIS, and reported that superposition of plasma with different ξ might form an emission line with width less than

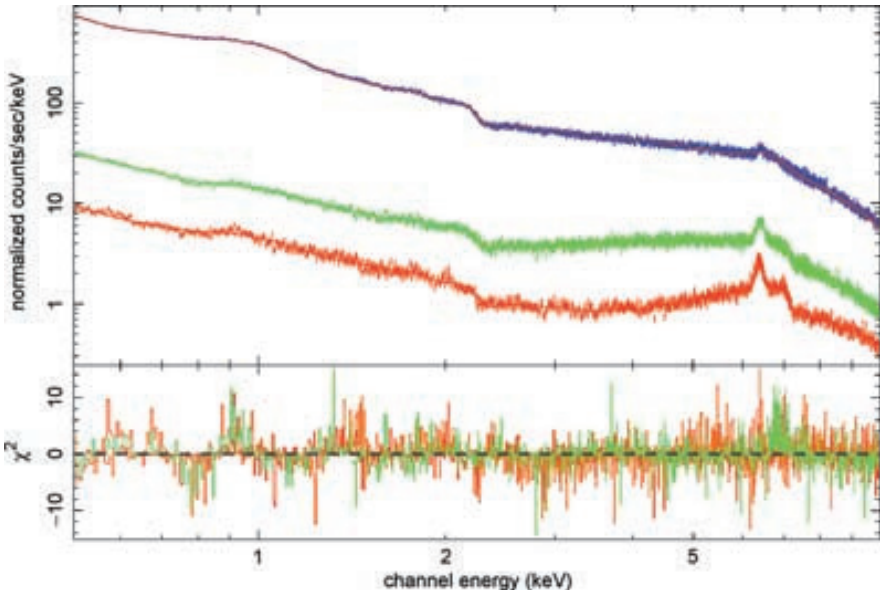

Figure 7.1: Her X-1 spectra in three different 35-d phases, main-on (blue), short-on (green), and low-state (red), obtained with XMM-Newton (Ramsay et al., 2002).

0.1 keV (FWHM), but could not make a single broad line. Therefore, line blending cannot explain the observed broad-line width of Her X-1, and another mechanism should be included.

7.2.2 Comptonization from ADC

Comptonization is another mechanism behind line broadening. We consider that the seed Fe line is Comptonized in ADC as shown in Figure fg:comptonization in ADC. The line width of a Comptonized line profile is expressed, as given in Kallman and White (1989); Brandt and Matt (1994), by

$$\sigma = 0.019\epsilon_0\tau_{\rm Th}(1 + 0.78kT_{\rm e}), \tag{7.1}$$

where ϵ_0 is the initial energy of the incident photon, $\tau_{\rm Th}$ is the Thomson optical depth, and $kT_{\rm e}$ is the electron temperature in kilo electron volts. We consider that seed photons (Fe line emission) is Comptonized in ADC. Ji et al. (2009) estimated the properties of ADC of Her X-1 and found a density $n \sim 10^{12-13}$ cm^{-3}, electron temperature $kT_{\rm e} \sim 170$–430 eV, and size 2×10^{10} cm$\leq r_{\rm ADC} \leq 3 \times 10^{11}$ cm. Using the values of n and $r_{\rm ADC}$, $\tau_{\rm Th}$ is $0.01 \leq \tau_{\rm Th} \leq 2$. Thus, the line width is $\sigma \leq 320$ eV for Fe K$_\alpha$. We therefore conclude that Comptonization in ADC is unlikely to cause the 6.5 keV broad line.

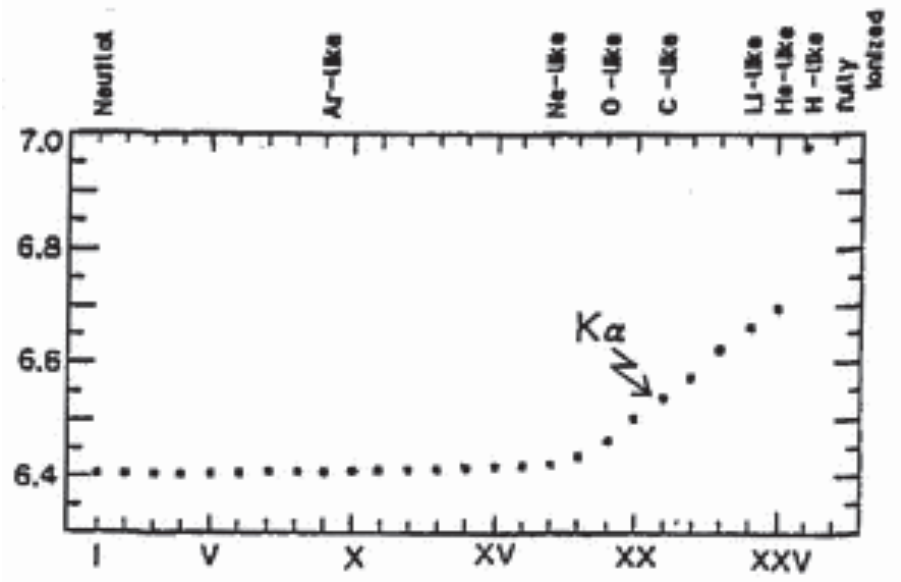

Figure 7.2: Fe K_α line energy as a function of the ionization degree (Makishima, 1986).

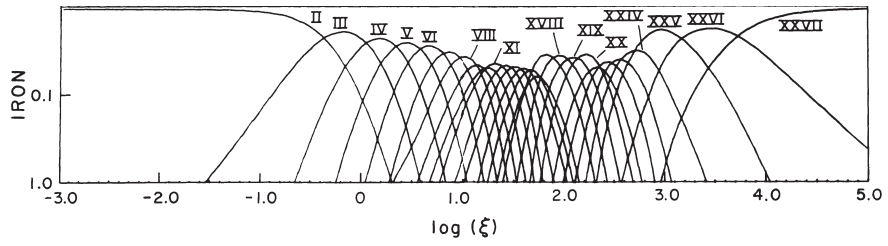

Figure 7.3: Relative ionization population of Fe. (Kallman and McCray, 1982).

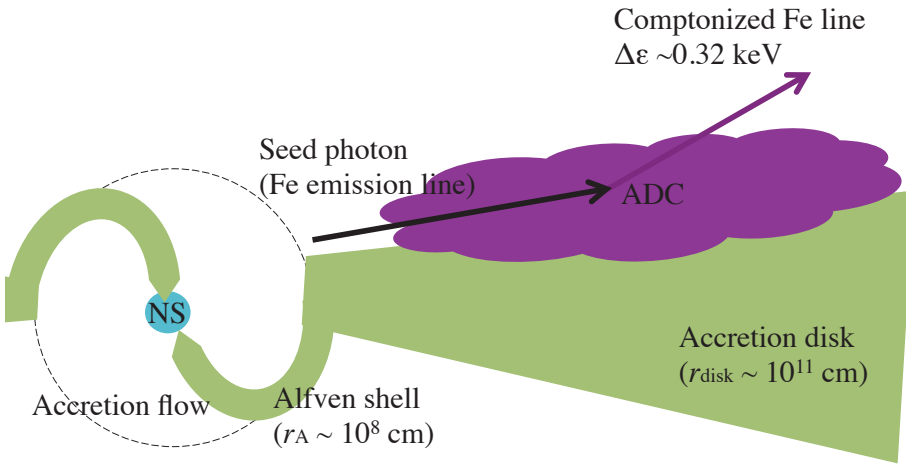

Figure 7.4: A description of the Comptonizaion in ADC.

7.2.3 Doppler broadening at the inner disk

We next consider another possible cause of the line broadening, Doppler line broadening in the inner disk. Figure 7.5 shows its description. The Alfven radius $r_{\rm A}$ of the averaged Suzaku observations ($L_{\rm X} = 3.4 \times 10^{37}$ erg s^{-1}) is calculated to be 2.5 $\times 10^8$ cm. Assuming a neutron star mass of $M_{\rm NS} = 1.4 M_{\odot}$, a radius of $R_{\rm NS} = 10^6$ cm, and a conversion efficiency of mass-accretion to X-ray luminosity of η =0.1, the mass-accretion rate is $\dot{M}$ = 1.8$\times 10^{18}$ g s^{-1}. This value and the formula of $r_{\rm A} = (\mu^4/2G\dot{M}^2 M_{\rm NS})^{1/7}$, where G is the gravitation constant and μ is the magnetic dipole moment, for which we use the value 3×10^{30} G cm^3, give the value of $r_{\rm A}$. We find the Keplerian velocity ($v_{\rm Kepler}$) at the Alfven shell to be $\sim$0.03 of the light velocity c, with $v_{\rm Kepler}/c (= \beta_{\rm Kepler}) = \sqrt{r_{\rm g}/2r}$, where $r_{\rm g}$ is the Schwarzschild radius of the neutron star, i.e., $r_{\rm g} = \sqrt{GM_{\rm NS}/c^2}$, and r is the distance from the neutron star. The Doppler shift is expressed as $\Delta\epsilon = \epsilon_0 \beta_{\rm Kepler}/(1-\beta_{\rm Kepler})$, so that $\beta_{\rm Kepler}$ of 0.03 corresponds to the Doppler shift of 200 eV at the 6.4 keV Fe K_α line. Thus, Doppler broadening at the Alfven shell is not a plausible explanation for the origin of the 6.5 keV broad line.

7.2.4 Doppler broadening at an accretion flow

The free fall velocity of matter in the accretion flow can reach several 10% of c, which corresponds to the Doppler shift of several hundred eV to a few keV at the 6.4 keV. Since the actual value of the Doppler shift depends on the line-of-sight velocity and the geometrical configuration of the accretion flow is not revealed, we only note that the Doppler effect in the accretion flow might be a possible origin of the line broadening.

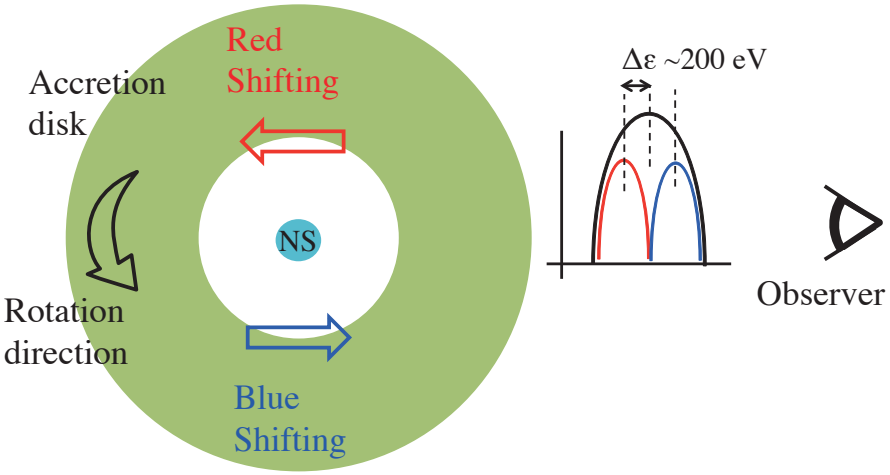

Figure 7.5: A schematic view of the Doppler broadening at inner edge of the accretion disk.

The ionization state of the plasma is primarily determined by the ionization parameter ξ ($\equiv L_{\rm X}/nr^2$) which increased in proportion to an X-ray flux and decreases in inverse proportion to the number density of the plasma n. Because the X-ray flux illuminating the accretion flow is high, the Fe ions in the accretion flow might be fully photo-ionized and cannot generate the line emission. To take account of a possibility of line emission from the accretion flow, we estimate ξ within $r_{\rm A}$. Since the mass-accretion rate $\dot{M} = n(r)v(r)S(r)$ is constant, where $v(r)$ is a velocity of the accreting matter and $S(r)$ is a cross-section of the accretion flow at r, we obtain the relation of $n(r)v(r)S(r) = n(r_{\rm A})v(r_{\rm A})S(r_{\rm A})$. Assuming that the neutron star has a dipole magnetic field $B \propto r^{-3}$, the cross-section of the accretion flow is $S \propto r^3$ because of the relation of $BS =$ constant. We assume that the velocity of the accreting matter is the free fall velocity $v_{\rm ff} = \sqrt{r_{\rm g}/r}$, and obtain

$$n(r) = n_{\rm A}\left(\frac{r}{r_{\rm A}}\right)^{-5/2}, \tag{7.2}$$

where $n_{\rm A}$ is the density at $r_{\rm A}$. Thus, the ionization parameter in the accretion flow is given as

$$\xi(r) = \xi_{\rm A}\left(\frac{r}{r_{\rm A}}\right)^{1/2}, \tag{7.3}$$

where $\xi_{\rm A}$ is the ionization parameter at $r = r_{\rm A}$. Because the 6.4 keV Fe line whose emission site is the inner edge of the accretion disk is seen, the $\xi_{\rm A}$ is low and allow the line emission. According to Equation 7.3, It is possible to produce the line emission from the Fe ions in the

accretion flow. Endo et al. (2002) also showed that in the X-ray pulsar GX301-2, which has an X-ray luminosity similar to that of Her X-1, the nearly neutral ionization state of Fe is realized in the accretion flow even around $r \sim 10^7$ cm.

The 6.5 keV broad line has a symmetric structure, implying that the red-shifted and the blue-shifted photons are required. In Her X-1, only one side of the magnetic pole is thought to be seen because of the single-peak pulse profile. From this reason, only the red-shifted accretion flow can be seen at the region very close ($\sim 10^6$ cm) to the neutron star surface. It is, however, possible to observe the blue-shifted (opposite side) accretion flow, since the iron line is assumed to emit from a wider region (10^6–10^7 cm) of the flow which is not covered by the neutron star.

Since the 6.5 keV broad line has a large EW, we estimate whether the Doppler broadening in the accretion flow can explain the observed one. As shown in Figure 7.7, if the X-ray illuminated matter is outside the line of sight from the X-ray emitter to us and the incident spectrum can be directly observed, the EW could be expected by the equation (Makishima, 1986):

$$\mathrm{EW} \sim \frac{\Omega}{4\pi} \times nl \times \alpha\omega\sigma_{\mathrm{Fe}}(E) \exp(-n\sigma_{\mathrm{P.E.}}(E)l_1 - n\sigma_{\mathrm{P.E.}}(6.4\ \mathrm{keV})l_2) \times \Delta E. \tag{7.4}$$

Here Ω is a solid angle of the absorber to the light source, l is the absorber size, $\alpha = 5 \times 10^{-5}$ is the cosmic Fe abundance, $\omega = 0.34$ is the fluorescence yield of Fe, σ_{Fe} is the Fe cross-section of photo-electric (P.E.) absorption, $\sigma_{\mathrm{P.E.}}$ is the total cross-section of the P.E. absorption. For the incident photon energy of 7.1 keV which is the K-shell binding energy of Fe, $\sigma_{\mathrm{Fe}} = 4 \times 10^{-5}$ cm^2. We assume the absorber with highest-emissivity where the incident photons enter the absorber and is immediately absorbed by the Fe ion, i.e. $l_1 \ll l_2 \sim l$ and use $\sigma_{\mathrm{P.E.}}(6.4\ \mathrm{keV}) = 6.55 \times 10^{-25}$ cm. Figure 7.8 shows the expected line EW as a function of the matter thickness, $nl = N_{\mathrm{H}}$. The absorber, i.e. the accretion flow, requires a large ($\geq 2\pi$) solid angle to the light source (accretion column). According to Endo et al. (2000), the solid angle of the accretion flow is $\Omega(r) = 2\pi[1 - \sqrt{1 - (r/r_{\mathrm{A}})}]$, which give $\Omega(10^7\ \mathrm{cm}) = 0.01$. A difficulty in this accretion flow model is that the large EW of the broad line cannot be explained with a simple geometry. In reality, the EW depends on the geometry of the matter, isotropy of the radiation, Fe abundance, and so on. In spite of these uncertainties, we consider that the large EW is a challenge to the 6.5 keV broad line model. However, the isotropic accretion-column emission may be able to explained the large EW because we overestimate the EW if the the directly accretion-column emission is lower than that illuminating the surrounding absorber (i.e, the accretion flow). Thus, the Doppler broadening at the accretion flow cannot be rejected completely.

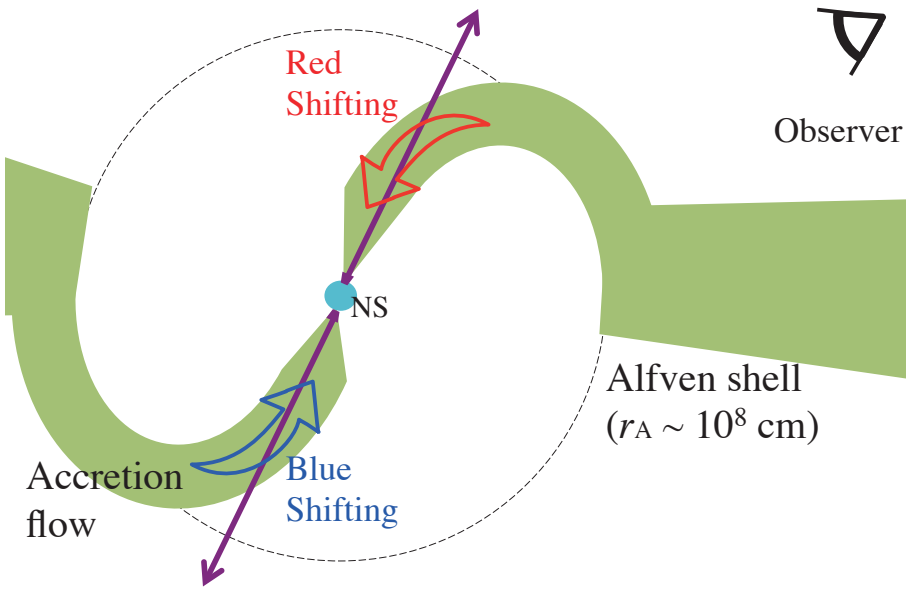

Figure 7.6: A schematic view of the Doppler broadening in the accretion disk. The accretion column and accretion-column emission are indicated by purple.

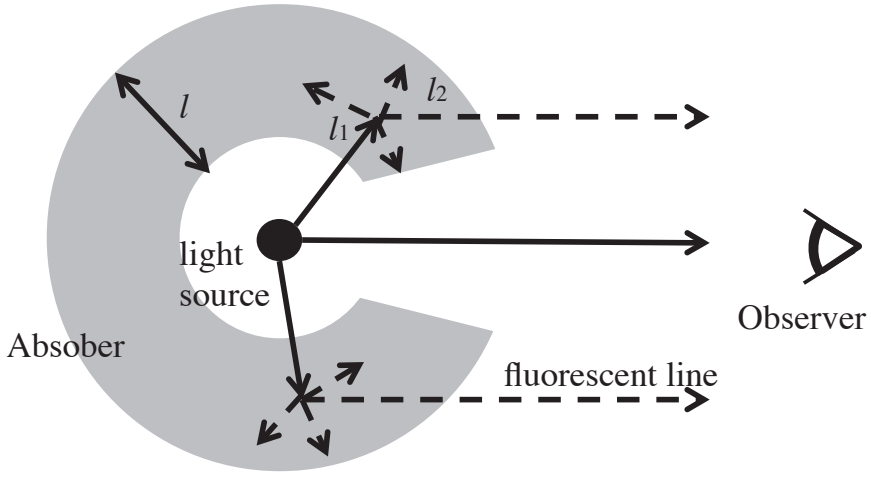

Figure 7.7: A schematic view of the radiation transfer around a compact X-ray source.

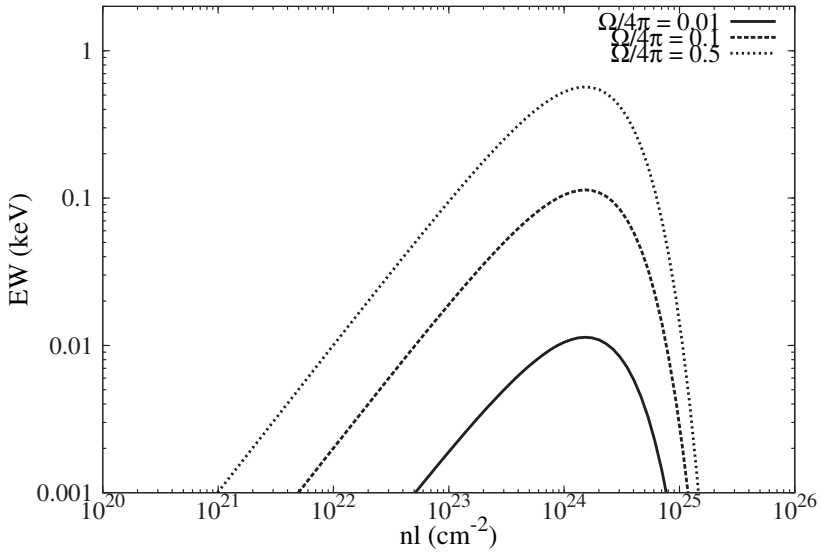

Figure 7.8: A schematic view of the radiation transfer around a compact X-ray source.

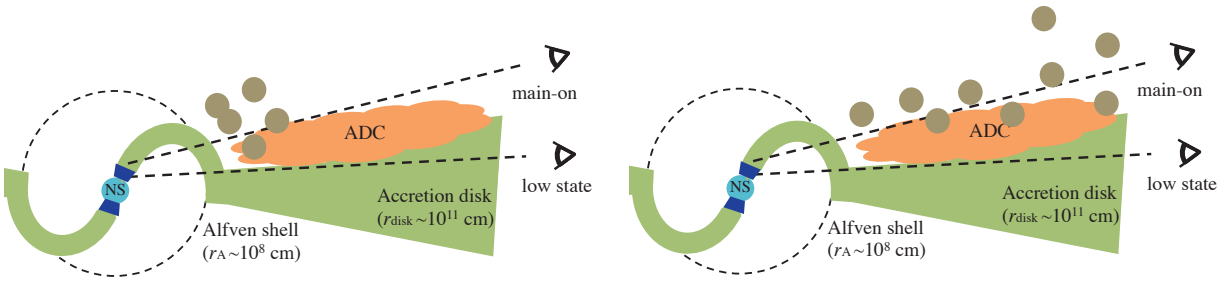

Figure 7.9: The schematic view of the locally (left) and widely (right) distributions of the blob-like absorbers along the radial direction.

7.3 Future works

We revealed the existence of the 4–9 keV hump in Her X-1 spectrum. The origin should be verified by future observations in dim phases of the 35-d cycle. We consider the case of the ionized partial covering. Assuming that the blob-like absorbers locally distribute inner region of the accretion disk as shown in Figure 7.9, the 4–9 keV hump should not appear in the dim phase due to occultation by the disk. In last November to confirm this scenario, we proposed an observation of Her X-1 in the low state.

In the future, we can observe Her X-1 with further higher energy and time resolution using the ASTRO-H satellite which is a Japanese sixth X-ray mission. One of the instrument on board ASTRO-H is a micro-calorimeter spectrometer array (soft X-ray spectrometer: SXS), which has energy resolution of 7 eV (FWHM) at 6 keV and time resolution of a few ten μs. Therefore it is possible to explore the temporal variations of the 4–9 keV hump parameters with the pulse phase independent with the narrow Fe lines. In the case of the ionized partial covering the model parameters would have little temporal variation because it is unlikely that the absorbers anisotropically distribute along azimuthal angle on the accretion disk. On the other hand, in the case of the 6.5 keV broad line from the accretion flow the model parameters would vary with the pulse phase since the accretion-flow motion in the line of sight should change.

Chapter 8

Summary

We performed the X-ray study of the accretion-powered pulsar Her X-1 with Suzaku. We summarize the results of our broad-band spectral analysis.

- We demonstrated that the 4–9 keV hump feature exists besides the 6.4 and 6.7 keV Fe lines independently of selecting the continuum models. The excellent energy resolution around 6 keV and the broad-band spectroscopic ability of Suzaku help us to confirm the underlying 4–9 keV broad hump. The hump was seen in all the four observations regardless of the selection of the continuum models. Thus the 4–9 keV hump is considered to be normally present and intrinsic spectral feature in Her X-1.

- The 4–9 keV hump was represented by two different spectral models: the ionized partial covering or the additional broad line at 6.5 keV. The former required a persistently existing of blob-like ionized absorber. The distribution of such an absorber and its supplier was not clear. In the latter case, the Gaussian fitting of the $\sim$6.5 keV line needs a large width of σ = 1.0–1.5 keV and a large equivalent width of 400–900 eV. If the broad line originates from iron fluorescence of accreting matter, its large width may be explained by the Doppler broadening in the accretion flow where the accreting matter has high velocity of a few 10% of the light velocity. However, the large equivalent width may be inconsistent with a simple accretion geometry, the solid angle of the accretion flow to the accretion column, and assuming the dipole magnetic field. Anisotropic radiation from the accretion column might be able to explain the inconsistent because we overestimated the equivalent width if the accretion-column emission in the line of sight is lower than that illuminating the accretion flow.

Bibliography

K. Asai, T. Dotani, et al. (2000). Iron K Emission Lines in the Energy Spectra of Low-Mass X-Ray Binaries Observed with ASCA. *ApJS*, 131:571–591.

F. Asami, T. Enoto, et al. (2014). Broad-band spectroscopy of hercules x-1 with suzaku. *pasj*, in press.

F. Asami, T. Tamagawa, et al. (2009). Mapping study of gain and hole diameter of japanese gems. In *Nuclear Science Symposium Conference Record (NSS/MIC), IEEE*, pages 734 – 737.

W. Baade and F. Zwicky (1934). On Super-novae. *Proceedings of the National Academy of Science*, 20:254–259.

M. M. Basko (1980). Iron line emission from the Alfven shell in X-ray binaries. *A&A*, 87:330–338.

P. A. Becker and M. T. Wolff (2007). Thermal and Bulk Comptonization in Accretion-powered X-Ray Pulsars. *ApJ*, 654:435–457.

J. M. Blondin, T. R. Kallman, et al. (1990). Hydrodynamic simulations of stellar wind disruption by a compact X-ray source. *ApJ*, 356:591–608.

H. Bondi and F. Hoyle (1944). On the mechanism of accretion by stars. *MNRAS*, 104:273.

W. M. Brandt and G. Matt (1994). Iron K-Alpha Lines from Ionized Discs in Z-Type X-Ray. *MNRAS*, 268:1051.

E. M. Cackett, J. M. Miller, et al. (2010). Relativistic Lines and Reflection from the Inner Accretion Disks Around Neutron Stars. *ApJ*, 720:205–225.

C. S. Choi, F. Nagase, et al. (1994). Iron line intensity variations of Hercules X-1 over the pulse phase and the 35 day cycle. *ApJ*, 437:449–457.

W. Coburn, W. A. Heindl, et al. (2002). Magnetic Fields of Accreting X-Ray Pulsars with the Rossi X-Ray Timing Explorer. *ApJ*, 580:394–412.

D. dal Fiume, M. Orlandini, et al. (1998). The broad-band (0.1-200 keV) spectrum of HER X-1 observed with BeppoSAX. *A&A*, 329:L41–L44.

J. K. Daugherty and A. K. Harding (1986). Compton scattering in strong magnetic fields. *ApJ*, 309:362–371.

P. B. Demorest, T. Pennucci, et al. (2010). A two-solar-mass neutron star measured using Shapiro delay. *Nature*, 467:1081–1083.

T. Endo, M. Ishida, et al. (2002). Broadening of Nearly Neutral Iron Emission Line of GX 301-2 Observed with ASCA. *ApJ*, 574:879–898.

T. Endo, F. Nagase, and T. Mihara (2000). Pulse-Phase Resolved Spectroscopy of Hercules X-1 with ASCA. *PASJ*, 52:223.

T. Enoto, K. Makishima, et al. (2008). Suzaku Observations of Hercules X-1: Measurements of the Two Cyclotron Harmonics. *PASJ*, 60:57.

Y. Fukazawa, T. Mizuno, et al. (2009). Modeling and Reproducibility of Suzaku HXD PIN/GSO Background. *PASJ*, 61:17.

F. Fürst, B. W. Grefenstette, et al. (2013). The Smooth Cyclotron Line in Her X-1 as Seen with Nuclear Spectroscopic Telescope Array. *ApJ*, 779:69.

D. Gerend and P. E. Boynton (1976). Optical clues to the nature of Hercules X-1/HZ Herculis. *ApJ*, 209:562–573.

R. Giacconi, H. Gursky, et al. (1973). Further X-ray observations of Hercules X-1 from Uhuru. *ApJ*, 184:227–236.

R. Giacconi, H. Gursky, et al. (1971). Discovery of Periodic X-Ray Pulsations in Centaurus X-3 from UHURU. *ApJ*, 167:L67.

R. Giacconi, H. Gursky, et al. (1962). Evidence for x Rays From Sources Outside the Solar System. *Physical Review Letters*, 9:439–443.

W. A. Heindl, R. E. Rothschild, et al. (2004). Timing and Spectroscopy of Accreting X-ray Pulsars: the State of Cyclotron Line Studies. In P. Kaaret, F. K. Lamb, and J. H. Swank, editors, *X-ray Timing 2003: Rossi and Beyond*, volume 714 of *American Institute of Physics Conference Series*, pages 323–330.

H. Heiselberg (2002). Neutron Star Masses, Radii and Equation of State. *ArXiv Astrophysics e-prints*.

R. C. Hickox, R. Narayan, and T. R. Kallman (2004). Origin of the Soft Excess in X-Ray Pulsars. *ApJ*, 614:881–896.

L.-W. Hung, R. C. Hickox, et al. (2010). Suzaku X-ray Spectra and Pulse Profile Variations During the Superorbital Cycle of LMC X-4. *ApJ*, 720:1202–1214.

K. Jahoda, C. B. Markwardt, et al. (2006). Calibration of the Rossi X-Ray Timing Explorer Proportional Counter Array. *ApJS*, 163:401–423.

L. Ji, N. Schulz, et al. (2009). The Photoionized Accretion Disk in Her X-1. *ApJ*, 700:977–988.

T. Kallman and N. E. White (1989). Iron K lines from low-mass X-ray binaries. *ApJ*, 341:955–960.

T. R. Kallman and R. McCray (1982). X-ray nebular models. *ApJS*, 50:263–317.

R. L. Kelley, K. Mitsuda, et al. (2007). The Suzaku High Resolution X-Ray Spectrometer. *PASJ*, 59:77–112.

D. Klochkov (2007). *X-ray observations of the accreting pulsars Her X-1 and EXO 2030+375*. PhD thesis, Eberhard-Karls-Universitat zu Tubingen.

D. Klochkov, R. Staubert, et al. (2008). INTEGRAL observations of Hercules X-1. *A&A*, 482:907–915.

M. Kokubun, K. Makishima, et al. (2007). In-Orbit Performance of the Hard X-Ray Detector on Board Suzaku. *PASJ*, 59:53–76.

K. Koyama, H. Tsunemi, et al. (2007). X-Ray Imaging Spectrometer (XIS) on Board Suzaku. *PASJ*, 59:23–33.

M. Kuster, J. Wilms, et al. (2005). Probing the outer edge of an accretion disk: a Her X-1 turn-on observed with RXTE. *A&A*, 443:753–767.

D. Lai and W. C. Ho (2003). Polarized X-Ray Emission from Magnetized Neutron Stars: Signature of Strong-Field Vacuum Polarization. *Physical Review Letters*, 91(7):071101.

F. K. Lamb, C. J. Pethick, and D. Pines (1973). A Model for Compact X-Ray Sources: Accretion by Rotating Magnetic Stars. *ApJ*, 184:271–290.

J. M. Lattimer and M. Prakash (2001). Neutron Star Structure and the Equation of State. *ApJ*, 550:426–442.

A. M. Levine, H. Bradt, et al. (1996). First Results from the All-Sky Monitor on the Rossi X-Ray Timing Explorer. *ApJ*, 469:L33.

P. Magdziarz and A. A. Zdziarski (1995). Angle-dependent Compton reflection of X-rays and gamma-rays. *MNRAS*, 273:837–848.

K. Makishima (1986). Iron Lines from Galactic and Extragalactic X-ray Sources. In K. O. Mason, M. G. Watson, and N. E. White, editors, *The Physics of Accretion onto Compact Objects*, volume 266 of *Lecture Notes in Physics, Berlin Springer Verlag*, page 249.

K. Makishima, T. Mihara, et al. (1999). Cyclotron Resonance Effects in Two Binary X-Ray Pulsars and the Evolution of Neutron Star Magnetic Fields. *ApJ*, 525:978–994.

R. A. McCray, J. M. Shull, et al. (1982). Einstein Observatory pulse-phase spectroscopy of Hercules X-1. *ApJ*, 262:301–307.

P. Meszaros (1992). *High-energy radiation from magnetized neutron stars*.

P. Meszaros and W. Nagel (1985). X-ray pulsar models. II - Comptonized spectra and pulse shapes. *ApJ*, 299:138–153.

P. Meszaros, R. Novick, et al. (1988). Astrophysical implications and observational prospects of X-ray polarimetry. *ApJ*, 324:1056–1067.

T. Mihara (1995). *Observational study of X-ray spectra of binary pulsars with Ginga*. PhD thesis, , Dept. of Physics, Univ. of Tokyo (M95), (1995).

T. Mihara, K. Makishima, et al. (1990). New observations of the cyclotron absorption feature in Hercules X-1. *Nature*, 346:250–252.

T. Mihara, T. Ohashi, et al. (1991). X-ray spectrum of Hercules X-1 in the low state of the 35-day cycle. *PASJ*, 43:501–521.

K. Mitsuda, M. Bautz, et al. (2007). The X-Ray Observatory Suzaku. *PASJ*, 59:1–7.

F. Nagase, S. Hayakawa, et al. (1986). Circumstellar matter in the VELA X-1/HD 77581 system. *PASJ*, 38:547–569.

H. Nakajima, H. Yamaguchi, et al. (2008). Performance of the Charge-Injection Capability of Suzaku XIS. *PASJ*, 60:1.

K. Nakazawa, T. Ueda, et al. (2010). Suzaku wide-band observation of anomalous dips in Hercules X-1. In K. Makishima, editor, *The Energetic Cosmos: from Suzaku to ASTRO-H*, pages 264–267.

T. Oosterbroek, A. N. Parmar, et al. (2000). BeppoSAX spectroscopy of the Hercules X-1 short-on state. *A&A*, 353:575–582.

T. Oosterbroek, A. N. Parmar, et al. (1997). The BeppoSAX LECS X-ray spectrum of Hercules X-1. *A&A*, 327:215–218.

J. R. Oppenheimer and G. M. Volkoff (1939). On Massive Neutron Cores. *Physical Review*, 55:374–381.

M. Ozawa, H. Uchiyama, et al. (2009). Energy-Scale Calibration of the Suzaku X-Ray Imaging Spectrometer Using the Checker Flag Charge-Injection Technique in Orbit. *PASJ*, 61:1.

G. Ramsay, S. Zane, et al. (2002). XMM-Newton EPIC observations of Her X-1. *MNRAS*, 337:1185–1192.

N. Rea, L. Stella, et al. (2005). A Compton reflection dominated spectrum in a peculiar accreting neutron star. *MNRAS*, 364:1229–1238.

J. Reeves, C. Done, et al. (2008). On why the iron K-shell absorption in AGN is not a signature of the local warm/hot intergalactic medium. *MNRAS*, 385:L108–L112.

A. P. Reynolds, H. Quaintrell, et al. (1997). A new mass estimate for Hercules X-1. *MNRAS*, 288:43–52.

R. E. Rothschild, P. R. Blanco, et al. (1998). In-Flight Performance of the High-Energy X-Ray Timing Experiment on the Rossi X-Ray Timing Explorer. *ApJ*, 496:538.

D. M. Scott, D. A. Leahy, and R. B. Wilson (2000). The 35 Day Evolution of the Hercules X-1 Pulse Profile: Evidence for a Resolved Inner Disk Occultation of the Neutron Star. *ApJ*, 539:392–412.

P. J. Serlemitsos, Y. Soong, et al. (2007). The X-Ray Telescope onboard Suzaku. *PASJ*, 59:9–21.

Y. Soong, D. E. Gruber, et al. (1990). Temporal behavior of Hercules X-1 - The long-term variability of its pulse profile and the 35 day X-ray intensity modulation. *ApJ*, 348:634–640.

R. Staubert (2013). Hercules X-1: variations of the cyclotron line energy with flux, with phase and with time. *ArXiv e-prints*.

R. Staubert, D. Klochkov, and J. Wilms (2009). Updating the orbital ephemeris of Hercules X-1; rate of decay and eccentricity of the orbit. *A&A*, 500:883–889.

M. Still, K. O'Brien, et al. (2001). RXTE Observations of Hercules X-1 during the 1998 July Short High State. *ApJ*, 553:776–787.

J. Swank, T. Kallman, and K. Jahoda (2008). Gravity and Extreme Magnetism SMEX. In *37th COSPAR Scientific Assembly*, volume 37 of *COSPAR Meeting*, page 3102.

T. Takahashi, K. Abe, et al. (2007). Hard X-Ray Detector (HXD) on Board Suzaku. *PASJ*, 59:35–51.

T. Tamagawa, A. Hayato, et al. (2009). Development of thick-foil and fine-pitch GEMs with a laser etching technique. *Nuclear Instruments and Methods in Physics Research A*, 608:390–396.

T. Tamagawa, N. Tsunoda, et al. (2006). Development of gas electron multiplier foils with a laser etching technique. *Nuclear Instruments and Methods in Physics Research A*, 560:418–424.

H. Tananbaum, H. Gursky, et al. (1972). Discovery of a Periodic Pulsating Binary X-Ray Source in Hercules from UHURU. *ApJ*, 174:L143.

T. M. Tauris and E. P. J. van den Heuvel (2006). *Formation and evolution of compact stellar X-ray sources*, pages 623–665.

J. Truemper, P. Kahabka, et al. (1986). EXOSAT observations of the 35 day cycle of Hercules X-1 Evidence for neutron star precession. *ApJ*, 300:L63–L67.

J. Truemper, W. Pietsch, et al. (1978). Evidence for strong cyclotron line emission in the hard X-ray spectrum of Hercules X-1. *ApJ*, 219:L105–L110.

H. Uchiyama, M. Ozawa, et al. (2009). New CTI Correction Method for Spaced-Row Charge Injection of the Suzaku X-Ray Imaging Spectrometer. *PASJ*, 61:9.

N. E. White, J. H. Swank, and S. S. Holt (1983). Accretion powered X-ray pulsars. *ApJ*, 270:711–734.

S. Yamada, K. Makishima, et al. (2011). Improvements in Calibration of GSO Scintillators in the Suzaku Hard X-Ray Detector. *PASJ*, 63:645.

S. Yamada, H. Uchiyama, et al. (2012). Data-Oriented Diagnostics of Pileup Effects on the Suzaku XIS. *PASJ*, 64:53.

S. Zane, G. Ramsay, et al. (2004). XMM-Newton EPIC and Optical Monitor observations of Her X-1 over the 35-d beat period. *MNRAS*, 350:506–516.

Acknowledgements

A lot of people have contributed to this work. I want to thank them all for their help, advises, and discussions. First of all, I am deeply grateful to my supervisor, Prof. Toru Tamagawa for wise supervision of my research, encouraging and comprehensive discussions. The author especially thank Prof. Kazuo Makishima, who kindly accepted me to spend my early graduate school life as a member of Cosmic Radiation Laboratory in RIKEN.

I especially have a great thanks for Teruaki Enoto, Shin'ya Yamada and Wataru Iwakiri for powerful support and encouragement to my phD study. The author thanks to Prof. Fumiaki Nagase, Tatehiro Mihara for useful advice and discussions. I also thank Takayoshi Khomura for his useful advice and technical support. This thesis would not be possible without their support and discussions with them.

The author thanks all of the GEMS collaborators, for their useful advice to the development of X-ray polarimeter, and for supports to my visit. I am also grateful to Hiroko Tawara, for their technical support and useful advice to the experiments in KEK.

All other members of the Tamagawa laboratory, Naya-san, Kato-san, Goro-san, Katsuda-san, Kitaguchi-san, Hayato-san, Ishikawa-san, Konami-san, Iwahashi-san, Rie-chan, Yoshikawa-kun, Yoko-chan, Kaneko-kun and Megu-chan are appreciated for their help and support in my work. They also made my presentations better. I learned the logical and easily understandable presentation method. I would also thank all members of Makishima laboratory, MAXI team, and Matsushita Laboratory, and Otsu-san, Yoneda-san, Rice Club and Crab Club members. All of them make my school life meaningful and give the excellent environment and friendly atmosphere.

Finally, I wish to thank my family and friends. Without their encouragement and understanding it would have been impossible for me to finish my work.